TIME-RESOLVED SPECTROSCOPIC STUDIES

OF

LASER PRODUCED PLASMAS

by

SYLVIA MUI LENG SIM, B-Sc. (Hons)

Royal Holloway College

University of London

Thesis submitted for the degree of Doctor of Philosophy of the University of London

January 1982

TO MY PARENTS

AND RICHARD

TIME-RESOLVED SPECTROSCOPIC STUDIES OF LASER PRODUCED PLASMAS

by

SYLVIA SIM

ABSTRACT

High speed optical measurements are important for laser fusion studies. At present, streak cameras provide the most versatile direct optical recording techniques with picosecond time resolution, but they possess limited dynamic range. Their poor performance is believed to be partly due to space charge effects at the electron optical cross-over point. This was experimentally investigated in this thesis, but found to be relatively unimportant. Effects inside the photocathode are suggested as an alternative explanation.

The dynamic ranges, sweep speeds and linearity of two commercial streak camera systems were measured using a modelocked dye laser and an etalon. The spatial resolution was measured with a test chart.

These two streak cameras were then used to study the temporal evolution of the backscattered fundamental and harmonic emission spectra from microballoon targets when they were irradiated by a neodymium laser. The spectra at the fundamental frequency displayed the characteristic red shift of Brillouin scattering. The spectral features of the $2\omega_o$ harmonic are explained in terms of ion acoustic turbulence driven by the electron return current. The $3\omega_o/2$ harmonic spectra were observed to consist of two wings, symmetrically shifted to the blue and red, with a separation depending on the electron temperature. Both the $2\omega_o$ and $3\omega_o/2$ harmonic emission were found to consist of picosecond pulsations which are attributed to density perturbations driven by the unstable ablation flow across a steepened density profile.

Finally, proposals are made for the development of diagnostic techniques in laser produced plasmas.

INDEX

CHAPTER 4 THE PERFORMANCE OF THE STREAK CAMERA IN THE PICOSECOND REGION

CHAPTER 5 DIAGNOSTICS FOR HIGH SPEED SPECTROSCOPY

CHAPTER 6 TIME-RESOLVED STUDIES OF BRILLOUIN BACKSCATTER EMISSION FROM LASER IRRADIATED SPHERICAL TARGETS

CHAPTER 1

GENERAL INTRODUCTION

1.1 Introduction

Ultrashort high power laser pulses can be used to irradiate pellets to create isolated high density, high temperature plasmas in which thermonuclear reactions (1.1 - 1.3) may occur. One such reaction is the fusion of deuterium and tritium nuclei to produce helium nuclei (alpha particles), neutrons and energy:

$$D + T \rightarrow \alpha + n + 17.6 \text{ MeV} \qquad I - 1$$

The reaction requires that the initial particles have sufficient energy to overcome the mutual repulsion of the nuclei in a collision. This requires temperatures of the order of 10^8 ^oC (10^4 eV). The reaction rate also increases with particle density. For a given density n_e, appreciable fusion occurs only when the hot gas is contained for a time not less than a critical value τ, first calculated by J.D. Lawson (1.4). The minimum value of the Lawson criterion $n\tau$ for the D-T reaction is 10^{14} $cm^{-3}s$ at a temperature of 25 keV (1.4) and this must be satisfied by any fusion reactor.

In laser driven fusion, the D-T target is compressed and heated by the laser pulse and then left to freely expand. The main compression comes from the rapid ablation of the outer part of the target which drives the core inwards by recoil. A smaller contribution arises from the radiation pressure. A 1 TW beam focussed to 50μm can exert a pressure of 10^7 atm.

Laser radiation incident on the expanding plasma from the irradiated surface encounters a density gradient in the plasma. Where the resonant

frequency ω_p of the plasma electrons in an oscillating electric field is equal to the laser frequency ω_o i.e. $\omega_p = \omega_o$, the dispersion relation for the e.m. wave cannot be satisfied for real k, hence the e.m. wave ceases to propagate and instead , is reflected. This critical density is given by:

$$n_{CR} = 10^{21} \lambda_{\mu m}^{-2} \quad \text{electrons cm}^{-3} \qquad \text{I - 2}$$

where λ is the laser wavelength.

In the case of full ionization of a low Z material where the atomic mass $A \sim 2Z$, the critical density corresponds to a mass density:

$$\rho_{CR} = 3.3 \times 10^{-3} \lambda_{\mu m}^{-2} \quad \text{g cm}^{-3} \qquad \text{I - 3}$$

At the critical density surface, anomalous heating of the plasma can occur due to the process of resonance absorption (1.5). This is the dominant heating mechanism since, as collisional absorption i.e. inverse bremsstrahlung (1.6) is proportional to $T_e^{-3/2}$, it is not expected to play an important role in high temperature plasmas.

The incident light can also act as a pump driving other modes which may be transverse or longitudinal waves. These waves or parametric instabilities will grow provided the driven modes receive more energy than they lose by damping i.e. incident laser energy must exceed a threshold. The existence of some of these instabilities results in light being scattered out of the plasma before it reaches n_{CR} e.g. stimulated Brillouin scattering (1.7) and stimulated Raman scattering (1.7). Others may couple the laser energy to the plasma e.g. the two plasmon decay (1.8) and the parametric decay instabilities (1.9).

The two most powerful lasers at the moment are CO_2 (λ = 10.6 μm) and Nd/glass (λ = 1.06 μm). The latter is used in the experimental studies of laser plasma interaction in this thesis. Present laser

powers of 1 TW have limited optimum target size to less than 100 μm diameter for efficient energy coupling to target implosion. Implosion speeds are typically of the order of 10^7 - 10^8 cm s^{-1} (1.10) so laser pulse lengths are around 100 ps. Hence picosecond time resolution is required for both laser development and target implosion diagnostics.

The development of the streak camera which is capable of time resolution of less than 1 ps (1.11) has greatly facilitated studies in both these fields. However, the low dynamic range possessed by this instrument when used with picosecond resolution, remains a severe limitation. Some of the reasons that might contribute to this performance are investigated in this thesis.

The streak camera can be coupled to the dispersed output of a spectrograph to provide high speed spectroscopy. This technique is used as a diagnostic to study the spectrum of the light backscattered through the main focussing lens. It is intended in this thesis to examine the spectrum for emission at the frequencies ω_o, $2\omega_o$ and $3\omega_o/2$ since they provide evidence for the existence of parametric instabilities. Previous observations (1.12 - 1.14) have identified characteristics of these three spectra:

i) ω_o emission shows a red shift characteristic of Brillouin scattering (1.12)

ii) $2\omega_o$ emission has a spectrum broadened to the red (1.13)

iii) $3\omega_o/2$ emission possesses a double peak spectrum (1.14)

With the advantage of simultaneous high temporal and spectral resolution, it is hoped that the generation mechanisms for these features can be identified more precisely than in the earlier studies. The observation of the backscattered emission can also be useful as a diagnostic for the electron temperature, density gradient scalelengths and bulk motion of the plasma.

This thesis begins with a brief discussion of the processes

involved in laser light absorption and scattering in plasmas. Earlier experimental investigations of the backscattered emission are reviewed. The diagnostics for the high speed spectroscopy experiments are discussed and calibrated in Chapter 5, followed by descriptions and analysis of the experiments in Chapters 6 - 8 on light scattered at the frequencies ω_o, $2\omega_o$ and $3\omega_o/2$ respectively. First, however, we conclude this Chapter with a review of the Nd/glass laser facility where these experiments were performed.

The author has been responsible for the experimental work, data analysis and fitting the results to existing theoretical models in this thesis.

1.2 The Neodymium Glass Laser and Target Area

The main laser pulses for these experiments were provided by the neodymium glass laser at the Science and Engineering Research Council (SERC) Laser Facility, Rutherford Laboratory. Full descriptions of this system can be found in References 1.15 and 1.16. The glass is doped with the triply ionised rare earth neodymium ion Nd^{3+} and the optical transitions involved are within the partially filled 4f shell (e.g. $^4F_{3/2} \rightarrow {}^4I_{11/2}$). This laser produces pulses of up to 100 J with durations of 50 ps to 2 ns and wavelengths near to 1.06 μm. Single or multiple beam operation is possible. A wide range of diagnostics is available both in the laser area and in the vicinity of the interaction chamber.

1.3 Description of the Nd/glass Laser System

The laser system consists of a Quantel neodymium YAG (yttrium aluminium garnet) oscillator which is used to drive silicate glass rod and disc amplifier chains as shown in Fig. 1.1. For these experiments, both short (100 ps) and long (1.8 ns) pulses were used, which are generated by different methods.

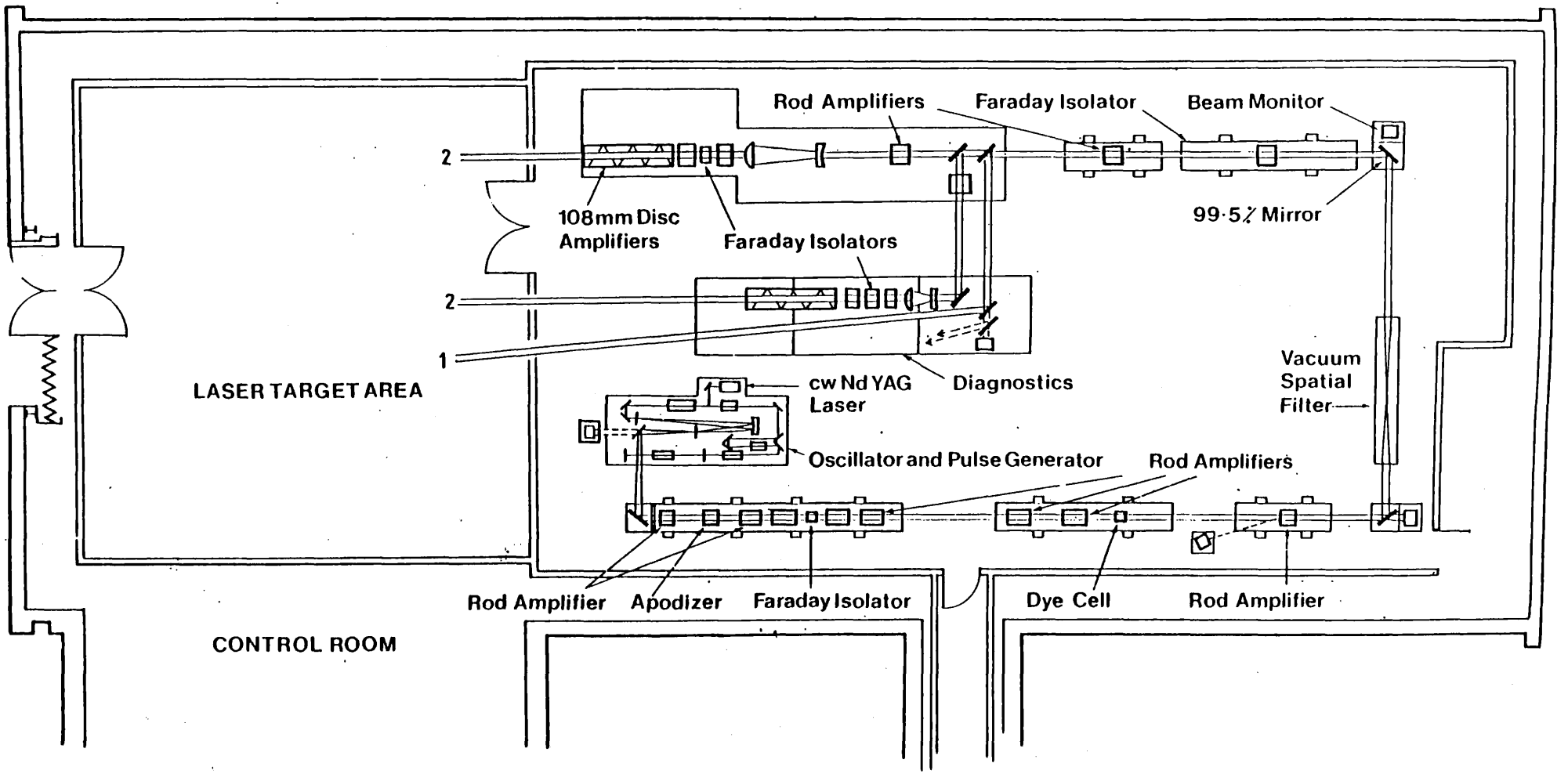

FIG. 1.1 - Schematic layout of the SERC Nd/glass laser, Rutherford Laboratory.

1.3.1. Short Pulse Generation

Fig. 1.1 shows the schematic layout of the laser. The passively mode locked oscillator generates a train of approximately 10 pulses (FWHM = 100 ps) with an interpulse spacing of 7 ns. One of the mode locked pulses, $\sim$ 1 mJ, is switched out by a Pockels cell unit and then passed through a series of rod and disc neodymium doped silicate glass amplifiers. The final beam direction is indicated by '1' for single beam operation and '2' for double beam operation.

Other beam components include the apodizer and vacuum spatial filter to improve the beam quality and reduce the focal spot size. The saturable dye cell after the first Faraday isolator in the chain, reduces prepulses and amplified spontaneous emission. This cell along with the two Faraday rotators (45° rotation) reduces back reflections from the target which otherwise can be amplified and cause damage to the early laser components.

1.3.2. Long Pulse Generation

The long pulses (1.8 ns) are generated by actively "Q" switching the cavity. Fig. 1.2 shows the oscillator bench arrangement. The 20 ns, 6 mJ "Q" switched pulse is first amplified to 50 mJ, then an Electro Optics Development Ltd. (EOD) slicer, consisting of a Pockels cell driven by a laser triggered spark gap, chops out a 1.8 ns spike from the main pulse. After further amplification, the pulse rejoins the common path through the dye cell and double passes the 16 mm glass rod amplifier before continuing down the rest of the single beam amplifier path.

1.4 Laser Area Diagnostics

The main laser area diagnostics are shown in Fig. 1.3. These are provided and operated by the laser facility and full details of their

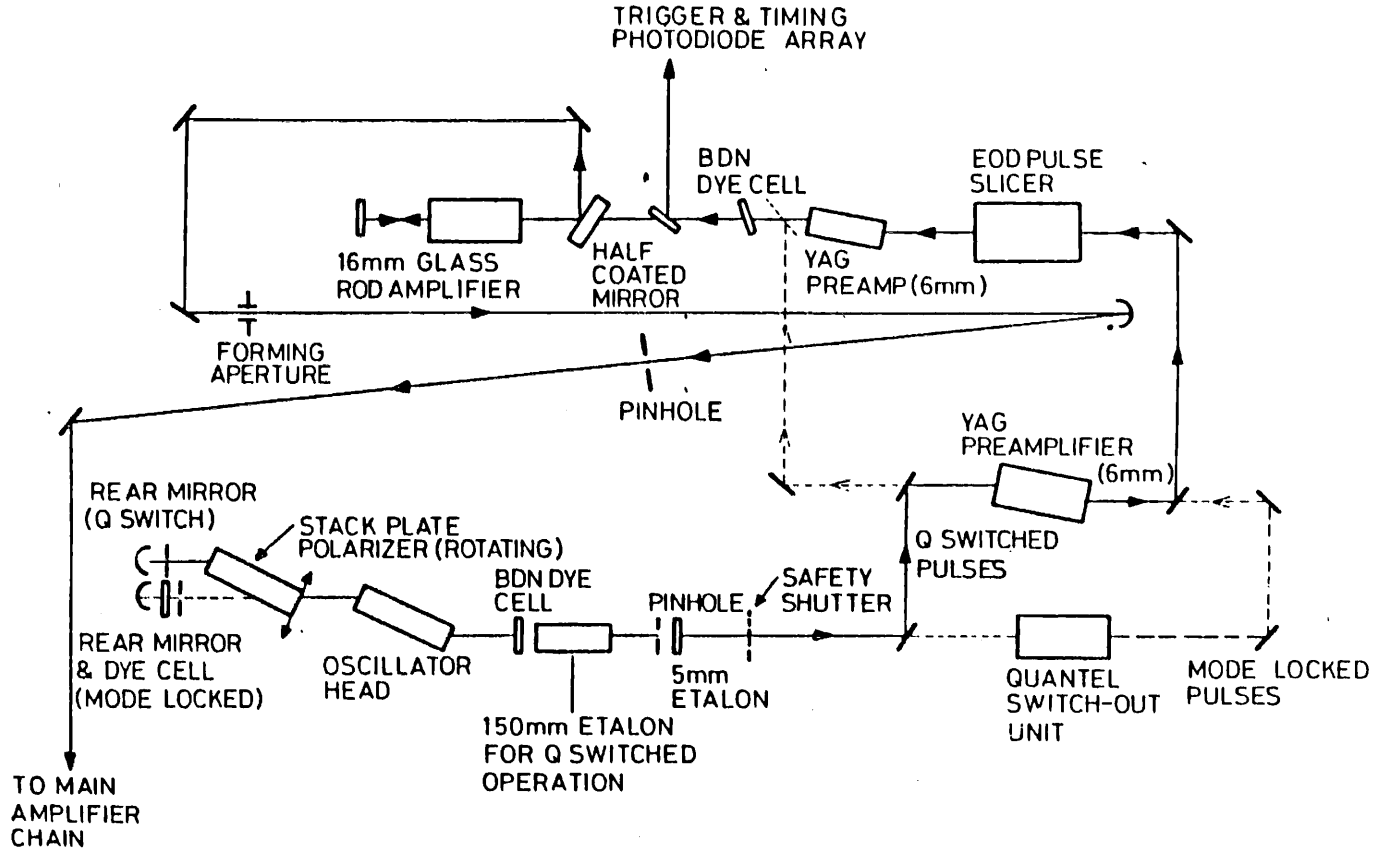

FIG. 1.2 - Oscillator bench arrangement for long pulse generation.

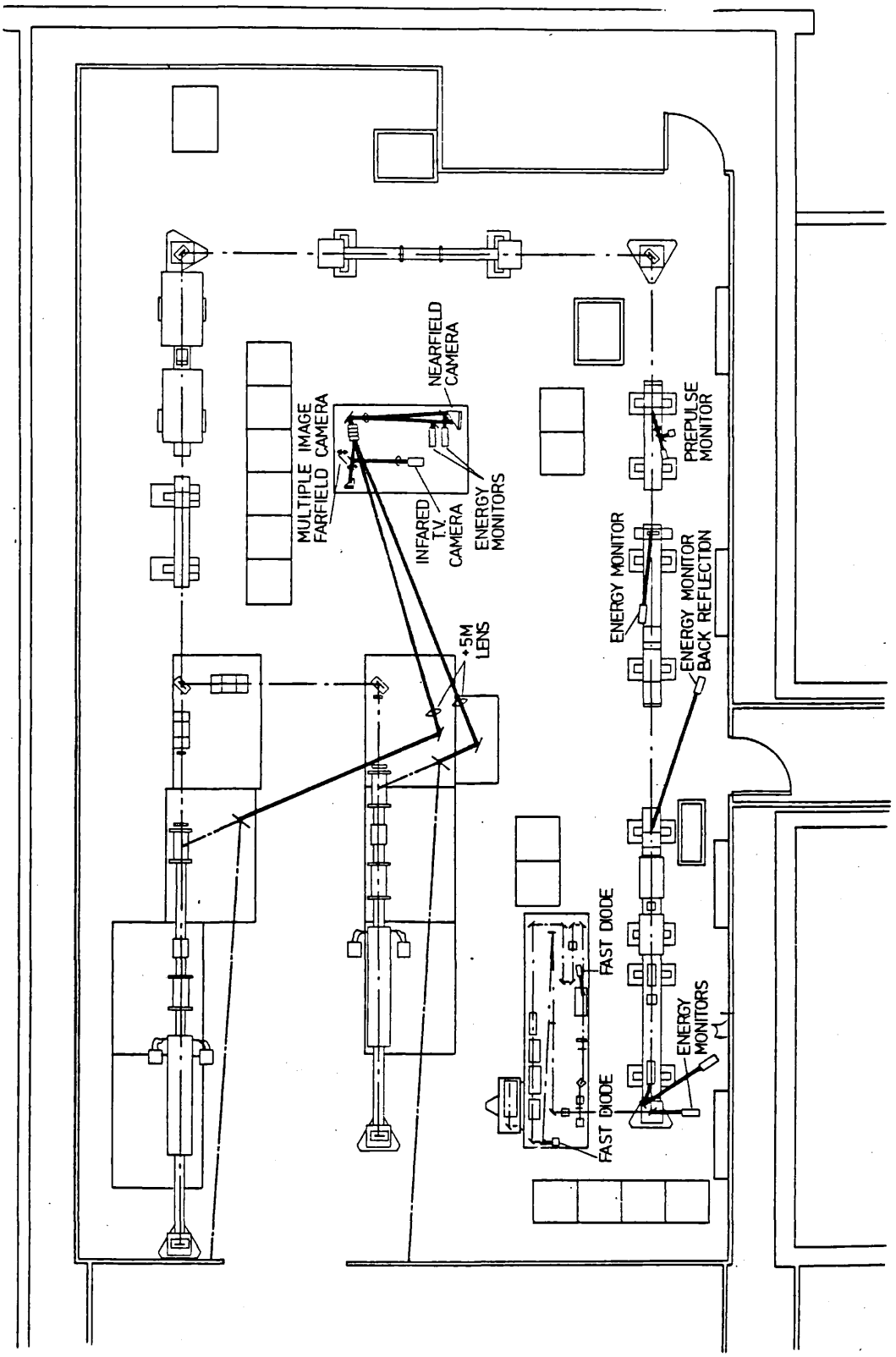

FIG. 1.3 - Laser area diagnostics.

description and operation can be found in References 1.15 and 1.16.

Briefly, the two photodiodes (fast diodes shown on the oscillator bench), monitor the oscillator and pulse selector to ensure only pulses at the peak of a well behaved modelocked train are switched out. The laser energy is monitored at four places along the path as shown in Fig. 1.3. The monitors are Holgate units using silicon photodiodes (Type SGD - 040A) coupled to an integrating and peak hold circuit.

The energy incident on the target prior to the main pulse is measured by the prepulse monitor shown in Fig. 1.4 i). A typical output is shown in Fig. 1.4 ii). Prepulse levels greater than 10^{-4} times the main pulse power can be detected. The effects of prepulse energy on target behaviour is discussed in Chapter 8.

The beam intensity profile is recorded on Ilford 1Z emulsions for both near and far field distributions. The near field camera records the beam profile in a plane equivalent to that of the target chamber entrance window. The far field camera is able to record ten different planes in a region near the beam focus depending on the experimental requirements.

The back reflection energy monitor checks for the presence of hot spots greater than 3 times the average intensity in the retro-reflected beam.

1.5 Laser Beam Characteristics and Performance

The laser characteristics for these experiments are summarised in Table 1.1.

Table 1.1 Laser Characteristics

Wavelength	1.0642 μm	1.0642 μm
Pulse Duration (FWHM)	100 ps	1.8 ns
Energy (in each beam)	15 - 30 J	$\lesssim$ 100J
Peak Irradiance	10^{15}-10^{16} W cm^{-2}	10^{13}-10^{15} W cm^{-2}

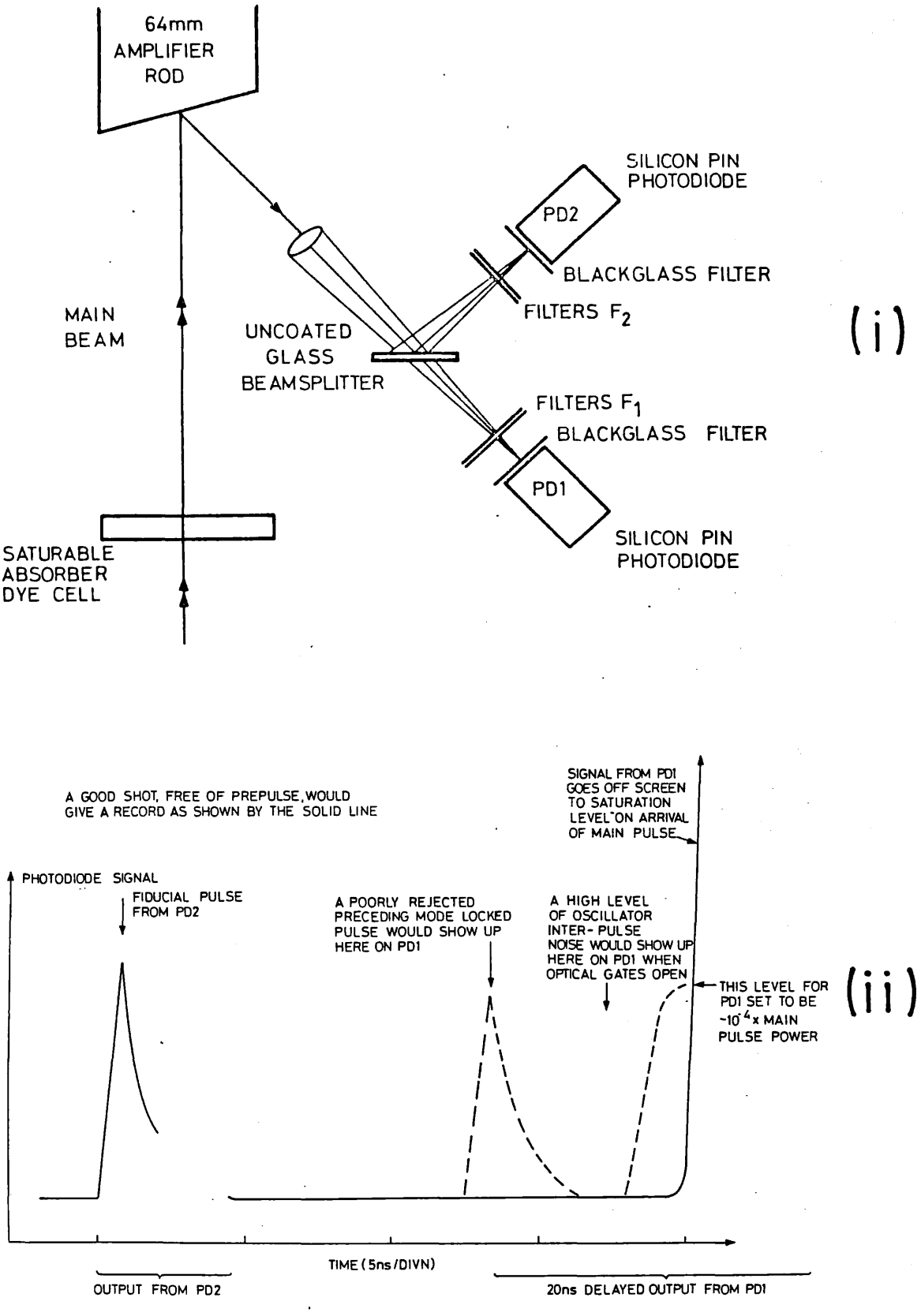

FIG. 1.4 - Prepulse monitor. i) Schematic layout. ii) Typical output.

The pulse duration is measured from the S - 1 streak camera records. In the Brillouin scattering experiment (Chapter 6), this is coupled to a Monospek grating spectrograph and the streak records give the line width of the laser, $\Delta\lambda = 1 - 2$ Å.

As well as prepulses, energy can be deposited on the target before the arrival of the main pulse due to amplified spontaneous emission (ASE). The ASE level is controlled by changing the concentration of the saturable dye cell until no target damage is observed when the amplifiers are fired in the absence of an oscillator pulse. The small signal transmission is 10% and the main pulse transmission is about 70% for the dye cell. The ASE level measured is about 100 μ J (1.15).

The far field camera shows that 50% of the total power is in the diffraction limited central Airy disc i.e. diameter = 30 μm (1.16). This best performance is generally degraded by thermal distortion in the amplifiers and by turbulence in the air flow along the beam path from the laser area to the target area.

A radial variation in the pump intensity distribution across the laser rods causes them to become slightly negative lenses. This causes the focal plane to shift by about 40 μm (1.15).

The discs have a more uniform pump intensity distribution and consequently cause little distortion of the beam during firing. After a shot, non-uniform thermal profiles exist which can cause optical distortion of the subsequent pulse unless a cooling period of at least 20 minutes is allowed between laser shots.

However, for the best steady state profiles, at least one hour's cooling is required, but this is the usual practicable interval between shots achieved in these experiments.

1.6 Target alignment and Focussing

The laser beam is taken to the target by a series of dichroic mirrors. For the short pulse experiments, the targets used are glass

microballoons, typically 50 - 100 μm in diameter and about 0.5 μm wall thickness, mounted on a 5.0 μm diameter glass stalk. These are purchased in bulk and selected for sphericity and wall uniformity (1.15). They are normally used with a thin (200 Å) aluminium coating for ease of alignment and focussing.

For the long pulse experiments, microballoons and microspheres in two different sizes are used, approximately 100 μm and 250 μm in diameter, to gauge the effects of target geometry and material Z on the backscatter measurements.

The target is positioned at the centre of the target chamber (shown in Fig. 1.5) and the tip of a conical surrogate target is used as a reference. The main beam axis is defined by the line passing through the target and replaceable cross wires mounted on the target chamber windows. A He-Ne laser is used for initial alignment and then a CW YAG laser is made collinear with this for focussing the target.

The main focussing lens (either a single element SORO lens or an achromatic doublet ICOS lens) is first centred on the alignment He-Ne beam. Then a small mirror is placed in contact with the rear surface (i.e. that nearest the target) of the lens to reflect the alignment beam. The tilt of the lens is adjusted until it is normal to the beam i.e. the alignment beam is retro-reflected.

The focussing of the target is performed using the telemicroscope system shown in Fig. 1.6. The target is placed in the focus of the He-Ne beam first, then, using the CW Nd:YAG laser, the target is moved until a strong, minimum size, symmetrical retro-reflected spot is observed on the focal plane telemicroscope TV monitor screen. Finally a small correction (40 μm) is applied for the change of focus produced in the amplifier rods when fired.

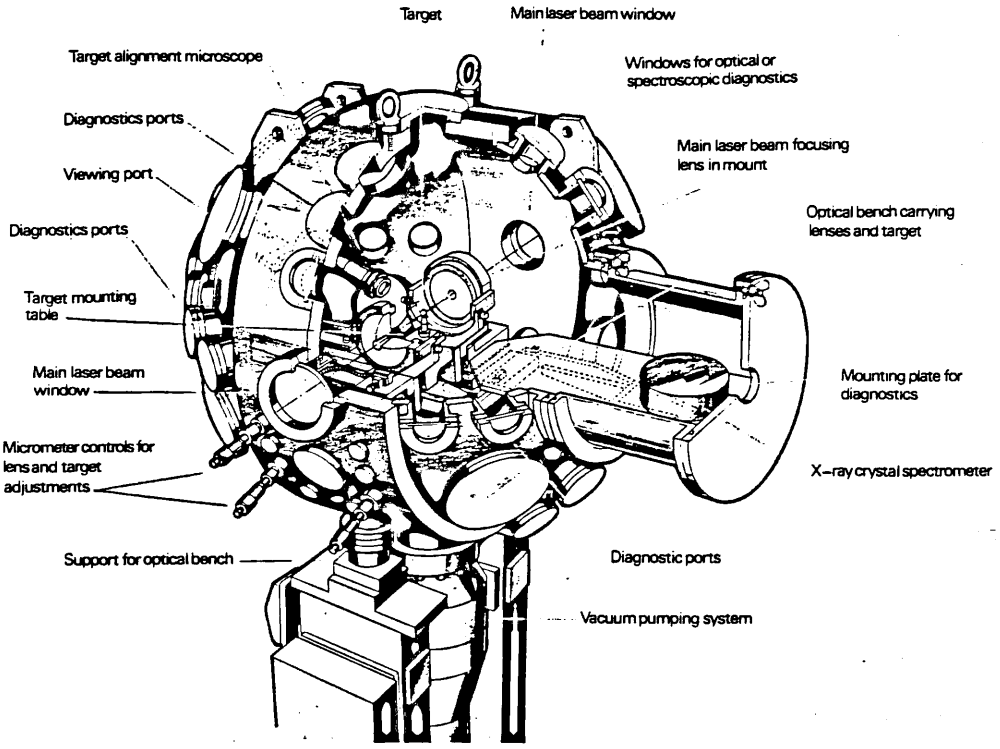

FIG. 1.5 - Target chamber.

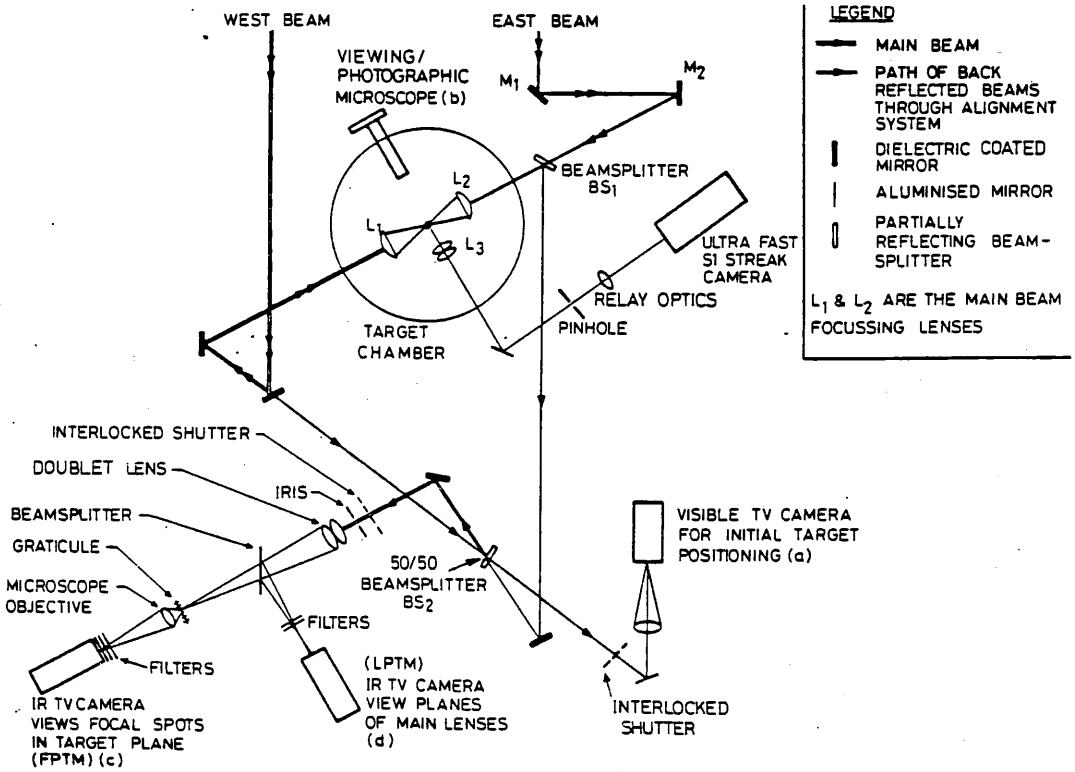

FIG. 1.6 - Target alignment and focussing system.

CHAPTER 2

THE PROPAGATION OF WAVES IN A PLASMA

2.1 Introduction

A plasma is a low density, ionized gas where the physical properties result mostly from long range Coulomb interaction and are, therefore, collective properties involving many particles simultaneously. This behaviour is analogous to that in a fluid, and like a fluid, a plasma can support many forms of oscillations. In a plasma which is located in an external field these oscillations can become amplified to a relatively high energy.

When a high power laser pulse is focussed onto a solid target a very dense plasma is formed very quickly. The light can interact directly with the plasma particles or with other waves in the plasma, which may be transverse (electromagnetic) or longitudinal (electrostatic or ion acoustic). The possible interaction processes and experimental evidence for their occurrence will be discussed in the next Chapter, but first, the behaviour of the various kinds of waves in plasmas will be reviewed briefly here.

Plasma waves in a regime where thermal motions are important have to be treated using a microscopic model such as the Vlasov theory. However, a more simple approach will be used here, resulting from fluid treatments for plasmas.

2.2. Plasma Parameters

In a many body system such as a plasma, much of the behaviour of the system can be described in terms of familiar macroscopic variables e.g. density, temperature, average velocity and pressure, which are related through the conservation laws for momentum and energy transport. However plasma physics also has its own concepts and terminology which may be less familiar.

For example, λ_{De} is the Debye length and is a measure of the sphere influence of a given test charge in a plasma.

$$\lambda_{De} = \left(\frac{T_e \, k_B \, \varepsilon_o}{n_e \, e^2} \right)^{1/2} \qquad \text{II-1}$$

Where T_e = electron temperature

k_B = Boltzman's constant

ε_o = permittivity of free space

n_e = electron density

e = electron charge

The length of time taken by an electron moving at thermal speed to travel a Debye length can be measured by the plasma frequency, ω_p. This is the natural frequency of the electrostatic oscillation of the electron resulting from a disturbance of the plasma charge neutrality.

$$\omega_p = \left(\frac{n_e \, e^2}{m_e \varepsilon_o} \right)^{1/2} \qquad \text{II-2}$$

Where m_e = electron mass

The plasma can be described by the distribution function, f, which is the number of particles per unit volume in six-dimensional phase space and is of Maxwellian form:

$$\bar{n} f(v) = \bar{n} \left(\frac{m_e}{2\pi \, k_B T_e} \right)^{3/2} e^{-\left(m_e v^2 / \, 2 k_B T_e \right)} \qquad \text{II-3}$$

Where $\bar{n} = \frac{N}{V}$ where N is the number of electrons and V the volume of the system.

In an inhomogeneous plasma, there will be regions of different densities i.e. an incident electromagnetic wave will encounter a density gradient. The steepness of this gradient will be given by the density scale length which is defined by $\left(\frac{1}{n_e}\frac{dn}{dx}e\right)^{-1}$. In an expanding plasma there exists a velocity gradient where the velocity scale length is defined by $v\ (\frac{dv}{dz})^{-1}$.

2.3 Waves in Plasmas

There are a large number of possible oscillations in a plasma and waves will propagate e.g. electric fields $\underline{E} = \underline{E}_o \exp\ (i\ (\underline{k}.\underline{x} - \omega t)\ )$. The frequency ω and the wave number k are related by a dispersion relation obtained from the plasma equations. The phase velocity of a wave is $v_p = \omega/k$ and the group velocity of a wave is $v_g = \partial\omega/\partial k$.

Most of the waves discussed in the following sections are small-amplitude waves whose amplitude is a linear function of the wave energy. The waves of interest in laser plasma interactions are ion-acoustic waves, electromagnetic waves and plasma waves, which are also known as electrostatic or Langmuir waves.

2.4 The Wave Equation

Maxwell's equations for a plasma may be written (2.2)

$$\underline{\nabla} \times \underline{E} = -\ \partial\underline{B}/\partial t \qquad \text{II-4}$$

$$\underline{\nabla} \times \underline{H} = \varepsilon_o\ \partial\underline{E}/\partial t + \underline{J} \qquad \text{II-5}$$

$$\underline{\nabla} \cdot \underline{E} = \rho_q/\varepsilon_o \qquad \text{II-6}$$

$$\underline{\nabla} \cdot \underline{B} = 0 \qquad \text{II-7}$$

Where $\underline{E}$ = electric field vector

$\underline{H}$ = magnetic field vector

ε_o = permittivity of free space

$\underline{J}$ = current density

ρ_q = charge density

$\underline{B} = \mu_o \underline{H}$ = magnetic flux density

μ_o = permeability of free space

The continuity of charge equation is obtained from II-5 and II-6.

$$\frac{\partial \rho_q}{\partial t} + \underline{\nabla}.\underline{J} = 0 \qquad \text{II-8}$$

The current density is related to the electric field by the conductivity $\underline{\sigma}$. For a particular angular frequency ω, Ohm's law may be written:

$$\underline{J}\ (\omega) = \underline{\sigma}\ (\omega).\underline{E}\ (\omega) \qquad \text{II-9}$$

The dielectric constant can be defined as:

$$\underline{\varepsilon} = 1 + \frac{\underline{\sigma}}{i\ \omega\ \varepsilon_o} \qquad \text{II-10}$$

Let both $\underline{E}$ and $\underline{H}$ vary in time and space as exp i $(\omega t - \underline{k}.\underline{r})$ where $\underline{k}$ is the propagation vector ($k = 2\pi / \lambda$), so equations II-4, II-5 and II-7 become:

$$\underline{\nabla} \times \underline{E} = -i\ \omega\ \mu_o\ \underline{H} \qquad \text{II-11}$$

$$\underline{\nabla} \times \underline{H} = i\ \omega\ \varepsilon_o.\underline{E} \qquad \text{II-12}$$

$$\underline{\nabla}.\ \underline{B} = 0 \qquad \text{II-13}$$

From equations II-8 and II-9 we have:

$$\nabla.(\varepsilon.E) = 0 \qquad \text{II-14}$$

The wave equation is obtained by taking the curl of equation II-11 and substituting for H from equation II-12:

$$\nabla \times (\nabla \times E) = \mu_o \varepsilon_o \omega^2 \varepsilon.E$$

$$= \left(\frac{\omega}{c} \right)^2 \varepsilon.E \qquad \text{II-15}$$

Where the velocity of light in free space, $c = (\mu_o \varepsilon_o)^{-\frac{1}{2}}$. Since both E and H vary as $\exp i(\omega t - k.r)$ equation II-15 can be written:

$$k \times (k \times E) + \left(\frac{\omega}{c}\right)^2 \varepsilon . E = 0 \qquad \text{II-16}$$

This is the general wave equation for a plasma and consists of three homogeneous equations in the components of E. The determinant of the coefficients $| D |$ must vanish if there is a solution i.e. if $E \neq 0 . | D | = 0$ is known as the dispersion relation and there may be more than one solution to the dispersion equation, each representing a different family of waves with different dispersion relations between ω and k. Solutions for the different types of waves are discussed in the following sections.

2.5 Longitudinal Oscillations

For longitudinal waves,

$$k \times E = 0 \qquad \text{II-17}$$

Hence in a cold plasma, the wave equation reduces to:

$$\varepsilon = 0 \qquad \text{II-18}$$

This solution corresponds to Langmuir oscillations at the plasma frequency $\omega = \omega_p$. They are dispersionless in a cold plasma and since the group velocity, $v_g = 0$, they do not propagate as longitudinal waves. However, they do involve an interchange of energy between the electric field and the kinetic energy of the particle motion. As the convection current density and the displacement current density cancel each other there is no net current in the plasma and hence no magnetic field.

In a warm plasma, the Langmuir oscillation is dispersive (as in this case ω varies nonlinearly with wavelength instead of being independent) and is a propagating wave. The dispersion relation is given by the solution of the Vlasov wave equation and is the well known Bohm-Gross equation (2.3):

$$\omega^2 = \omega_p^2 + \frac{3\, k_B\, T_e\, k^2}{m_e} \qquad \text{II-19}$$

Where k_B = Boltzman's constant

$$\omega = \omega_p \left(1 + \frac{3\, k_B\, T_e}{m_e\, \omega_p^2} \right)^{1/2}$$

$$\omega = \omega_p \left(1 + 3\, k^2 \lambda_{De}^2 \right)^{1/2} \qquad \text{II-20}$$

For a cold, field-free plasma, there is only one characteristic frequency, $\omega = \omega_p \left(1 + \frac{m_e}{m_i}\right)^{\frac{1}{2}}$, with no separate resonance at the ion-plasma frequency. However, when the electrons are warm, the low frequency limit solution ($\omega^2 << \omega_p^2$) gives:

$$\omega_{ia}^2 = \frac{k^2\, Z\, k_B\, T_e\, /\, m_i}{1 + k^2\, \lambda_{De}^2} \qquad \text{II-21}$$

This is the ion acoustic wave and it propagates at the ion sound speed which is between the electron and ion thermal speed:

$$\frac{\partial\omega}{\partial k} \simeq c_s = \left(\frac{k_B T_e}{m_i} \right)^{1/2} << \left(\frac{k_B T_e}{m_e} \right)^{1/2} \qquad \text{II-22}$$

The energy in the ion acoustic waves is shared between the electrostatic energy E^2 and the mechanical energy of the plasma particles oscillating in the low frequency electric fields. In order that the ion acoustic wave is not heavily damped, it can be shown that $T_e >> T_i$ (2.1).

2.6 Transverse Oscillations

For a transverse wave:

$$\underline{k} \cdot \underline{E} = 0 \qquad \text{II-23}$$

The non-trivial solution $\underline{E} \neq 0$ gives the dispersion relation:

$$\omega^2 = k^2 c^2 + \omega_p^2 \qquad \text{II-24}$$

These waves propagate in any direction in the plasma and are electromagnetic waves propagating in a dielectric medium. Their properties are very different from those of the electrostatic waves. They will transport energy even through a cold plasma at rest, at a speed equal to their group velocity:

$$v_g = \frac{\partial\omega}{\partial k} = \frac{k c^2}{\omega} = \frac{c}{\left(1 + \omega_p^2 / k^2 c^2 \right)^{1/2}} < c \qquad \text{II-25}$$

Their phase velocity is given by:

$$v_p = \frac{\omega}{k} = c \left(1 + \frac{\omega_p^2}{k^2 c^2} \right)^{1/2}$$

$$= \frac{c}{(1 - \omega_p^2/\omega^2)^{1/2}} > c \qquad \text{II-26}$$

which exceeds their speed in vacuum.

As $\omega_p \to 0$, the waves become $\omega = kc$ i.e. plane electromagnetic waves propagating in vacuum. At $\omega \simeq \omega_p$ a cut off occurs. The plasma frequency, ω_p, increases with increasing plasma density (equation II-2) hence, by the dispersion relation II-24, k^2 will decrease and the wavelength of the electromagnetic wave becomes longer. There will be a critical density, n_{CR}, such that k^2 is zero and for densities greater than this equation II-24 cannot be satisfied for any real k and the wave cannot propagate. This critical density occurs at $\omega = \omega_p$ so from II-2:

$$n_{CR} = \frac{\omega^2 m_e \varepsilon_o}{e^2} \qquad \text{II-27}$$

Since the wave has a spatial dependence exp (ikx) it will be exponentially attenuated if k is imaginary. The skin depth δ is as follows:

$$e^{ikx} = e^{-(k)x} = e^{-x/\delta} \qquad \text{II-28}$$

$$\delta = |k|^{-1} = \frac{c}{(\omega_p^2 - \omega^2)^{1/2}} \qquad \text{II-29}$$

A wave which behaves in the above manner is known as an evanescent wave.

2.7 Wave Damping

The plasma wave will grow until damped by one or more mechanisms. In a weakly ionised plasma the plasma waves will be damped by collisions between the electrons and any neutral particles. However, wave damping without energy dissipation by collisions is also possible by the mechanism

known as Landau damping: in a Maxwellian electron distribution more electrons are accelerated than slowed down, such that the wave loses energy to the electrons.

Non-linear saturation of plasma waves also exists: for example, it can be shown (2.4) that electrons with velocities close to the wave's velocity will be trapped by the wave. There is a continuous energy exchange between the wave and the electron trapped in the wave, which over a large time interval will average zero, but not if collisions between captured and free electrons are considered. This means that the wave eventually loses energy to the electrons and is damped. In a cold plasma the condition for electron trapping is given by:

$$v_E = v_P \qquad \text{II-30}$$

Where $v_E = e\,E\,/\,m_e\,\omega$ is the velocity of oscillation of the electron in the wave.

In a warm plasma, trapping occurs at smaller amplitudes as faster electrons are more easily brought into resonance, and the pressure force associated with the density fluctuation of the wave gives an additional acceleration to the electrons.

When the localised oscillating field becomes sufficiently intense that electrons can be accelerated through it in one oscillation period, a process called wave breaking occurs. Electrons which enter the oscillating field with the proper phase are efficiently heated, taking energy from the field and saturating its growth. Kruer (2.4) has shown that the amplitude of the oscillating field at wave breaking is:

$$\frac{e\,E}{m_e\,\omega} = \left(\frac{2\,e\,E_d\,L}{m_e}\right)^{1/2} \qquad \text{II-31}$$

where L : scalelength

Where E_d is the electric driving field.

Electrons are not the only possible resonant particles. If a wave has a slow enough phase velocity to match the thermal velocity of ions, ion Landau damping can occur. For example, ion acoustic waves are heavily Landau damped under certain conditions.

CHAPTER 3

LASER PLASMA INTERACTIONS

3.1 Introduction

The coupling of light energy to targets is an important component of laser fusion studies. The high temperature conditions existing in the plasma will reduce the collisional absorption process of inverse bremmstrahlung, whereby a free electron attains a more energetic state by absorbing a photon. However, even a collisionless plasma can be heated. This anomalous absorption arises because intense laser light incident across a variation in the plasma density can excite plasma waves. The electric fields associated with these waves can then accelerate and heat the plasma particles.

The density variation is due either to the overall density gradient caused by the plasma expansion (leading to resonance absorption), or density fluctuations associated with other plasma waves such as ion acoustic waves (giving rise to the parametric instability near n_{CR}, for example). How such instabilities occur can be understood by considering the effect of the ponderomotive force.

3.2 The Ponderomotive Force

The ponderomotive force is simply the radiation pressure in a plasma. Chen has shown (3.1) that the ponderomotive force is given by:

$$\underline{F}_{NL} = -\left(\frac{\omega_p}{\omega_o}\right)^2 \frac{\varepsilon_o}{2} \underline{\nabla} \langle E^2 \rangle \qquad \text{III-1}$$

Where the brackets denote a time average over the high frequency oscillations and ω_o = laser frequency

The ponderomotive force can drive both backscattering and electrostatic parametric instabilities. For example, consider a small (thermal level) density fluctuation associated with an ion acoustic wave. The light field will couple with the density fluctuation to drive a high frequency electric field associated with a plasma wave. In turn, this electric field couples with the light wave field to produce a fluctuation in the field pressure, which enhances the density fluctuation. Hence, instability is possible, leading to the growth of both plasma and ion acoustic waves provided $\omega_o \simeq \omega_p + \omega_{ia}$. This is known as the parametric decay instability.

3.3 Parametric Instabilities

The intense laser light can act as a pump driving other modes which may be transverse or longitudinal (electron plasma or ion acoustic) waves. Hence, some of the energy of the incident electromagnetic wave has been converted to other waves or parametric instabilities.

i.e. $T \rightarrow T'$, I and E III-2

Where T = laser photons denoted by subscript = t or o

T' = other photons = t'

I = phonons = ia

E = plasmons (Bohm-Gross) = e

They can be either 3-wave or 4-wave processes but must obey the usual frequency and wave number matching conditions:

$$\omega_o = \omega_1 + \omega_2 \qquad \text{III-3}$$

$$\underline{k}_o = \underline{k}_1 + \underline{k}_2 \qquad \text{III-4}$$

Where $\underline{k}$ = wave vectors and ω = frequencies and subscripts o, 1 and 2 denote pump and driven waves respectively. When multiplied by $\hbar$ equations III-3 and III-4 represent the conservation of energy and momentum. The energy given up by the pump wave to the daughter waves is in proportion to their frequencies:

$$\frac{W_o}{\omega_o} = \frac{W_1}{\omega_1} = \frac{W_2}{\omega_2} \qquad \text{III-5}$$

Where W = energy absorbed and equation III-5 is known as the Manley-Rowe relations.

The region in the plasma where the k- matching conditions are satisfied is known as the interaction region. The parametric instability may exist in two modes: as a convective instability or an absolute instability. The former is a spatially growing mode such that a wave packet of unstable modes will grow as it moves in space, but will not grow in time at a fixed point in space. The latter is a temporally growing mode which will grow in time at a fixed spatial point.

The following sections confine the discussion to cases where the laser is the pump wave. However, once large amplitude plasma and ion acoustic waves have been generated they can couple parametrically to each other to produce new frequencies. Therefore, a wide complex spectrum of longitudinal waves can develop in the plasma as in plasma turbulence. Fig. 3.1 shows the different regions in the plasma where specific instabilities may occur.

3.4 Light Absorption Processes in a Plasma

3.4.1. The Parametric Decay Instability

$$T \rightarrow E + I \qquad \text{III-6}$$

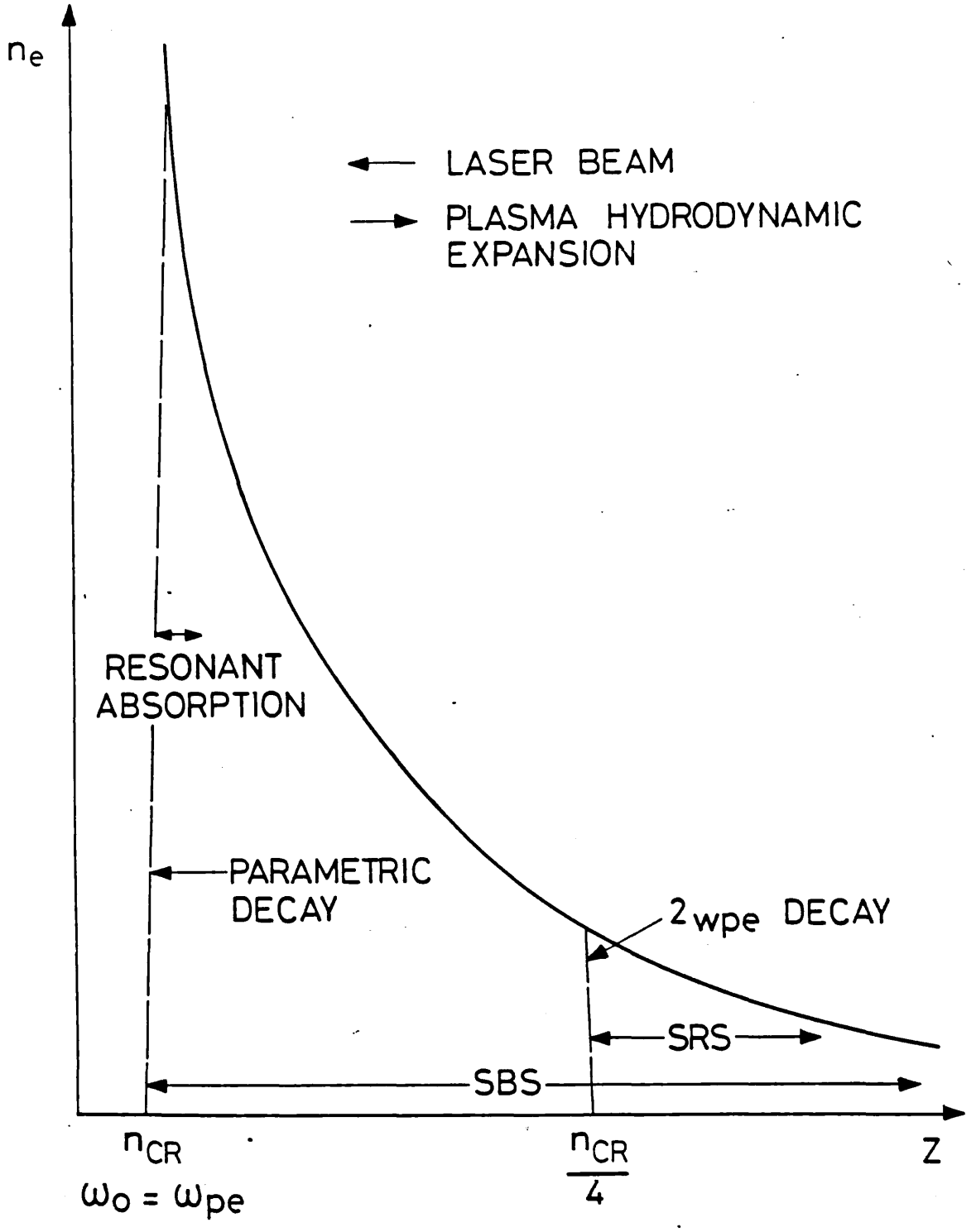

FIG. 3.1 - Interaction regions in a laser produced plasma.

The parametric decay of an electromagnetic wave with $\omega_o \simeq \omega_p$ into electrostatic perturbations has two possible branches. These are distinguished by the frequency of the ion acoustic wave generated. A zero frequency phonon signifies the oscillating two stream instability while a finite phonon frequency corresponds to the parametric decay instability.

The ω- and k- matching conditions are shown in Fig. 3.2. The dispersion relations are given by Chen (3.1).

$$\left.\begin{aligned} k_t^2 c^2 &= \omega_t^2 - \omega_p^2 && \text{a)} \\ 3 k_e^2 v_{th}^2 &= \omega_e^2 - \omega_p^2 && \text{b)} \\ k_{ia}^2 v_{ia}^2 &= \omega_{ia}^2 && \text{c)} \end{aligned}\right\} \qquad \text{III-7}$$

As the parametric decay process may be an important mechanism for absorbing laser light it has been studied for a variety of conditions by several authors. For example, Nishikawa (3.2) used hydrodynamic equations to obtain the threshold irradiance, and growth rate just above threshold for weak pump fields, allowing for damping and thermal motion.

The threshold for the parametric decay instability has been calculated by Perkins and Flick (3.3).

$$\left(\frac{v_E}{v_{th}}\right)^2 \simeq \frac{8}{kL}\left(1 + \frac{3T_i}{T_e}\right)\left(\frac{\upsilon_{ik}}{\omega_{ia}}\right)^{1/2} + 3\left(\frac{\upsilon_{ik}}{\omega_{ia}}\right)\left(\frac{\upsilon_{ek}}{\omega_p}\right) \qquad \text{III - 8}$$

Where υ_{ik} = ion collision frequency including Landau damping

υ_{ek} = electron collision frequency including Landau damping

T_i = ion temperature

T_e = electron temperature

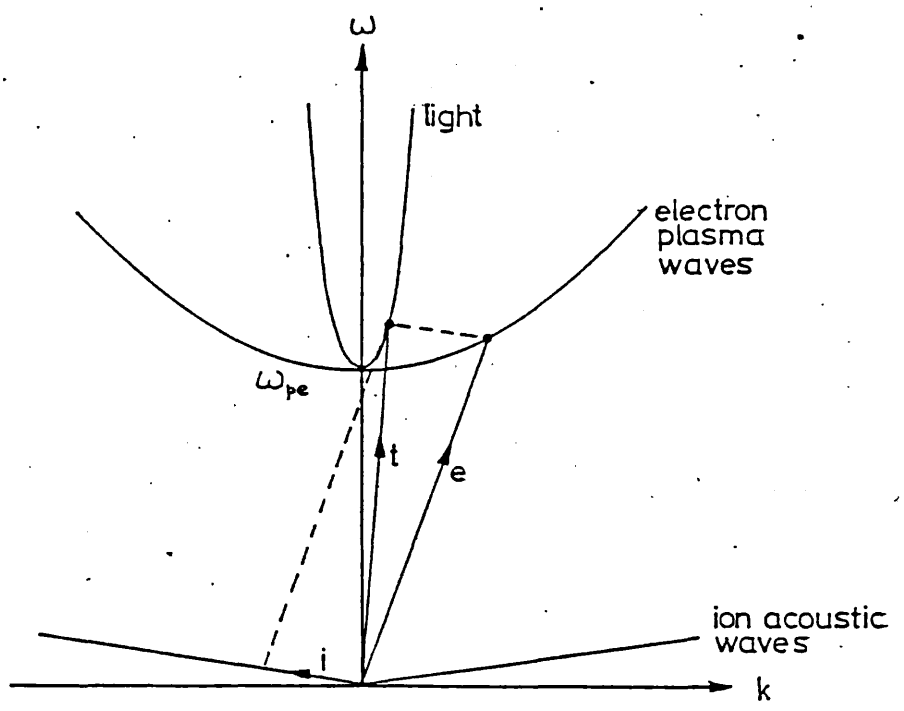

FIG. 3.2 - (ω,k) diagram for the parametric decay instability. The parallelogram construction ensures the matching conditions are satisfied.

Until recently the main experimental evidence for the occurence of the parametric decay instability came from microwave experiments. The decay of an electron plasma wave into other electron waves in a sodium plasma was investigated by Franklin et al (3.4) and the matching conditions were found to be consistent with theory.

However, the evidence in laser produced plasmas is less conclusive as it is not possible to measure the frequencies and wave numbers of the waves directly. Bobin et al (3.5) have inferred its occurence through the observations of second harmonic light and this is discussed in a later chapter.

3.4.2 Two Plasmon Decay

$$T \rightarrow E + E \qquad \text{III-9}$$

This is the process where the pump wave decays to give two plasma waves at the quarter critical density. The matching conditions are given by:

$$\left.\begin{aligned} \omega_t &= \omega_{e_1} + \omega_{e_2} \\ \underline{k}_t &= \underline{k}_{e_1} + \underline{k}_{e_2} \end{aligned}\right\} \qquad \text{III-10}$$

It should be noted that these cannot be satisfied in one dimension. The theory of this process has been described by several authors (3.6). Rosenbluth (3.7) gives the threshold for an inhomogeneous plasma:

$$\frac{1}{3} \left(\frac{v_E}{v_{th}}\right)^2 k_o L > 1 \qquad \text{III-11}$$

However, this expression assumes $k_e >> k_o$. For cases when this is not valid, Barr gives the following threshold (3.8):

$$\frac{1}{44}\left(\frac{v_E}{v_{th}}\right)^2 k_o L > 1 \qquad \text{III-12}$$

In practical units, for a Nd/glass laser equation III - 12 can be written

$$\Phi > 2.3 \times 10^{16} \frac{T_e}{L} \frac{(keV)}{(\mu m)} \quad W\ cm^{-2} \qquad \text{III-13}$$

For typical values of T_e = 4 keV and L = 25 μm

$$\Phi > 4 \times 10^{15} \quad W\ cm^{-2} \qquad \text{III-14}$$

The saturation of the two plasmon decay instability has been discussed by Langdon et al (3.9). The simulations suggest that the plasma waves generate short wavelength ion fluctuations which couple them to shorter wavelength, more strongly damped plasma waves. At the same time, profile self-steepening, caused by the ponderomotive force of these large amplitude plasma waves inhibits the instability. As the caviton (which is a local depression in the plasma) moves down the density gradient, the steepening relaxes and the instability can recur. These simulations show different timescales for these fluctuations depending on the value chosen for the mass ratio. For a realistic mass ratio , the period for the bursts of the instability is approximately 0.8 ps.

Most of the experimental evidence for the two plasmon instability has been inferred from observations of the $3\omega_o/2$ harmonic emission (see Chapter 9). Recently, Baldis (3.10) has reported the identification of fast electrons generated by the two plasmon decay process near the quarter critical density region.

3.4.3 Resonance Absorption

Resonance absorption is probably the most important of the anomalous absorption processes. This is the process where energy flows from the light wave into a resonantly driven electrostatic oscillation near the n_{CR} (where $\omega_o \simeq \omega_p$), thus heating the electrons.

Consider an electromagnetic wave incident on a plasma with a density gradient as in Fig. 3.3 a. When the direction of the incident beam is parallel with the density gradient, the wave penetrates up to the critical density (being partially absorbed in transit) and is reflected along its own path. However, when the direction of the incident wave is oblique onto the plasma boundary, it is continuously refracted by the layered plasma (as shown in Fig. 3.3 b). This refraction increases until a turning point is reached:

$$\omega_p^2 = \omega_o^2 \cos \phi_i \qquad \text{III-15}$$

Where ϕ_i = angle of incidence

One of the characteristics of resonance absorption is its polarisation dependence. When the electric field vector is parallel with the plane of incidence (defined by the incident and reflected rays), the light is said to be p-polarised. The variation of the field magnitude with depth is similar to that for normal incidence, but the change from oscillation to exponential behaviour now occurs at the turning point. However, tunnelling of the wave through to the critical density occurs and at the critical density resonant electrostatic oscillations are excited as shown in Fig. 3.4 ii). The extent to which this occurs depends on ϕ_i.

For the case of "s" polarisation, when the E-vector is perpendicular to the plane of incidence some tunnelling can still occur, but no resonance is allowed and electrostatic waves are not driven (see Fig. 3.4 i).

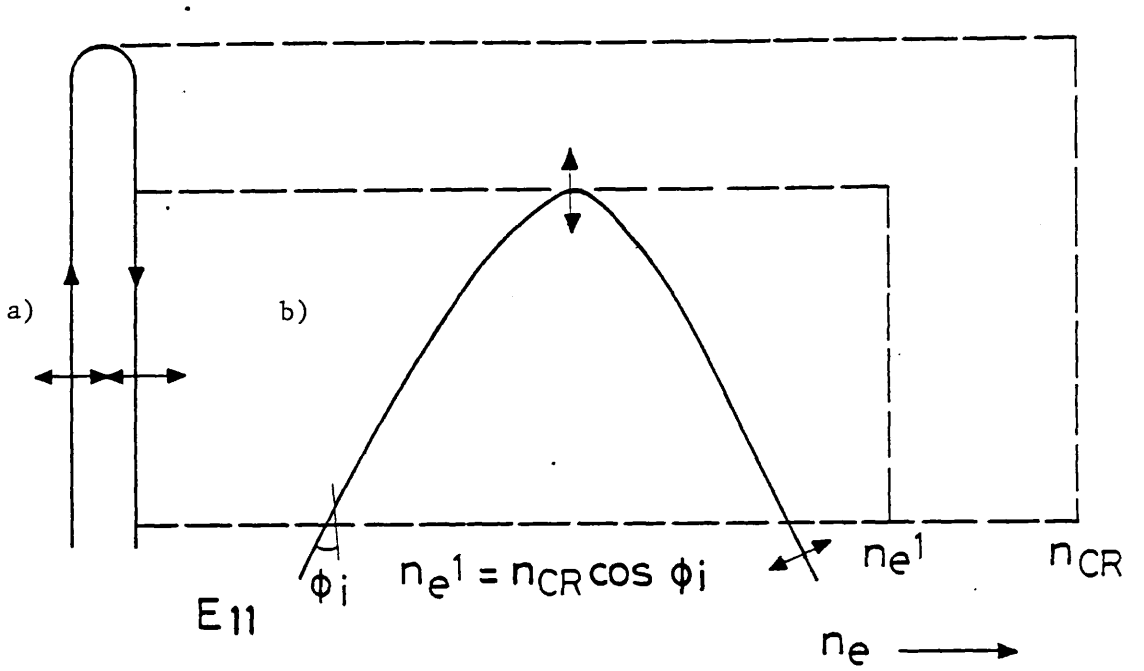

FIG. 3.3 - Normally and obliquely incident e.m. wave on a density gradient.

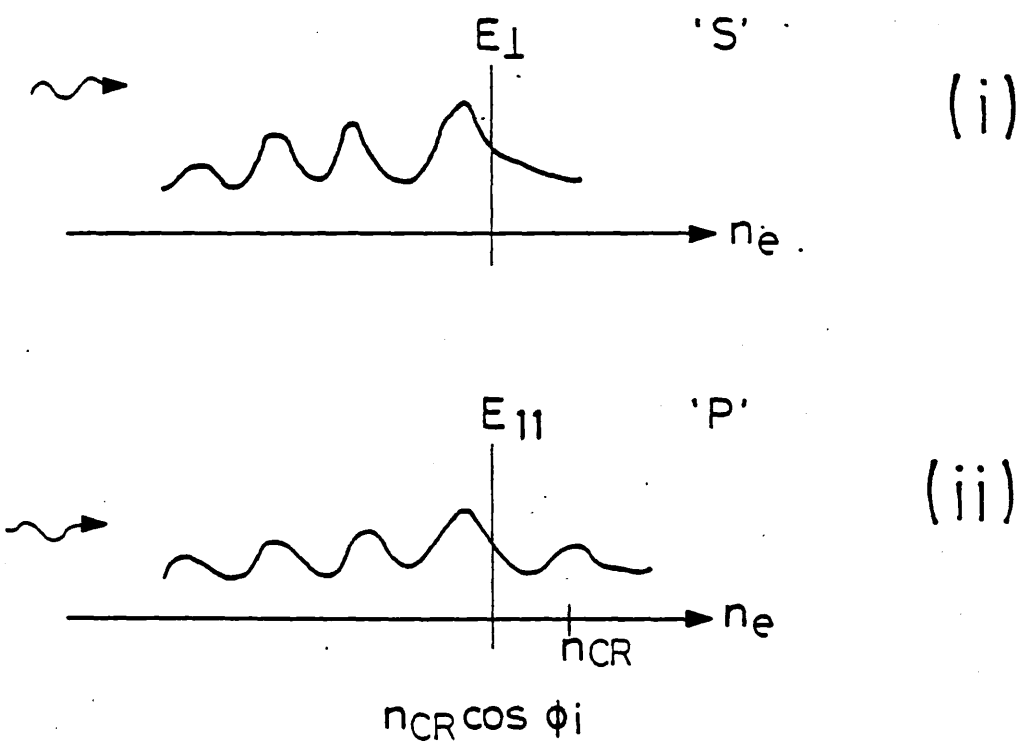

FIG. 3.4 - Tunnelling of e.m. wave. i) 's' polarisation. ii) 'p' polarisation.

Therefore, resonance absorption occurs only for p-polarised light. The amplitude of the resonant driving E-field (E_D) is given by (3.11)

$$E_D = \frac{E_o \, \phi(\tau)}{(2\pi k_o L)^{1/2}} \qquad \text{III-16}$$

Where $\tau = k_o L^{1/3} \sin \phi_i$

$\phi(\tau)$ = dimensionless parameter given by Ginzburg

$L = \dfrac{n_{CR}}{(dn_{CR} / d_z)}$ $n_e = n_{CR}$ for linearly varying density

The amplitude of the driven electron plasma waves is limited by convection, electron trapping or Landau damping when they travel down the density gradient. The generation of these resonant plasma waves causes local density steepening by the ponderomotive force. As this lowers the value of the scalelength L, it enhances resonance absorption.

As well as enhancing absorption, the process produces fast electrons which may cause preheat in the core. The absorption coefficient is normally independent of laser irradiance so resonance absorption is a linear process and has no threshold. However, at sufficiently high irradiances, the resonant plasmons may couple nonlinearly to other plasmons to create a more complex model. Optimum absorption occurs for an angle of incidence ϕ_{max} defined by (3.11).

$$(k_o L)^{1/3} \sin \phi_{max} \simeq 0.6 \qquad \text{III-17}$$

Hence the significance of resonance absorption depends strongly on the value of the density gradient scalelength near the critical density. If $\omega_o L/c$ is large, this absorption is effective only for a narrow band of angles. If $\omega_o L/c \lesssim 10$, resonance absorption will occur for a broad range of angles.

There have been many recent laser plasma experiments to investigate the polarisation and the angular dependence of light absorption (3.12).

As an example, the experiment by Manes et al (3.13) is described: 1.06 μm laser pulses of 30 ps duration were focussed by an f/10 lens onto planar parylene discs with irradiances in the range 10^{15} - 10^{16} Wcm^{-2}. The target was enclosed in a box calorimeter which together with calorimeters to collect the back reflected and transmitted light, allowed an accurate measurement of light absorption with angle and polarisation. The results showed a clear peak in absorption in p - polarisation at approximately 20^{o}, but no such peak is observable in s - polarisation, thus demonstrating the expected polarisation and angular dependence.

All these experiments confirm that resonance absorption is an important process in the absorption of intense laser light. However, for a more quantitative understanding of the process, the effects of critical surface rippling (3.14), short wavelength ion turbulence and self-generated magnetic fields must be considered.

3.5 Light Scattering Processes in a Plasma

3.5.1 a) Stimulated Brillouin Scattering

$$T \rightarrow T' + I \qquad \text{III-18}$$

From the Manley-Rowe relations, it can be seen that most of the energy will be in the reflected wave.

Fig. 3.5 shows the ω - k matching conditions and the following equations give the dispersion relationships:

$$\left.\begin{aligned} k_t^2 c^2 &= \omega_t^2 - \omega_p^2 \quad \text{a)} \\ k_{t'}^2 c^2 &= \omega_{t'}^2 - \omega_p^2 \quad \text{b)} \\ k_{ia}^2 v_{ia}^2 &= \omega_{ia}^2 \quad \text{c)} \end{aligned}\right\} \qquad \text{III-19}$$

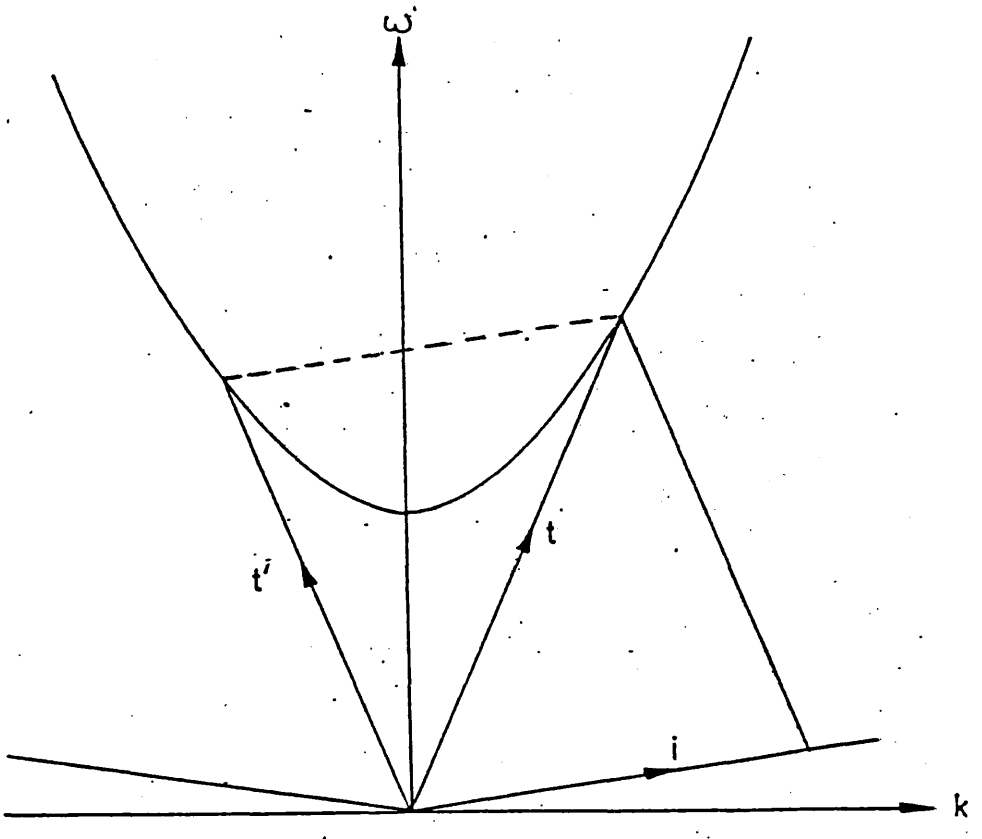

FIG. 3.5 - (ω,k) diagram showing matching conditions for stimulated Brillouin backscatter.

The threshold for the Brillouin instability has been calculated by Rosenbluth, White and Liu (3.15):

$$\tfrac{1}{8} \left(\frac{v_E}{v_{th}}\right)^2 \left(\frac{\omega_p}{\omega_o}\right)^2 k_o L_u > 1 \qquad \text{III-20}$$

Where L_u = velocity gradient scale length

In a convenient form given by Evans (3.16):

$$\Phi > \frac{T_e}{\lambda_o \beta L} \times 10^{13} \ \text{W cm}^{-2} \qquad \text{III-21}$$

where T_e is in eV, λ_o in μm and $\beta = \left(\frac{\omega_p}{\omega_o}\right)^2 = \frac{n_e}{n_{CR}}$

For the case of a Nd/glass laser, λ_o = 1.06 μm and taking typical values of T_e = 1000 eV and L = 100 μm

$$\Phi > 3 \times 10^{14} \ \text{W cm}^{-2} \qquad \text{III-22}$$

Clearly, a long scalelength will lower the threshold as will the operation of the instability near the critical density. It is worth considering extreme cases in terms of matching k vectors. The lowest value of k which can produce backscatter is that for which $k_{t'}$ is just below zero. When $k_{t'} = 0$ equation III-19 shows that $\omega_{t'} = \omega_p$, $k_t = k_{ia}$ and $\omega_t = \omega_{ia} + \omega_p$, so:

$$\left.\begin{aligned} k_{ia\ min} &\simeq 2\, v_{ia}\, \omega_p / c^2 \\ \omega_{ia\ min} &\simeq 2\, v_{ia}^2\, \omega_p / c^2 \end{aligned}\right\} \qquad \text{III-23}$$

Since, $v_{ia} \ll c$, the Brillouin instability can operate at all densities up to:

$$n_e = n_{CR} \left(1 + \frac{4 v_{ia}^2}{c^2}\right)^{-1} \qquad \text{III-24}$$

For matching conditions away from n_{CR}, $k_{ia} \simeq 2k_t$, so from equations III-19b) and III-19c)

$$\frac{\omega_{ia}}{\omega_t} \sim \frac{2v_{ia}}{c} \left(1 - \frac{n_e}{n_{CR}}\right)^{1/2} \qquad \text{III-25}$$

3.5.1 b) Spectral Characteristics of Stimulated Brillouin Scattering

The backscattered wave will be red shifted due to the generation of the ion acoustic wave, but there will also be a Doppler shift to the blue due to the motion of the ablating material. The Brillouin shift can be written:

$$\frac{\Delta \lambda_B}{\lambda_o} = \frac{\omega_{ia}}{\omega_o} = \frac{2 k_o v_{ia}}{\omega_o} = \frac{2 v_{ia}}{c} \qquad \text{III-26}$$

where v_{ia} = ion acoustic phase velocity = $\left(\frac{Z k T_e}{M_i}\right)^{1/2}$

The Doppler shift can be written as:

$$\frac{\Delta \lambda_D}{\lambda_o} = - \frac{2 v_a}{c} = - \frac{2 M v_{ia}}{c} \qquad \text{III-27}$$

where M = Mach number of flow
v_a = ablation velocity

The net shift is then given by:

$$\frac{\Delta \lambda}{\lambda_o} = \frac{2 v_{ia}}{c} (1 - M) \qquad \text{III-28}$$

Hence the shift is to the red if the flow is subsonic and to the blue, if it is supersonic.

3.5.1 c) Saturation of the Brillouin Instability

As laser plasma experiments move to longer pulse durations, resulting in larger amounts of underdense plasma, stimulated Brillouin scattering may become a severe light reflection problem. So, it is important to know the saturated level of the Brillouin instability.

The ion wave generated by the Brillouin instability saturates either by ion trapping or Landau damping. Generally, the wave will first saturate by ion trapping which will heat the ions and strong Landau damping will occur when the ion temperature approaches the electron temperature.

There is some theoretical evidence from Evans (3.16) that when the ablation speed is approximately the ion sound velocity, Brillouin scattering is only limited by ion trapping, as the equilibrium ion temperature is too low to produce significant ion Landau damping. This would lead to large reflectivities in the underdense plasma, especially in the case of short wavelength generated plasmas because of their large critical density. Evans (3.16) has shown that a 1.06 μm laser would produce 100% backscatter given a large enough volume of underdense plasma.

The previous experimental evidence for the Brillouin instability is discussed in Chapter 6.

3.5.2 Stimulated Raman Scattering

$$T \rightarrow T' + E \qquad \text{III-29}$$

The instability is strongest when E is near resonance with the local plasmon frequency. i.e. $\omega_{t'} \sim \omega_t - \omega_p$. For the propagation of the scattered photon, $\omega_{t'} > \omega_p$, so $\omega_p \lesssim \omega_t$. Hence the Raman instability will only operate at densities up to quarter critical. Therefore, from the Manley-Rowe relations, up to half the incident laser energy may be transferred to the plasma, with the rest being reflected. For minimum

Landau damping, $k\lambda_{De}$ must be as small as possible, so Raman scattering will occur as close as possible to the quarter critical especially as its threshold has its minimum value there.

Fig 3.6 shows the ω - k diagram for Raman scattering. The matching conditions are given by the following equations:

$$\left.\begin{aligned} \omega_t &= \omega_e + \omega_{t'} \\ \underline{k}_t &= \underline{k}_e + \underline{k}_{t'} \end{aligned}\right\} \qquad \text{III-30}$$

The threshold laser electric field required for instability to grow is expressed in terms of the electron quiver velocity $v_E = \frac{e\,E}{m_e\,\omega}$. For a homogeneous plasma:

$$\frac{\underline{v}_E^2}{c^2} = \frac{2\,\omega_p^2}{\omega_t^2}\,\frac{\gamma_e}{\omega_p}\,\frac{\nu_{ei}}{\omega_t} \qquad \text{III-31}$$

Since $\frac{\omega_p^2}{\omega_t^2}\,\frac{\nu_{ei}}{2}$ is the damping rate γ_t for the laser light:

$$\frac{\underline{v}_E^2}{c^2} = \frac{4\,\gamma_t\,\gamma_e}{\omega_t\,\omega_p} \simeq \frac{8\,\gamma_t\,\gamma_e}{\omega_t^2} \qquad \text{III-32}$$

In an inhomogeneous plasma, the plasma wave will move away from the interaction region and be rapidly Landau damped, hence:

$$\frac{\underline{v}_E^2}{c^2} \simeq \frac{1}{k_t L} \qquad \text{III-33}$$

The frequency of the scattered photon will be given by the frequency matching conditions (equation III-30) and the condition that the scattered wave is at the cut off density.

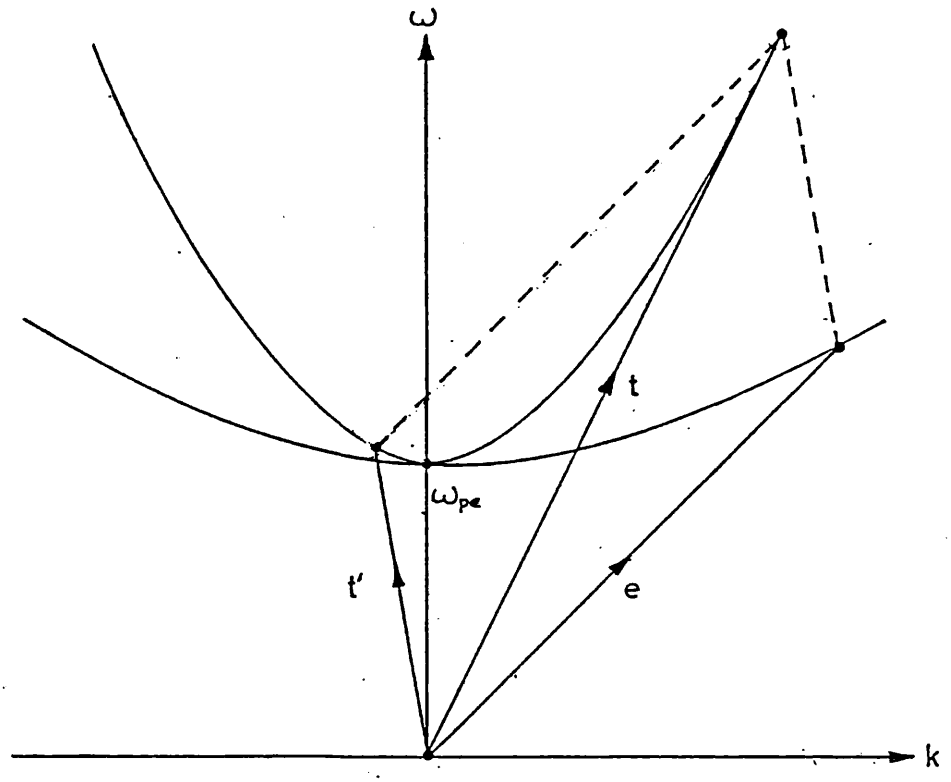

FIG. 3.6 - (ω,k) diagram showing matching conditions for stimulated Raman backscatter.

$$\omega_{t'} + (\omega_{t'}^2 + 3\, k_e\, v_{th}^2)^{1/2} = \omega_t \qquad \text{III-34}$$

where v_{th} = electron thermal velocity

Due to thermal corrections:

$$\omega_{t'} < \frac{\omega}{2}t \qquad \text{(cold plasma result)} \qquad \text{III-35}$$

Defining $\Delta\omega = \frac{\omega}{2}t - \omega_{t'}$ and assuming $\Delta\omega \ll \omega_t$, we obtain:

$$\frac{\Delta\omega}{\omega_t} = \frac{9}{8}\,\frac{v_{th}^2}{c^2} \qquad \text{III-36}$$

or $$\frac{\Delta\omega}{\omega_t} = \frac{T_e\ (\text{keV})}{454} \qquad \text{III-37}$$

Like the Brillouin instability, Raman scattering is favoured by the large regions of underdense plasma expected to occur when longer pulselengths are used for more realistic fusion research. However, not only will it reflect the laser light, but it may also cause pre-heating of the target by the generation of fast electrons. Simulations (3.17) have shown that the heated electron distribution is approximately Maxwellian, with a temperature given by $(m_e/2)\, v_p^2$ where v_p is the phase velocity of the electron plasma wave.

Both stimulated Raman scattering and the two plasmon decay instability can generate $\omega_o/2$ plasmons at the quarter critical density layer, which can give rise to $3\omega_o/2$ harmonic emission (described in Chapter 8), so its observation is not taken to be clear cut evidence for the Raman instability. However, the Raman process generates $\omega_o/2$ harmonic emission directly and recently there have been two reports of

its detection. The first by Phillion (3.18) used indium antimonide (In As) detectors cooled to 77°K. The $\omega_o/2$ spectrum from high Z targets irradiated by a Nd/glass laser was obtained by using selective changes of band pass filters for a multi-shot experiment. Although it was a crude measurement, a spectrum broadened to the blue was obtained.

The second report was by Elazar, Toner and Wooding (3.19). Again, a Nd/glass laser was used on plane targets, this time of varying Z. An In As photovoltaic detector was also used, but at room temperature. They observed $\omega_o/2$ harmonic emission with an energy of approximately 10^{-7} times the incident light energy, increasing with irradiance.

3.6. Density Profile Steepening Effects

As well as being the physical basis for these plasma instabilities the ponderomotive force also causes density profile steepening. Calculations by Kruer (3.20) predict steepening of the density profile near the critical density surface due to the ejection of plasma by the ponderomotive force of the intense localised electrostatic field. The ejected plasma expands towards the vacuum, leaving a locally steepened density profile which is supported by the pressure of both the localised electrostatic wave and the reflecting light wave.

This steepening affects the scalelength near the critical density, thus influencing the mix of absorption processes and the hot electron temperature. In particular, resonance absorption becomes important for a wide range of angles of incidence, while parametric instabilities will be strongly limited since there will now be only a very small region of plasma in which they can operate. Finally, the heated electron energies due to the resonantly generated waves are not strongly reduced by steepening, as the amplitude of the resonantly driven field decreases as the profile steepens.

The profile steepening has been confirmed by interferometric measurements of the density of a laser heated plasma (3.21).

Profile steepening also occurs in the underdense plasma but here it is caused by the ponderomotive force due to the intensity profile of the incident light. At the quarter critical, both stimulated Raman scattering and two plasmon decay are inhibited by decreasing scalelength, but the former more so than the latter (3.15). This is probably the reason why stimulated Raman scattering has not been observed experimentally until recently, as it requires large underdense plasmas.

Stimulated Brillouin scattering is also inhibited by decreasing scalelength, but it is affected by multi-dimensional effects as well. For example, a perturbation in the intensity profile of the incident light creates a depression in the plasma density via the ponderomotive force. This density depression then refracts the light inward, increasing the intensity perturbation, thus leading to the filamentation instability. This instability has a smaller growth rate than the Brillouin instability and may inhibit it by being the dominant mechanism. However, little is known about the competition of these two effects in the non linear state.

These effects caused by density profile steepening also illustrate that these interactions cannot be considered in isolation, and that there will be interactions between the interactions (3.22). For example, if the Brillouin instability is very strong, it will reflect light before it reaches the n_{CR} , thus affecting all the instabilities operating at higher densities.

CHAPTER 4

The Performance of the Streak Camera in the Picosecond Region

4.1 Introduction to Pulse Measurement Techniques

The earliest methods capable of picosecond time resolution rely on non-linear techniques, which involve deconvolution to obtain the pulse width. Typical processes include second (4.1) and third (4.2) harmonic generation, two (4.3) and three (4.4) photon fluorescence, four photon parametric mixing (4.5) and the optical Kerr effect (4.6). The two most popular are two photon fluorescence, which has an inherent time resolution of $\sim$0.2 ps (4.7) and the optical Kerr effect shutter, which has a time resolution of $\sim$2 ps (4.8). Neither are suitable for laser produced plasma studies as they require multi-shot experiments.

Photoemissive devices are suitable for single shot measurements. The simplest is the photodiode and oscilloscope combination which is capable of 60 ps time resolution (4.9) limited by the risetime of the combination. The risetime restriction is overcome in the image converter streak camera, which was first used for high speed photography by Courtney-Pratt in 1949 (4.10) who obtained a time resolution of about 0.1 μs. Since then, streak cameras possessing picosecond time resolution have been developed by several groups (4.11) and Bradley and Sibbett (4.12) have reported sub-picosecond time resolution from their Photochron II streak camera.

4.2 Description of the Image Converter Streak Camera

The basis of the system is the image converter tube, which is an evacuated glass tube containing a photocathode, electron accelerating and focussing fields and a phosphor screen, as shown in Fig. 4.1. When used as a component of a high speed camera the electronic image can be

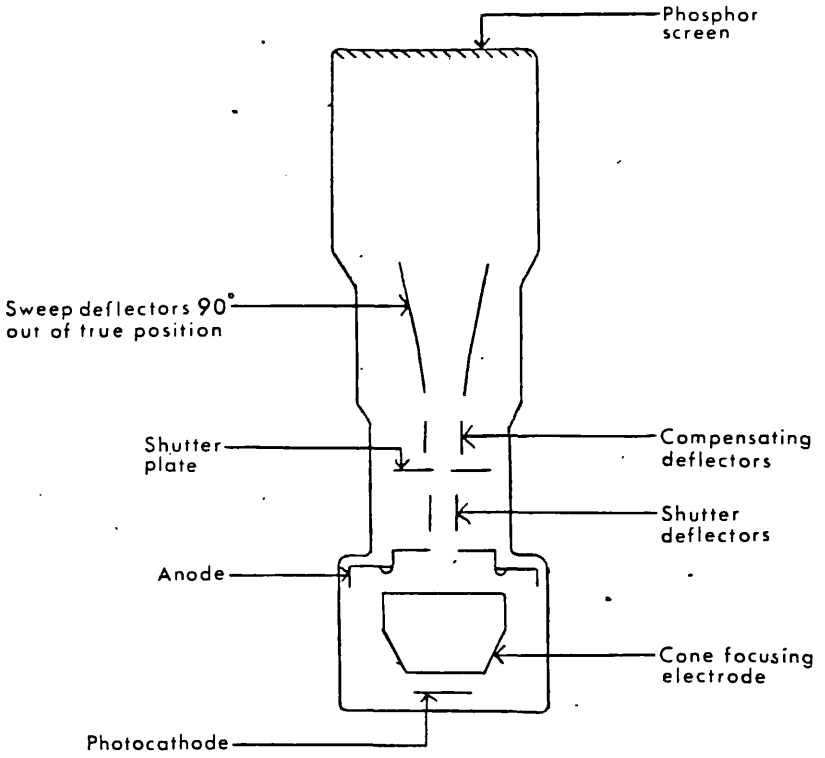

FIG. 4.1 - Image converter streak tube.

interrupted or deflected, or both, at up to picosecond timescales.

For streak operation, a narrow slit is placed in front of the image tube and is focussed onto the photocathode by a lens. The electron beam is then swept across the phosphor screen by applying a fast linear voltage ramp across a pair of deflection plates in a drift equipotential section of the image tube. The temporal information of the electron image as it is relayed through the image tube is thus preserved and the temporal variation of intensity is displayed on the phosphor as a spatial distribution in intensity in the direction of the streak.

4.3 Theoretical Time Resolution Limit of a Streak Camera

The theoretical limits of the electron optical image converter streak camera's performance have been investigated by Zavoiskii and Fanchenko (4.13). They considered a conventional design where electrons emitted by the photocathode are accelerated and focussed by an electron optical system. Before striking the fluorescent screen, the electrons traverse a region of rapidly rotating electromagnetic field such that the image is swept out in time; a circular sweep is usually the most suitable. If the period of rotation of the field is T, the radius of the circular sweep on the screen is R, and the resolution of the image is δ, the minimum resolved time interval is given by:

$$\Delta\tau_{sweep} = \frac{T}{2\pi R\delta} \qquad \text{IV - 1}$$

Taking typical values of $T = 10^{-10}$s, R = 5 cm and δ = 300 line pairs cm^{-1}, we have:

$$\Delta\tau_{sweep} = 10^{-14}\text{s} \qquad \text{IV - 2}$$

Generally, $\Delta\tau$ can be enhanced by reducing T or increasing $R\delta$. However, there are a number of physical processes which limit the

resolving power. The first is electronic chromatic aberration, which limits the minimum duration of an electron pulse at the phosphor screen to:

$$\Delta\tau_{min} = \left(\frac{h}{eE_o v_o} \right)^{1/2} \qquad \text{IV - 3}$$

Where E_o = electric field near photocathode

v_o = initial velocity of the electron

For $E_o = 100 \text{ kV cm}^{-1}$

$$\Delta\tau_{min} = 2 \times 10^{-14} \text{ s} \qquad \text{IV - 4}$$

Another important factor which limits the time resolution is the finite thickness of the photocathode which leads to the spread of the emission times of the photoelectrons:

$$\Delta\tau \simeq d/v_o \qquad \text{IV - 5}$$

for $d \simeq 10^{-6}$ cm and $v_o \simeq 10^{8}$ cm s^{-1}

$$\Delta\tau_d \simeq 10^{-14} \text{ s} \qquad \text{IV - 6}$$

A necessary condition for obtaining a short pulse is that the size of the source light must be sufficiently small:

$$\frac{\ell}{c} < \Delta t \qquad \text{IV - 7}$$

where ℓ is the diameter of the source

For $\Delta t \simeq 10^{-14}$ s, $\ell < 3\mu m$

The imaging optics should also be such that they do not stretch the pulse:

$$\frac{\Delta s}{c} < \Delta t \qquad \text{IV - 8}$$

where Δs is the difference in optical paths from the light source to the photocathode for different frequencies in the spectrum of the pulse. Hence, the input optics must be well achromatised and corrected for spherical aberration.

Overall, the above analysis concludes that the ultimate time resolution of the system is due to the variation in the initial energies of the photoelectrons given by equations IV - 5 and IV - 6 i.e. $\simeq 10^{-14}$s.

4.4 Practical Time Resolution Limit of a Streak Camera

In a practical system, there is one other important consideration - that of dynamic range. This is defined as the region between $I_{min} \rightarrow I_{sat}$, where I_{min} is the minimum photocurrent required to produce a detectable exposure on the recording film and I_{sat} is the maximum photocurrent which can be drawn from the photocathode before there is a serious loss in spatial resolution and the onset of geometric distortion.

Schelev, Richardson and Alcock (4.14) have calculated the maximum current density to be 0.1 A cm^{-2} assuming conditions within the tube correspond to a circularly symmetric electron beam converging from a 10 mm diameter cathode to a 1 mm cathode aperture, located $\sim$ 70 mm away, where the behaviour of the beam can be described by:

$$r_{min} = r_o \, e^{-\sigma} \qquad \text{IV - 9}$$

where r_{min} = beam radius at anode

r_o = beam radius at cathode

$\sigma = 3.3 \times 10^{-5} \left(\frac{V_a^{3/2}}{I}\right) \tan^2 \omega$

V_a = anode voltage

ω = angle between converging beam and axis

In an interval of 10^{-12}s, this corresponds to the emission of 6×10^{5} photoelectrons cm^{-2} from the photocathode. Assuming a spatial resolution of 10 lp mm^{-1}, this gives only 60 electrons in each resolution element. Hence such a camera would have limited dynamic range. So, although the ultimate temporal resolution is $\sim 10^{-14}$s, the practical requirements of a dynamic range of at least 10, results in a resolution of the order of 10^{-12}s.

4.5 Measurement of an Ultrashort Pulse Width Using a Streak Camera

Schelev has shown (4.14) that there are three major contributions to the half width τ of the recorded profile at the output of a streak camera, which for a gaussian pulse, are connected by the following equation:

$$\tau = (\tau_1^2 + \tau_2^2 + \tau_3^2)^{1/2} \qquad \text{IV - 10}$$

1. The half width of the incident pulse, τ_1
2. The time taken for the deflected electron beam to scan a spatial element of the phosphor screen,

$$\tau_2 = \frac{1}{v\delta} \qquad \text{IV - 11}$$

where v = streak velocity in $cm\ s^{-1}$
δ = spatial resolution at phosphor screen in line pairs cm^{-1} (lp cm^{-1})

3. The total transit time for the electrons to travel from the photocathode to the screen.

$$\tau_3 = \frac{m\Delta u}{eE} \qquad \text{IV - 12}$$

where Δu = half width of initial longitudinal velocity distribution
E = electric field at photocathode

e = electronic charge

m = electronic mass

An instrumental time limit can be defined:

$$\tau_{inst} = (\tau_2^2 + \tau_3^2)^{1/2} \qquad \text{IV - 13}$$

for $\tau \simeq \tau_1$, τ_{inst} must be minimised, by reducing τ_3 and maximising both the streak velocity and spatial resolution.

4.6 High Intensity Effects

The high intensity lasers used for plasma interaction studies will obviously pose a severe problem for the dynamic range capabilities of streak cameras. Some of the causes for the limited dynamic range of streak cameras are investigated below.

The photon energy density required to give a particular exposure level on the recording film is independent of the time for which the tube is conducting. Hence, under streak conditions, a much higher photocurrent is drawn from the cathode than in the case of static illumination. This causes several effects as reported by Ahmed, Gale and Key (4.15):

1. The resistance of the photocathode rises in value at its centre, resulting in a distortion of the distribution of the potential near the cathode. This affects the electrostatic lens in the initial stage of the tube, producing defocussing which results in a loss of spatial resolution and the appearance of geometric distortion.
2. Space charge builds up near the photocathode when large currents are taken from the cathode, leading to a reduction in the effective acceleration field. In the limit, this leads to photocathode saturation.

3. The electron optics of the image tube system produces an inverted image at the phosphor screen, so that electrons must cross the longitudinal axis of the tube. In the cross-over region the charge density is at a maximum, and the electrons suffer a mutual Coulomb repulsion effect, resulting in loss of spatial resolution and image distortion.

Both the space charge effects near the photocathode and in the cross-over region obey the Child-Langmuir three-halves power law ($\propto E^{3/2}$).

To avoid these high intensity effects, the photocurrent for streak operation must be limited. However, the magnitude of current for which space charge effects do not arise is insufficient to permit photographic recording of the streaks. This restriction is overcome by using a high gain image intensifier at the output of the tube. Even then, with a gain of 10^5 - 10^6, the dynamic range has been measured to be only about 3 (4.16) to 30 (4.17) for 2 ps pulses.

A new experiment to investigate the causes which limit the value of the streak camera's dynamic range to $\sim$10 when operating in the picosecond region is discussed in the remainder of this chapter.

4.7 The Dynamic Range of Four Image Converter Tubes in Nanosecond and Subnanosecond Photography

4.7.1 Details of the Four Image Converter Tubes

The characteristics of the four tubes used in this investigation are summarised in Table 4.1. Although they all employ electrostatic focussing, they possess different electron optical configurations, so that at equal anode potential, each tube has a different field near the photocathode. Thus, it is possible to distinguish between the effect caused by space charge due to the electric field near the

TABLE 4.1 - Details of the image converter tubes.

		Tube 1	Tube 2	Tube 3	Tube 4
Operating voltage	(V)	8 kV	8 kV	11.5 kV	6.5 kV
Magnification	(β)	0.9	0.9	2.6	0.33
Phosphor efficiency	(η)	0.1	0.1	0.1	0.1
Collection efficiency	(Ω)	0.015	0.015	0.7	0.7
Photon energy density on film in J cm^{-2}	(α)	$3x10^{-10}$	$3x10^{-10}$	$3x10^{-10}$	$3x10^{-10}$
Photocathode substrate resistance in $\Omega\ \square^{-1}$	(R)	100	100	100	1000
Electric field near photocathode in V cm^{-1}	(E)	2000	3500	400	200
Type of photocathode		S-20	S-1	S-20	CsTe
Spatial resolution (with 3 ns N_2 laser pulse)		10 lp mm^{-1}	10 lp mm^{-1}	10 lp mm^{-1}	10 lp mm^{-1}

photocathode and that at the cross-over region. Two of the tubes are fitted with S-20 photocathodes while the other two have an S-1 and a caesium telluride (CsTe) photocathode respectively.

4.7.2 Experimental Details

Fig. 4.2 shows the schematic of the experimental layout. A nitrogen laser pulse (λ = 3371 Å, FWHM = 3 ns) was used to illuminate uniformly a resolution chart, which was imaged optically on to the photocathode of the tube under test. The resolution chart consisted of a piece of veroboard which was masked to provide a pattern of two lines of equispaced holes. To minimise the effects due to non-linearities across the photocathode surface, the area illuminated by the laser was kept small. Hence, the input optics to the tubes were arranged such that the diameters of the illuminated dots on the photocathodes were approximately 0.6 mm in each case. Although this was a very coarse resolution test, it was sufficient for the purposes of the observations.

Image recordings were taken on film for each tube. The phosphor screen output windows of tubes 1 and 2 were optically coupled to the film by an f/2 relay lens with 1:1 magnification. Tubes 3 and 4 had fibre optic outputs which were in direct contact with the film. The films were all developed in Universal solution for 4 minutes at 20°C. It was found necessary to use films of different recording speeds (see Table 4.2) to cover the range of the four tubes.

In each case the corresponding voltage across the capacitor in the current monitor circuit (shown in Fig. 4.3) was recorded on a Tektronix 568 storage oscilloscope. A range of data was obtained by varying the intensity of the laser pulse with suitable density filters. A large number of recordings was taken to average out any errors due to fluctuations, both in amplitude and spatial pattern, of the laser beam.

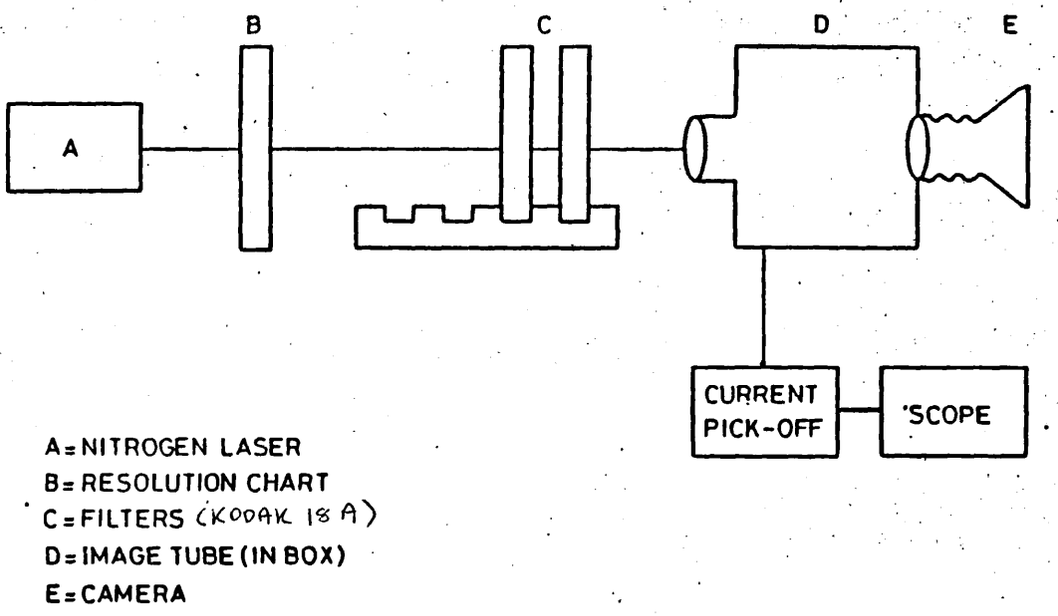

FIG. 4.2 - Experimental layout to investigate the dynamic range of four image tubes.

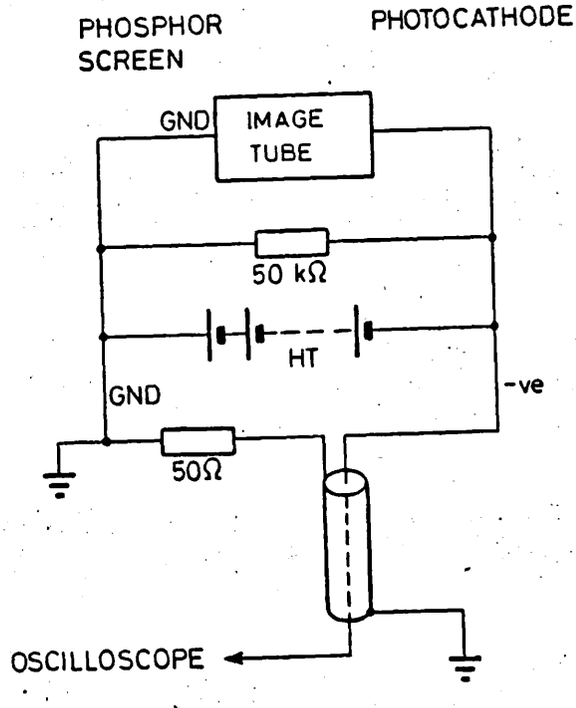

FIG. 4.3 - Current pick-off circuit.

4.7.3 Results

Series of photographs showing the dynamic range behaviour for each of the four tubes are given in Figs. 4.4 - 4.7. The photocathode substrate resistance of tube 4 was too high and non-uniform in the centre, hence the image was focussed onto an area near the outer edge of the photocathode. This caused the oblong appearance of the circular apertures in Fig. 4.7. All the tubes showed serious image distortion and collapse of the image towards the centre as the photocurrent densities were increased.

The corresponding values of photocathode current densities were calculated by means of the following formula:

$$I = \frac{i}{a} = \frac{Q}{at} = \frac{CV}{at} \quad \text{mA cm}^{-2} \qquad \text{IV - 14}$$

where I = photocathode current density

i = photocurrent

a = illuminated cathode area

C = capacitance of circuit = 180 pF

V = measured voltage

t = FWHM of N_2 laser pulse = 3 ns

The minimum and maximum values of the current densities were estimated from the photographs for each tube: the minimum current density was that for which an image just detectable above the fog level of the film was obtained and the maximum current density was that for which image distortion just set in. Defining the dynamic range as the region given by $I_{min} \rightarrow I_{sat}$, the value for each tube was calculated. These are shown in Table 4.2, normalised for Kodak 2475 films and an operating voltage of 8 kV.

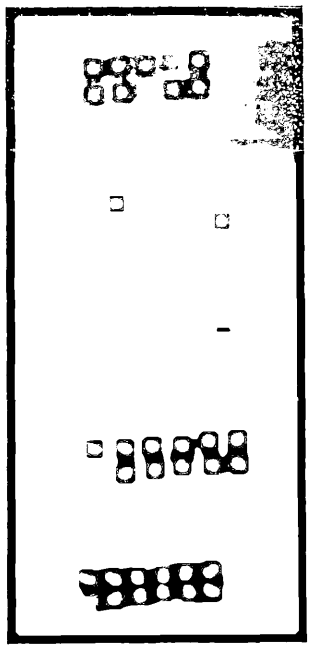

Photocurrent densities are:

a) 28 mA cm^{-2}

b) 64 mA cm^{-2}

c) 110 mA cm^{-2}

d) 200 mA cm^{-2}

e) 240 mA cm^{-2}

FIG. 4.4 - Photographs taken on Kodak 2475 film for tube 1.

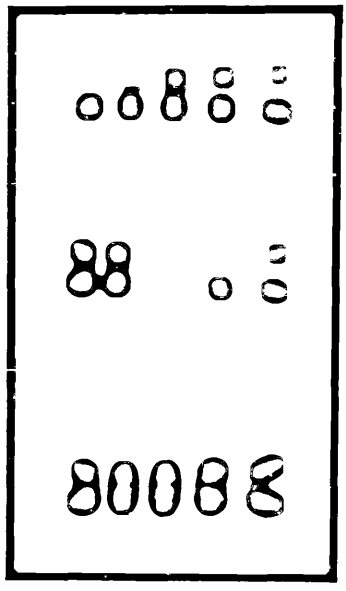

Photocurrent densities are:

a) 100 mA cm^{-2}

b) 160 mA cm^{-2}

c) 380 mA cm^{-2}

FIG. 4.5 - Photographs taken on Kodak FP4 film for tube 2.

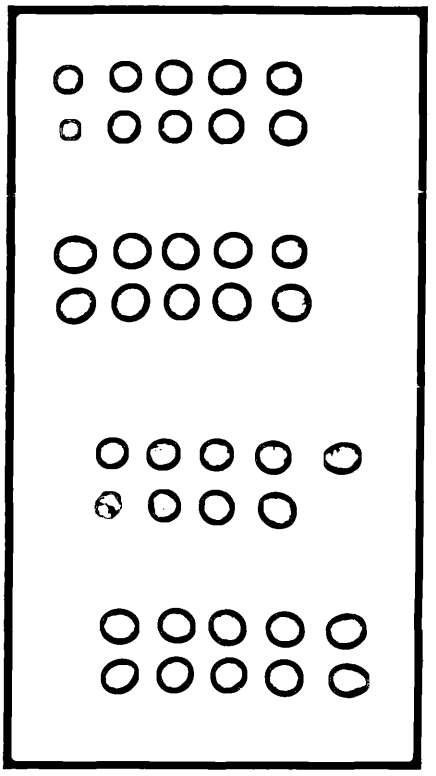

Photocurrent densities are:

a) 0.8 mA cm^{-2}

b) 3.2 mA cm^{-2}

c) 9 mA cm^{-2}

d) 13 mA cm^{-2}

FIG. 4.6 - Photographs taken on Ilford HP4 film for tube 3.

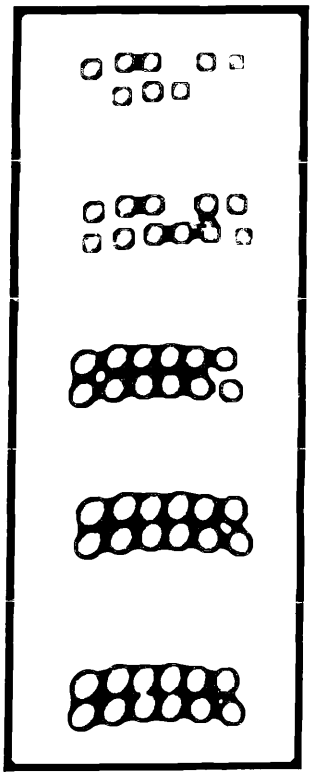

Photocurrent densities are:

a) 0.3 mA cm^{-2}

b) 0.8 mA cm^{-2}

c) 1.2 mA cm^{-2}

d) 2.5 mA cm^{-2}

e) 4 mA cm^{-2}

FIG. 4.7 - Photographs taken on Kodak Pan F film for tube 4.

TABLE 4.2 - Results

	Tube 1	Tube 2	Tube 3	Tube 4
Film	Kodak 2475	Kodak FP4	Ilford HP4	Kodak Pan F
Maximum current densities in mA cm^{-2} (I_{sat})	40	100	3.5	1.2
Minimum current densities in mA cm^{-2} (I_{min})	5	11	0.5	0.2
Theoretical ratios for I_{sat} from $E^{3/2}$ law	32	73	3	1
Experimental ratios for I_{sat}	33	83	3	1
Dynamic range (normalised for Kodak 2475 film and 8 kV)	8	30	12	64

4.7.4 Discussion

Although this is a simple experiment without the benefit of picosecond resolution or streak facilities for the image tubes, it can be used for a qualitative evaluation of the factors discussed in Section 4.6.

The first, photocathode resistance does not seem to be too important, as, although three of the tubes i.e. tubes 1, 2 and 3 have the same value of substrate resistance (approximately 100 $\Omega\,\square^{-2}$) they have different dynamic ranges. Also, tube 4 has both the highest substrate resistance (around 1000 $\Omega\ \square^{-2}$) and the greatest dynamic range.

High values for the electric field near the surface of the photocathode means that the liberated photoelectrons have a greater velocity, so that image distortion due to space charge effects take place at higher current densities. This is experimentally verified by the results of tubes 1 and 2. The only difference between the two tubes is that tube 2 has a higher electric field near the photocathode, but tube 2 has a maximum current density of 100 mA cm^{-2} compared with only 40 mA cm^{-2} for tube 1.

Space charge at the cross-over region is widely held to be the chief cause of image distortion. However, comparisons of the results for tubes 1 and 2, which have the same anode voltage, show a factor of greater than 2 difference for the maximum current densities.

So, the results suggest that space charge near the photocathode is more important than space charge at the cross-over region in limiting the dynamic range of image converter tubes. If the Child-Langmuir three halves ($E^{3/2}$) power law is applied to obtain the theoretical ratio of the maximum current densities from the values of the electric fields near the photocathodes there is good agreement with the experimental values as shown in Table 4.2.

Another interesting experimental result is the discovery that tube 4 has the greatest dynamic range. The reason for this may be because it

has the smallest magnification for its electron optics.

Consider the following formula derived by Schelev (4.14) for the minimum photocurrent required to produce a recording on photographic film:

$$I \gtrsim \frac{\alpha \beta^2 e a}{\gamma \tau \kappa \omega_{os}} \qquad \text{IV - 15}$$

where α = total energy required to produce required density

β = magnification factor of entire system

e = electron charge

a = illuminated photocathode area

γ = number of photons per photoelectron

τ = temporal resolution

κ = overall gain of system

ω_{os} = mean photon energy emitted by phosphor of tube.

This shows that the current density is strongly dependent on the magnification as I is proportional to β^2. At the moment most streak cameras use electron optics with values of β typically around 2 - 3 e.g. the Photochron II tube, giving I = 30 mA cm^{-2} for time resolutions of 10 ps (4.18). The same analysis shows that if β is made less than unity, the current density would drop e.g. β = 0.33 with an operating voltage of 30 kV gives I = 0.5 mA cm^{-2}. Hence, it should be possible to build a single stage image converter camera system for picosecond operation.

4.8 Possible Factors for Pulse Broadening Effects

The results obtained here are in agreement with those of Kalibjian (4.19) and Hull and Freeman (4.20) i.e. space charge at the cross-over region is not significant in pulse broadening effects. Both these groups were able to make tests involving streak cameras and picosecond pulses (10 - 30 ps). The same test method of masking the entrance slit of the

streak camera was used in both studies. No changes in dynamic range compared with values obtained using the full slit length were recorded.

However, the cause of the pulse broadening effects is still unknown. Kalibjian has suggested that space charge between the cathode and the grid is responsible, while Hull and Freeman think space charge between the grid and the phosphor is a more significant factor. Perhaps, the most novel solution has been suggested by Majumdar (4.18) - space charge effects inside the photocathode itself!

He has proposed two possible scenarios: the first suggest that the photoelectrons must stay longer in the photocathode before being emitted. However, in a solid excited electrons do not have very long lifetimes, so for this hypothesis to be correct, photoelectrons must somehow have longer lifetimes in the photocathode and the mechanisms for such a process are as yet unclear.

His second hypothesis is more plausible: the time dilation of the pulses is due to effects in the surface layer of the photocathode. As the vacant spaces in the surface layer must be filled up before excited electrons can be emitted, bottlenecking can occur in the surface layer.

Obviously, clarification of the reasons contributing to pulse broadening must await the results of further experiments and analysis.

CHAPTER 5

Diagnostics for High Speed Spectroscopy

5.1 Introduction

The laser pulse duration in these experiments is 100 ps - 1.8 ns. Hence, picosecond time resolution is required to observe interactions in the plasma during the laser pulse. Of particular interest in this thesis is the coupling of the light energy to the target and the study of the interactions described in Chapter 3 e.g. Brillouin scattering, resonance absorption, the two plasmon decay, etc.

The presence of these and other instabilities in the plasma can be inferred from the appearance in the scattered light spectrum of the frequencies ω_o , $2\omega_o$ and $3\omega_o/2$. For example, light backscattered with a small red shift from the fundamental frequency, ω_o , is characteristic of the Brillouin scattering instability. Also the observation of harmonic emission at $2\omega_o$ (Chapter 7) and $3\omega_o/2$ (Chapter 8) imply the generation of ω_o plasmons, at the critical density surface, and $\omega_o/2$ plasmons, at the quarter critical density surface, respectively. The former can be ascribed to either resonance absorption or the parametric decay instability and the latter to either stimulated Raman scattering or the two plasmon decay instability.

Hence, a suitable diagnostic must incorporate both high temporal and spectral resolution. Also, as the conversion efficiency of the $2\omega_o$ and $3\omega_o/2$ harmonics is expected to only around 10^{-5} - 10^{-7} (5.1) of the incident laser energy (15 - 100J) an instrument with high gain is required for photographic recording. A dynamic range of at least 10 is also necessary to observe any structure that might be present during the evolution of the spectra.

In Chapter 4, the image converter streak camera was demonstrated to possess a dynamic range of about 10 for picosecond time resolution and

when used with an image intensifier, a gain of $\sim 10^6$. Thus, the streak camera can be coupled to the dispersed output of a spectrograph to provide the main diagnostic for high speed spectroscopy.

Two commercial streak cameras - the Electrophotonics Ltd (EPL) and Hadland Photonics Ltd Imacon 675 - and three grating spectrographs - Spex and Monospek makes - are provided by the SERC Laser Facility. The description and calibration of these instruments are discussed in the following sections. Setting up of the diagnostics for high speed spectroscopy is then outlined.

5.2 The Streak Cameras

Fig. 5.1 shows the schematic layout of the EPL and Imacon 675 streak cameras. It can be seen that they differ primarily in their intensifiers, possessing an electromagnetically focussed intensifier (EMI Type 9912) and a channel plate intensifier (Mullard 50/40) respectively. Although not shown in the diagrams, they also differ in their electronic circuits: the ramp voltage is supplied by a krytron (KN 22) and a hard ceramic valve respectively. The ceramic valve can be operated with a jitter of only ± 100 ps compared with over ± 350 ps for the krytron, which simplified the synchronisation for the Imacon 675 over the EPL camera.

The photocathode may be either S-1 (Ag-O-Cs) or S-20((Cs)Na_2K Sb) with spectral responses as shown in Fig. 5.2. For monitoring the incident laser pulse (λ = 1.06 μm) and the Brillouin scattering experiment the S-1 tube was used for its infra-red response. However, the S-20 tube was preferred for the harmonic emission studies because of its higher sensitivity in the visible range.

5.3 The Calibration of the Streak Cameras

The following streak camera calibrations were performed:

i) spatial resolution

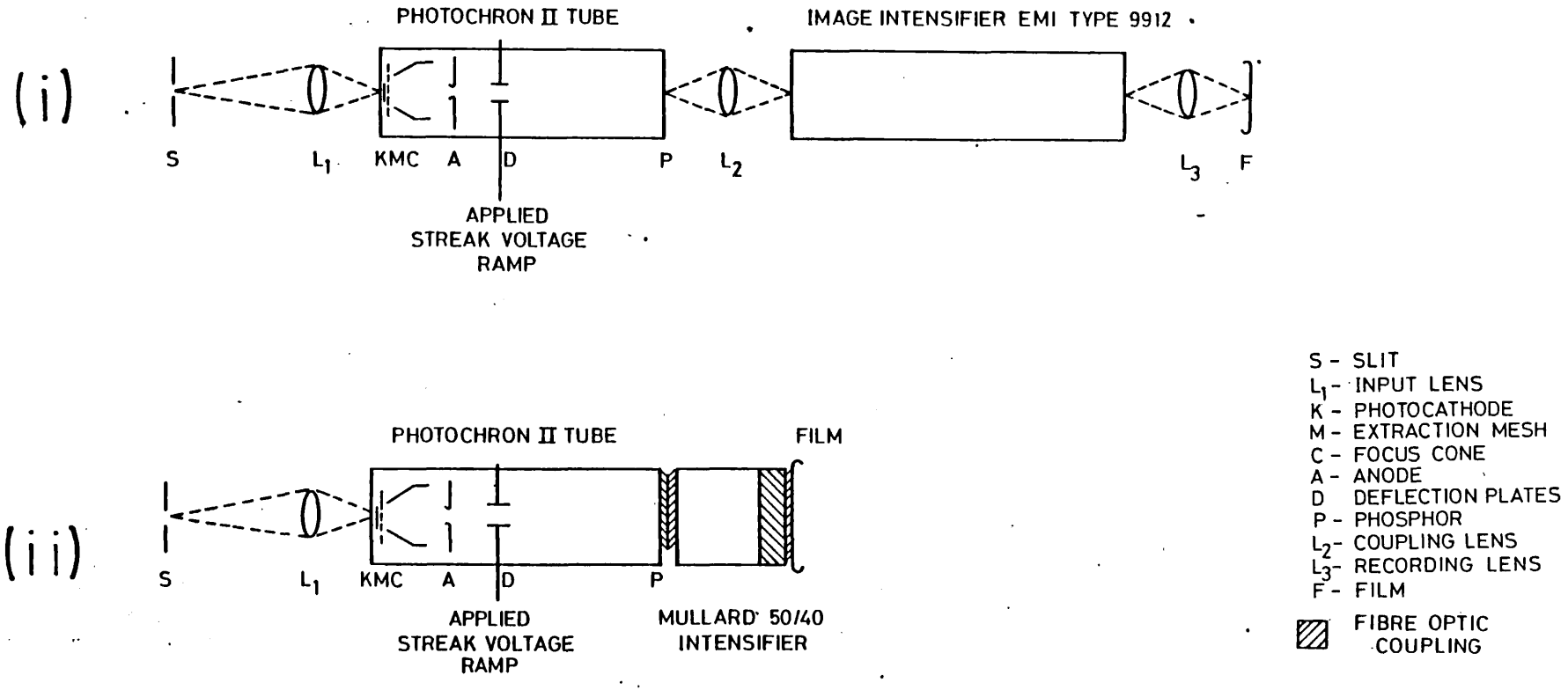

FIG. 5.1 - Schematic diagram of the streak camera systems
i) Electrophotonics Ltd. (EPL) ii) Imacon 675

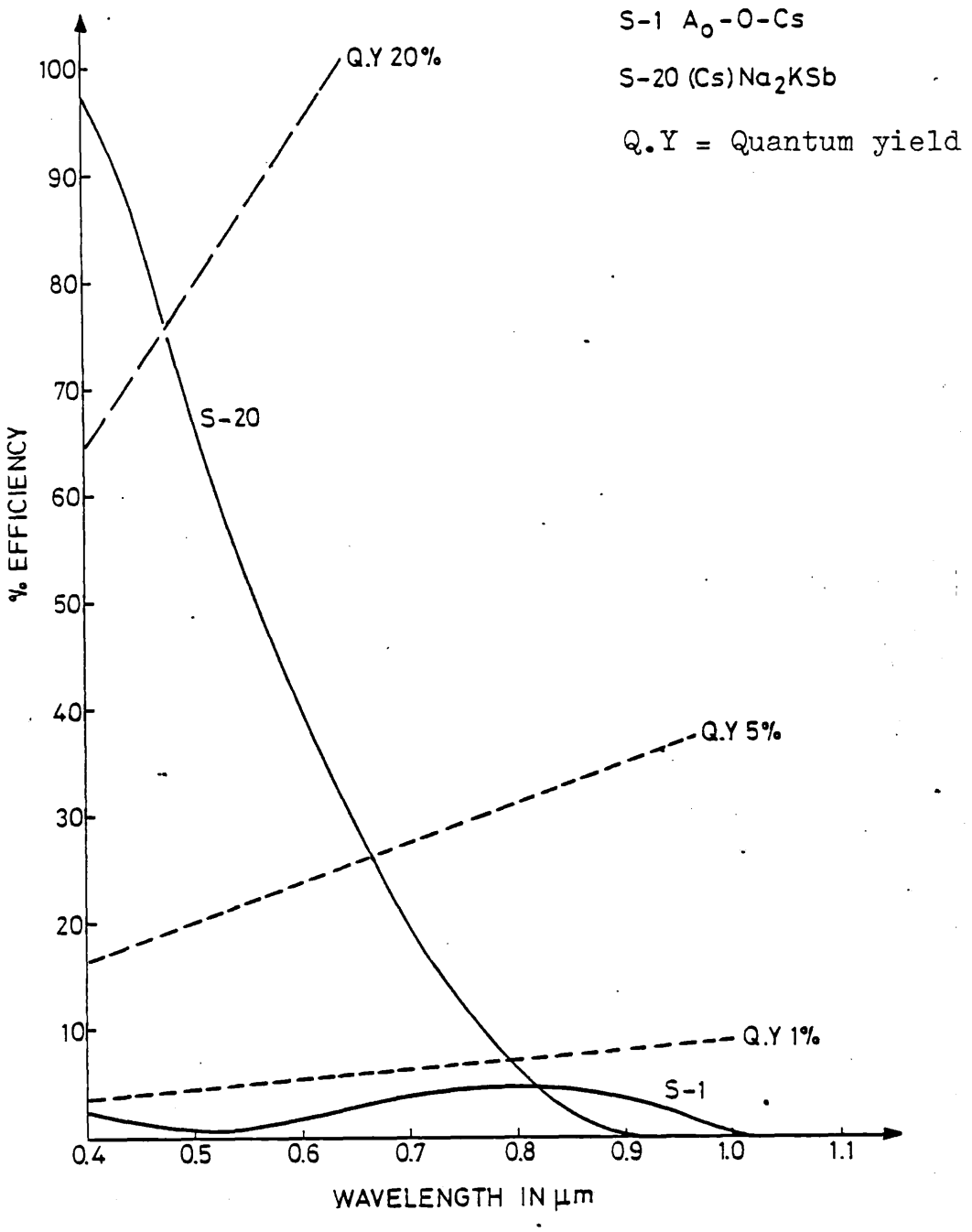

FIG. 5.2 - Spectral response curves for S-1 and S-20 photocathodes. (Reproduced from the RCA Photomultiplier Manual, Technical Series, PT-61, 1970.)

ii) sweep speed and linearity

iii) gamma curves with Kodak 2485 film

iv) dynamic range

These measurements require a short pulse illumination source which is provided by the output of a mode locked dye laser (EPL Model 33). The lasing medium is Rhodamine 6G (R6G) and the mode locking dye is 3 3' diethyloxadicarbocyanine iodide (DODCI). The dye laser wavelength is between 5700 - 6100 Å depending on the charging voltage and dye concentration conditions. Each mode locked pulsewidth is $\sim$ 10 - 20 ps and the pulse separation in the mode locked train is $\sim$ 4 ns.

The interpulse spacing is too long to calibrate the streak rates on the faster sweep speeds (i.e.1 ns cm^{-1} to 300 ps cm^{-1}), hence an air gap etalon is used to produce a train of pulses with fixed separation and decreasing amplitude as shown in Fig. 5.4 (ii). The reflectivities of the etalon mirrors were measured with a He -Ne laser and a power meter to be about 70% (representing an attenuation factor of 2) and the separation of the mirrors was measured accurately to within 5 ps.

Additionally, a Pockels cell may be used to switch out a single mode locked pulse to avoid exposing the photocathode to a long chain of pulses.

5.3.i) Spatial Resolution Measurements

Both the static (focus mode operation) and dynamic (streak mode operation) spatial resolutions were measured. The latter is degraded compared with the former since for pulsed operation the high intensity effects discussed in Chapter 4 are important. For both measurements the standard U.S. Air Force resolution test pattern is used, consisting of groups of vertical and horizontal equispaced bars diminishing in width towards the centre of the chart. Fig. 5.3 i) shows the image produced

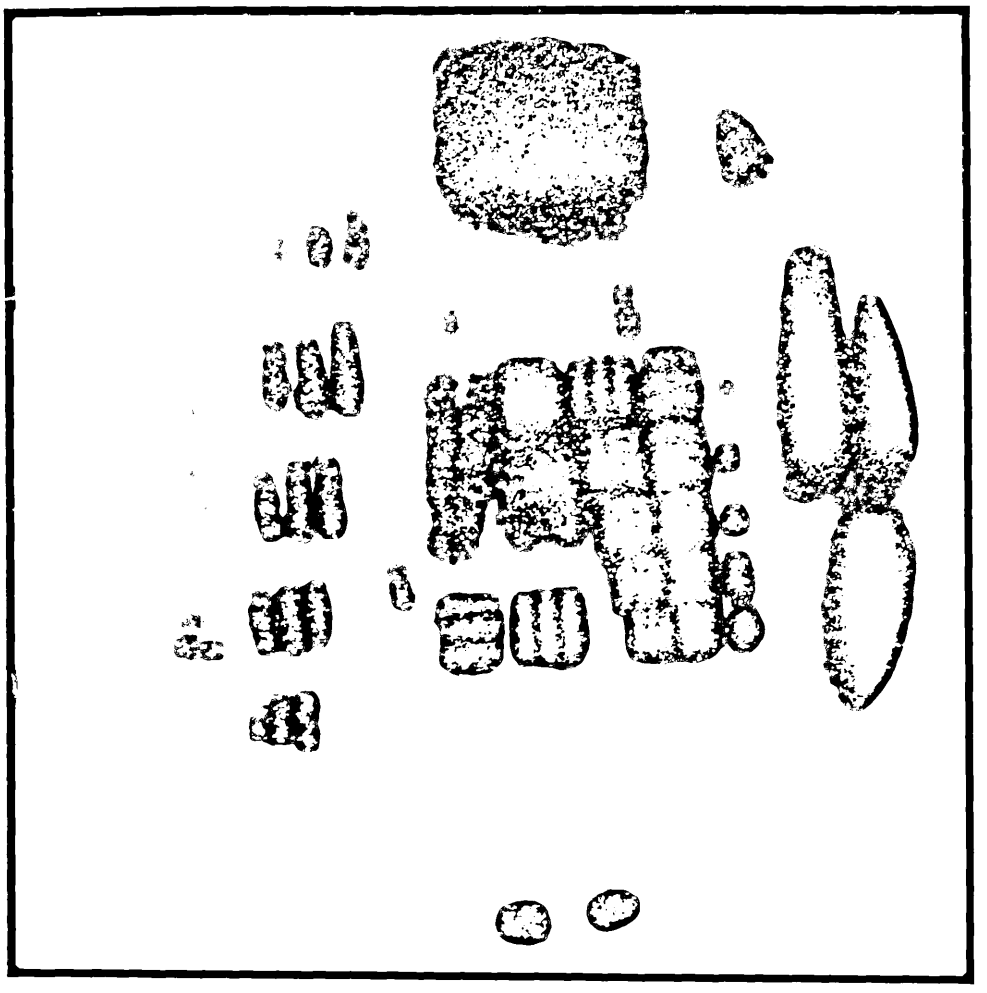

FIG. 5.3 i) - Focus mode picture of the Air Force test chart taken with Imacon S-20 camera on Kodak 2485 film.

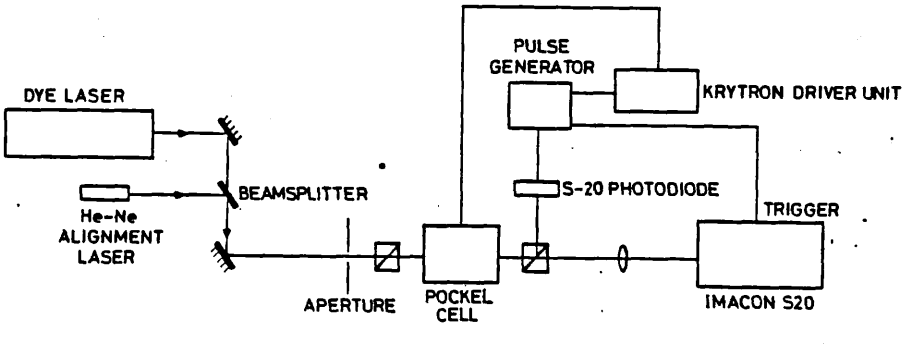

FIG. 5.3 ii) - Experimental arrangement for switching out a single modelocked pulse from a R6G dye laser for measuring the dynamic spatial resolution of the Imacon S-20 camera.

at the output phosphor of the intensifier on the Imacon S-20 camera when the chart is uniformly illuminated by the diffuse light from a microscope lamp.

The whole area of the photocathode is tested as the entrance slit has been removed. The image is recorded on Kodak 2485 film, developed in D 19 solution for 5 minutes at 30°C to give an ASA rating of 3000. The spatial resolution at the phosphor is $\sim$ 30 line pairs per mm (1p mm^{-1}) where a line pair is a dark and light bar together.

To measure the dynamic spatial resolution the photocathode current must be of the order that flows during streaking. Hence, a single switched out pulse from the mode locked R6G dye laser is used to illuminate the test chart as shown in Fig. 5.3 ii). As the image tube is conducting only for the duration of this pulse, the photocurrent is comparable to that for streaking and the whole of the photocathode is still visible. The result is recorded on Kodak 2485 film, developed as before, giving a dynamic spatial resolution for the Imacon S-20 of 10 1p mm^{-1}.

5.3 ii) Sweep Speeds and Linearity

For these measurements the streak camera is operated in the streak mode and the experimental arrangement shown in Fig. 5.4 i) is used. To measure a wide range of sweep speeds, etalons of two different spacings had to be used and their dimensions are summarised in Fig. 5.4 ii). Fig. 5.4 iii) shows an example of the streak obtained of the etalon pulse train on Kodak 2485 film with one of the mode locked pulses.

The sweep rate can then be calculated from the known separation of the etalon mirrors. The curves for three different sweep rates for the Imacon 675 camera are shown in Fig. 5.5 (the fit is the best fit by eye). The non-linearity in the curves is mostly due to the bad pincushion distortion of the channel plate intensifier.

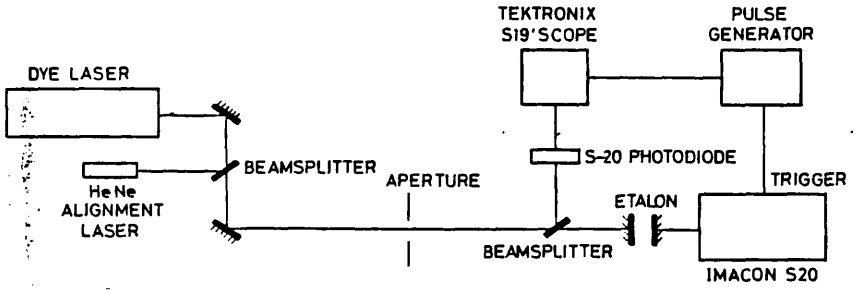

(i)

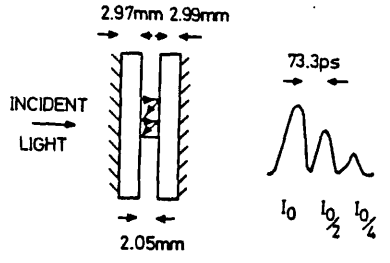

(ii)

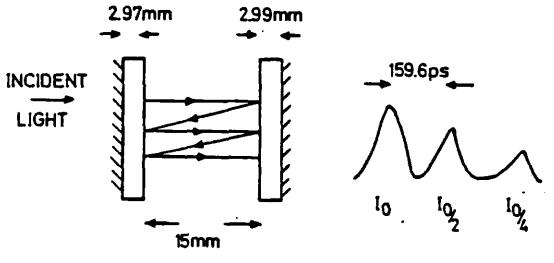

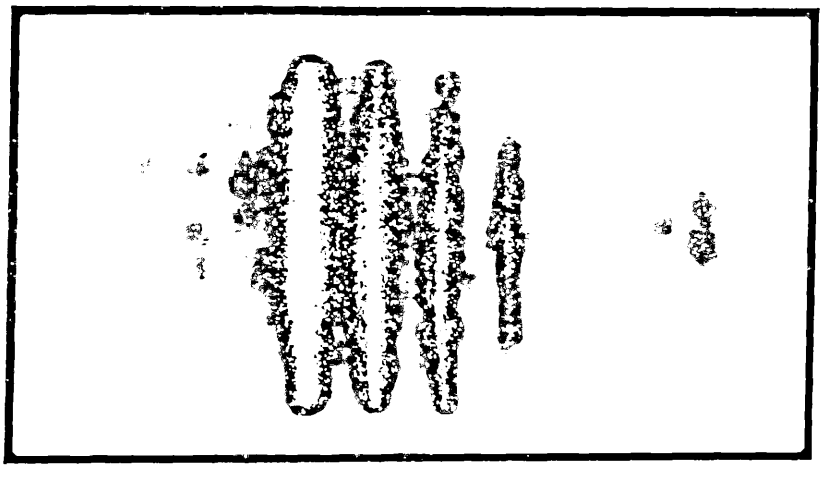

(iii)

FIG. 5.4 - Streak camera calibrations using a modelocked dye laser and etalon. i) Experimental arrangement. ii) Dimensions of etalons. iii) Imacon S-20 streak record: nominal sweep speed = 600 ps cm^{-1}; pulse separation = 160 ps

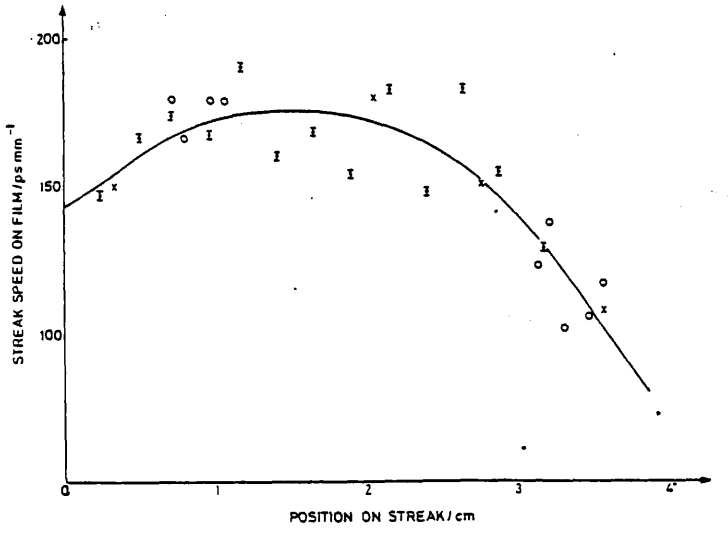

(i)

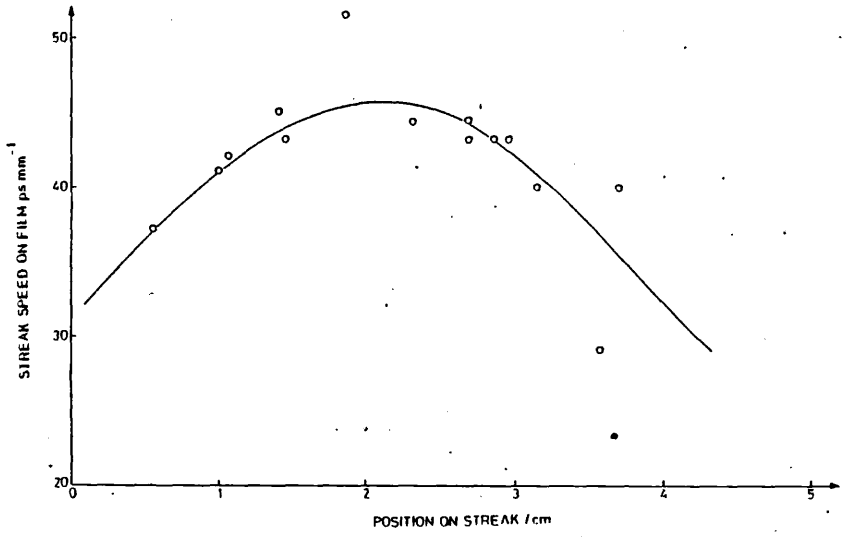

(ii)

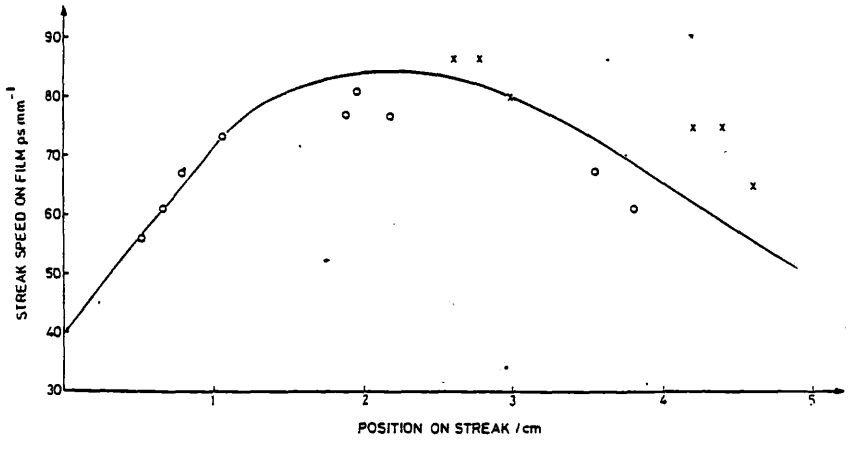

(iii)

FIG. 5.5 - Streak rate calibration curves for the Imacon 675
i) Nominal sweep speed = 1 ns cm^{-1}.
ii) Nominal sweep speed = 600 ps cm^{-1}.
iii) Nominal sweep speed = 300 ps cm^{-1}.

5.3 iii) Gamma Curves

The linearity of the streak cameras' intensity response can be measured from the same streak pictures since the ratio of the intensity of successive etalon pulses is fixed at an attenuation of 2. Firstly, the gamma curve of the Kodak 2485 film only is found by exposing a calibrated step wedge (step attenuation of 2) directly onto a piece of film. This is the top curve marked by X's in both Fig. 5.6 i) and Fig. 5.6 ii). The curves marked by O's represent the experimental values derived from the etalon streak pictures for the streak camera, intensifier and film combinations for the two commercial systems. It can be seen that at high intensities the response of both streak cameras is reduced due to non-linearities in the systems.

5.3 iv) Dynamic Range Measurements

Overexposure of the photocathode results in pulse broadening (as discussed in Chapter 4) hence the useful range of intensities which can be incident on the streak cameras must be found.

The γ curves are used to determine the width of each pulse in the etalon train recordings at its half maximum intensity point (FWHM). The ratio of the measured pulse duration to the mean (actual) pulse duration at low intensities, t_p' / t_p is plotted against log intensity (in arbitary units) as shown in Fig. 5.7. Defining the upper limit as the point where the pulse broadens by 20%, the dynamic range of the EPL S-20 = 10 and the Imacon S-20 = 16.

5.4 Streak Camera Synchronisation

The useful streak length is 4.5 cm and this defines the temporal window of the streak camera, e.g. temporal window = 4.5 ns for sweep speed = 1ns cm^{-1}. For the fastest sweep speeds, this means the streak camera must be carefully synchronised with the main laser pulse to record the event. The camera is triggered by a photodiode which receives a

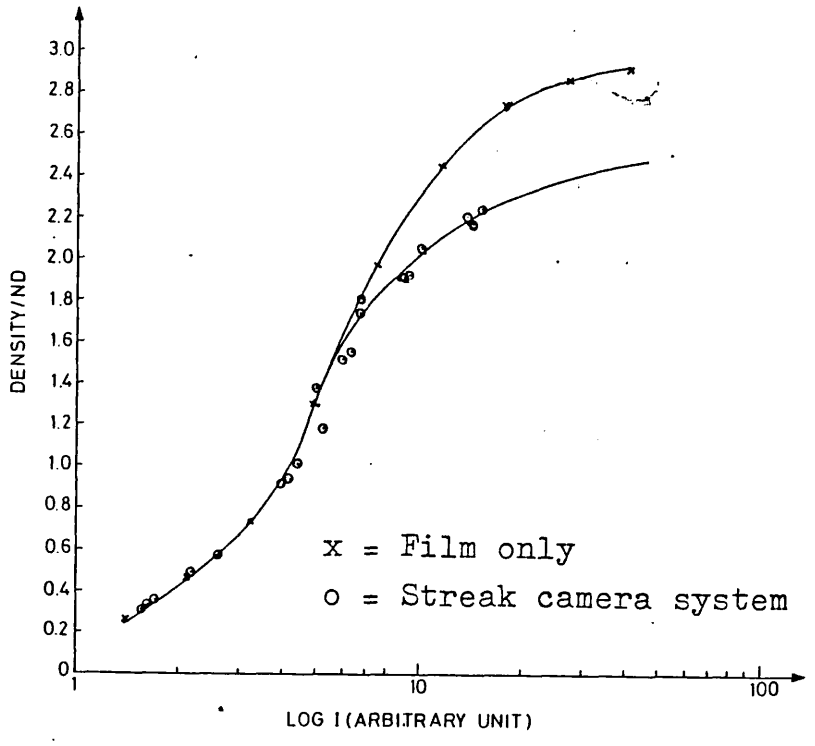

(i)

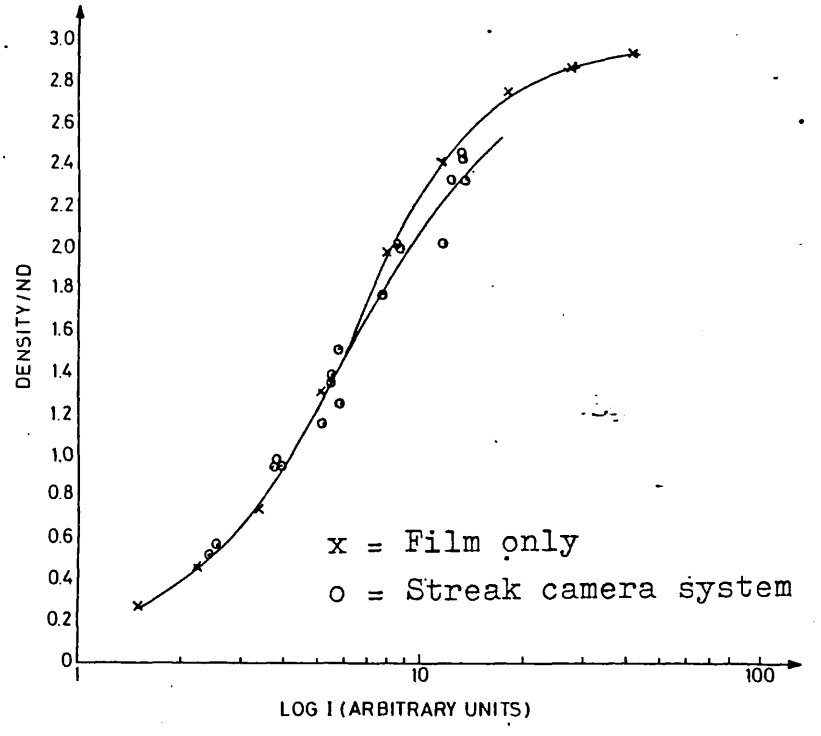

(ii)

FIG. 5.6 - Gamma curves for Kodak 2485 film and streak camera systems. i) EPL camera. ii) Imacon 675.

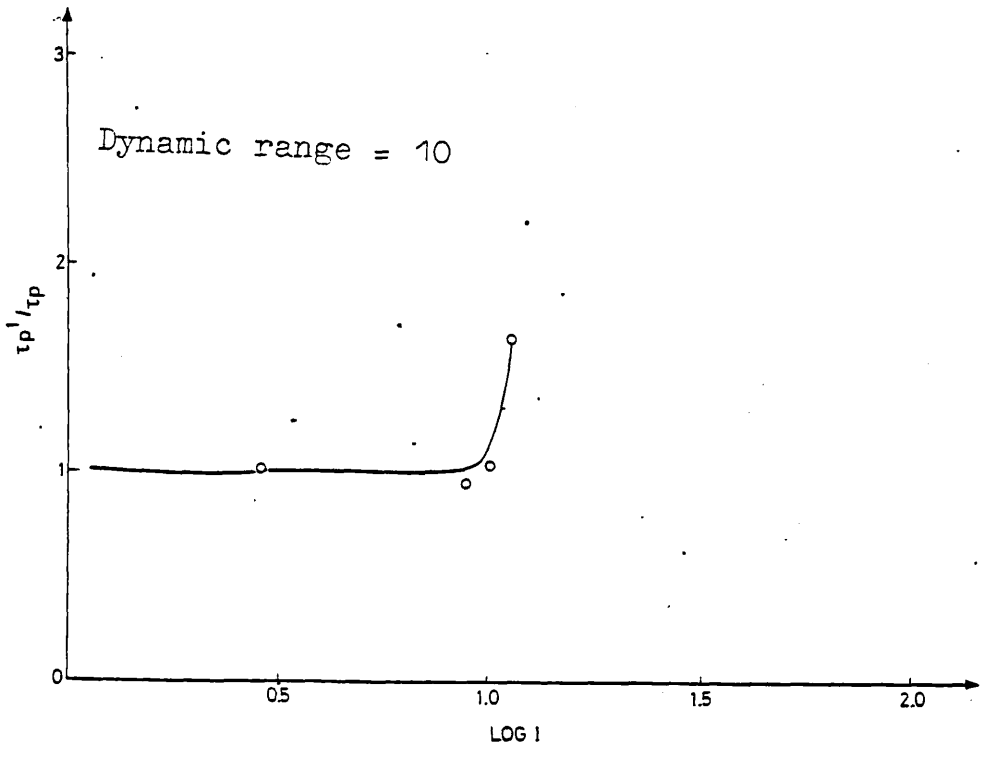

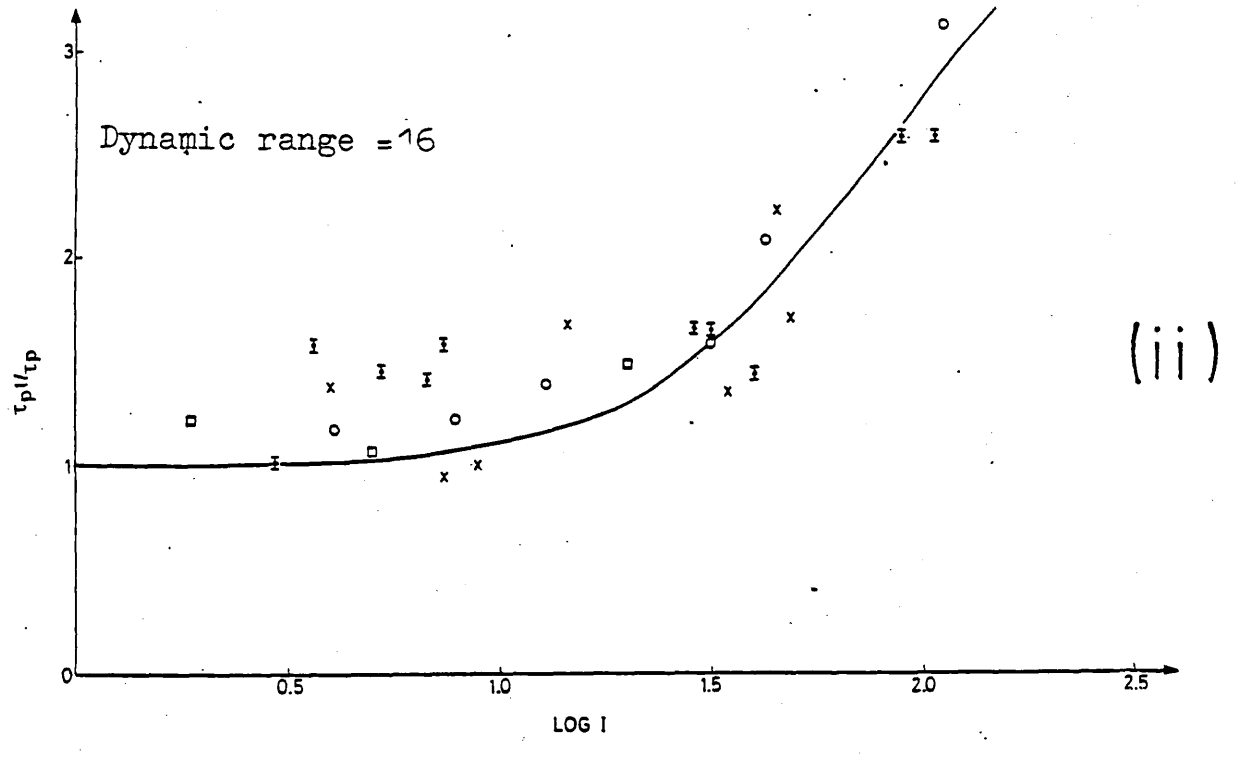

FIG. 5.7 - Dynamic range of streak camera systems recording on Kodak 2485 film. i) EPL camera. ii) Imacon 675.

portion of the light from early on in the amplifier chain. The cable delay from this photodiode to the streak camera is then adjusted until the camera is synchronised with the event.

5.5 Time-Resolved Spectroscopy

For time-resolved spectroscopy, the streak camera is coupled to the output of a spectrograph as shown in Fig. 5.8. The spectrum is dispersed along the streak camera slit, so the result is temporally resolved along the direction of the streak and spectrally resolved along the line of the slit.

The Brillouin scattering experiment (Chapter 6) used a Monospek spectrograph (f/10) and the $2\omega_o$ and $3\omega_o/2$ harmonic spectra were dispersed by two Spex spectrographs (both f/4). All these spectrographs are reflexion grating spectrographs of the Czerny-Turner design as shown in Fig. 5.9. The dispersions were measured by exposing the output of a mercury lamp through each spectrograph onto Type 55 polaroid film. These and the characteristics of each spectrograph are listed in Table 5.1.

Table 5.1 Spectrograph Characteristics

Spectrograph	Grating Ruling	Focal Length	Dispersion
Monospek	600 lines mm^{-1}	1 m	7 Å mm^{-1}
Spex A	1200 lines mm^{-1}	0.5 m	14 Å mm^{-1}
Spex B	600 lines mm^{-1}	0.5 m	12 Å mm^{-1}

For the harmonic emission observations, the incident laser pulseleng $\sim$ 100 ps, so high temporal resolution $\sim$ 10 - 20ps is required. However, in a grating spectrograph the optical pathlength of a light ray diffracte from a given groove differs, in first order, by one wavelength from the p of a ray diffracting from the adjacent groove. Hence, as more lines of t grating are illuminated the spread in time of the light pulse Δt is

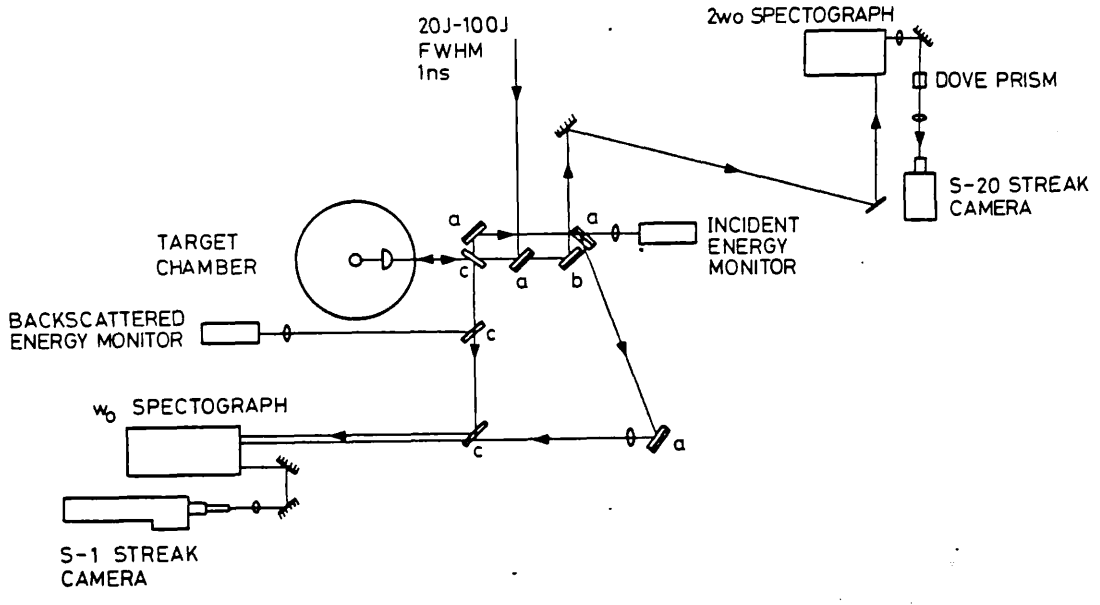

FIG. 5.8 - Experimental layout for high speed spectroscopy.

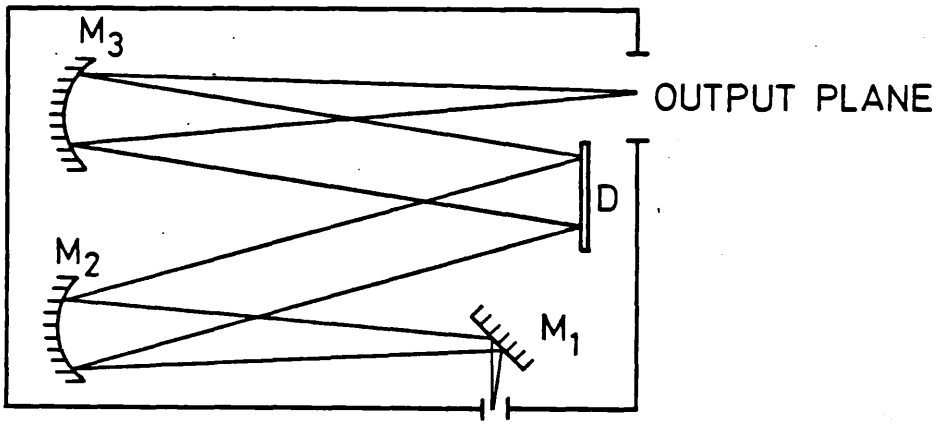

D = DIFFRACTION GRATING

M_1, M_2 AND M_3 = MIRRORS

FIG. 5.9 - Schematic diagram of Spex spectrograph.

given by;

$$\Delta t = \frac{\lambda^2}{c\Delta\lambda} \qquad V - 1$$

For picosecond time resolution the number of grooves illuminated in the grating must be restricted. This can be achieved by choosing a suitably large f-number for the aperture of the input optics to the spectrograph. However, if the grating is not fully illuminated the spectral resolution of the spectrograph is less than that predicted by the entrance slit width. So, there is a trade-off in the temporal and spectral resolutions and these are chosen in the following experiments to be near the limit $\Delta t \Delta\lambda \sim 1$.

5.6 Energy Monitors

For the Brillouin scattering experiment the incident and back-scattered energies near the fundamental frequency were measured by calorimeters employing silicon PIN photodiodes (type SGD 040A). These are sensitive over a spectral range of 0.35 μm to 1.13 μm (5.2). The calorimeters are calibrated against an absorbing glass disc calorimeter and the readings corrected for losses at the beamsplitter, chamber window and lens surfaces ($\sim$ 4% loss at each reflecting surface).

The irradiance incident on the target is calculated by means of the following formula:

$$\Phi_{inc} = \frac{E_{inc}\ (J)}{\tau(s)\ \pi\ r^2\ (cm^2)} \text{ Watts cm}^{-2} \qquad V - 2$$

where E_{inc} is the corrected value from the incident energy monitor; τ, the incident pulselength (FWHM) is measured from the S-1 streak recordings; and r, the focal spot radius - estimated from the x-ray pinhole camera

pictures. This figure represents an average irradiance over the surface of the target; non-uniformities in the illumination of the target may result in irradiances greater than the average figure by a factor of 3 in "hot spots".

5.7 Data Analysis

The raw data consists of information on Kodak 2485 film which lie in the ($\tau\lambda$) plane. This is analysed using a Joyce Loebl microdensitometer. For greater ease of analysis, the SERC facility also provides a microdensitometer which has been modified so it can be run by instructions from the GEC 4080 computer. This enables 2 - D scans of the data to be automatically taken and then plotted to produce a map of constant density contours. Programs are provided to produce sections through the map along either the τ or λ directions. Examples of data treated in this manner are shown in Fig. 5.10.

Other advantages of using a computerised system include facilities to correct for the film characteristics and to perform integrations in time and wavelength which can be normalised to the energy monitor readings. These are used in particular to analyse the mode beating shot discussed in Chapter 6, section 6.

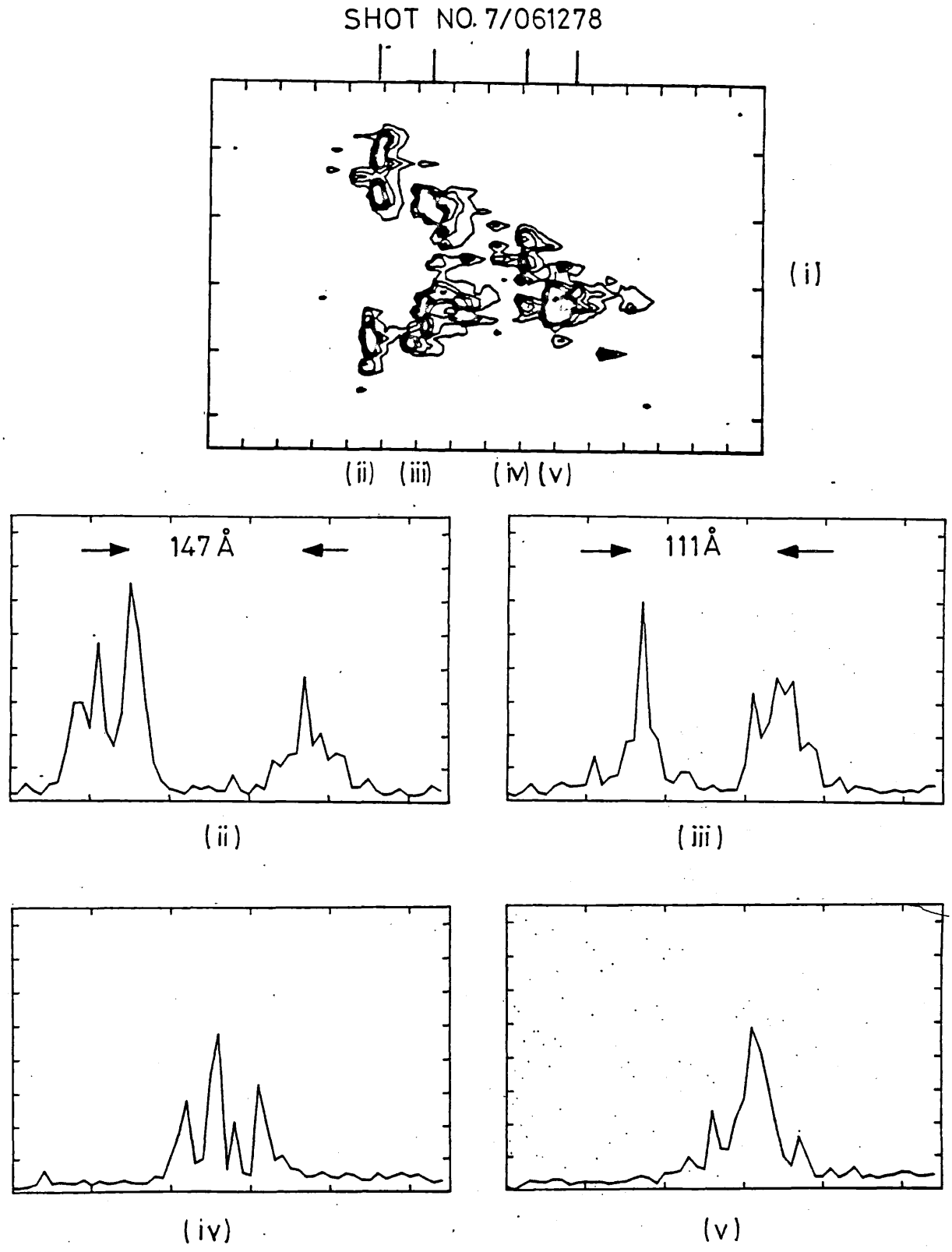

FIG. 5.10 - 2 - D microdensitometer scan of time-resolved 3/2 w_o harmonic spectrum. i) Isodensity contour map. ii) - v) Vertical sections as indicated.

CHAPTER 6

Time-Resolved Studies of Brillouin Backscatter Emission from Laser Irradiated Spherical Targets

6.1 Introduction

The stimulated Brillouin scattering (SBS) instability, discussed in Chapter 3, may pose a serious light scattering problem in long, underdense plasmas. Experiments (6.1 - 6.3) have confirmed that SBS is present for plasma and laser parameters of interest to laser fusion. This experimental evidence is reviewed in the next section.

In this Chapter, an experiment is presented in which a long (1.8 ns) Nd laser pulse was used to irradiate spherical targets in a range of materials and sizes. The light backscattered through the main focussing lens was simultaneously spectrally and temporally resolved, yielding evidence of SBS. There was also evidence of the second harmonic ($2\omega_o$) emission which will be discussed in Chapter 7.

6.2 Review of Experimental Evidence for SBS

Theoretical predictions show that for long pulse experiments, absorption will be reduced as light is reflected before it can reach the critical density surface by SBS. Experiments support these predictions. For example, Lawrence Livemore Laboratory report (6.1) that when plastic discs are irradiated by 1.06 μm light ($\Phi \sim 3 \times 10^{15}$ to 3×10^{16} W cm^{-2}) the absorption is reduced by a factor of 2 for pulse lengths of 200-400 ps compared with 80 ps. Measurements of the spectra of the reflected light show frequency shifts consistent with Brillouin scattering. Subsequent experiments with pulse lengths of the order of 1 ns (6.2) and high Z targets have also indicated appreciable Brillouin scattering.

In the experiments of Ref 6.2, an estimate of the coronal temperature

was made by a measurement of the Brillouin shift. The measured frequency shift also contains a Doppler shift, so to separate the two contributions, the target is used at both normal and 45° incidence to the laser beam. Then,

$$\left.\begin{aligned} \Delta\lambda(0^\circ) &= \Delta\lambda_B - \cos 0^\circ \, \Delta\lambda_D \\ \Delta\lambda(45^\circ) &= \Delta\lambda_B - \cos 45^\circ \, \Delta\lambda_D \end{aligned}\right\} \qquad \text{VI - 1}$$

can be solved (where the subscripts B and D refer to Brillouin and Doppler respectively) assuming the ablation velocity, electron temperature, mean ionisation state and critical density do not change significantly when the disc is tilted. Values of $T_e \sim 5$ keV for $\Phi = 3 \times 10^{14}$ W cm^{-2} and $T_e \sim 20$ keV for $\Phi = 3 \times 10^{15}$ W cm^{-2} were obtained.

A large underdense plasma can also be created by the use of a prepulse. Ripin et al (6.3) showed that the addition of a prepulse approximately 2 ns before a main pulse of 75 ps duration increases the backscatter from the main pulse on a plane plastic target. They also found that the reflected light rays retrace their paths which is a feature of Brillouin scattering.

Time resolved ω_o spectra have been obtained by Gorbunov et al (6.4) from plane polyethylene targets irradiated by Nd/glass laser pulses of 5 ns durations. For $\Phi \sim 3 \times 10^{12}$ W cm^{-2}, they observe a broadened line approximately 5 Å wide with a 2 Å red shift. For $\Phi > 3 \times 10^{13}$ W cm^{-2}, a blue wing is observed which broadens with increasing irradiance later on in the pulse. For $\Phi \sim 10^{14}$ W cm^{-2}, both blue and red wings appear simultaneously with oscillations of period $\sim$0.7 ns in intensity.

Gas jet targets have also been used for studies of Brillouin backscatter. Ng et al used a 35 ns CO_2 laser pulse on a hydrogen gas jet to simulate both underdense (6.5) and overdense (6.6) conditions.

Large levels ($\sim$ 30% with saturation at 60%) of backscatter are obtained with long (1 mm) scalelength plasmas, but only about 18-30% with short scalelength plasmas. Slater et al (6.7) also used a gas jet target (density gradient length $\sim$ 50 μm) for their short pulse (100 ps) Nd/glass laser experiment. Spectra of the backscattered emission display the characteristic red shift of Brillouin. This shift of $\sim$ 4 Å remains constant for a range of irradiances up to 2×10^{15} W cm^{-2} , but the backscattered energies increase to a saturation level of $\sim$ 40% for the maximum incident intensity. A periodic frequency structure is seen in the high intensity shots which might have been due to multiple Brillouin reflections.

6.3 Experimental Method

The experimental layout is shown in Fig. 6.1. The Nd/glass laser beam ($E_L \lesssim 100$ J FWHM $\sim$ 1.8 ns) was focussed onto the spherical targets by an aspheric doublet f/1 lens. The ω_o radiation backscattered through the main focussing lens was imaged onto the slit of a 1 m Monospek grating spectrograph and the dispersed output optically coupled onto an Electrophotonics Ltd (EPL) streak camera, fitted with an S-1 photocathode. A portion of the incident laser beam was suitably delayed and also directed onto the spectrograph, thus providing a simultaneous temporal and spectral reference as well as an incident pulse profile.

The streak camera was operated at a sweep speed of 2 ns cm^{-1} and an entrance slit width of $\sim$ 100 μm, giving a best temporal resolution of 20 ps. The entrance slit width of the spectrograph was 200 μm, and with a dispersion of 7 Å mm^{-1} in the output plane, this gives a spectral resolution of $\sim$ 1 Å. As discussed in Chapter 5, this imposed a restriction on the temporal resolution (equation V-1):

$$\Delta t = \frac{\lambda^2}{c\Delta\lambda} = 37 \text{ ps} \qquad \text{VI - 2}$$

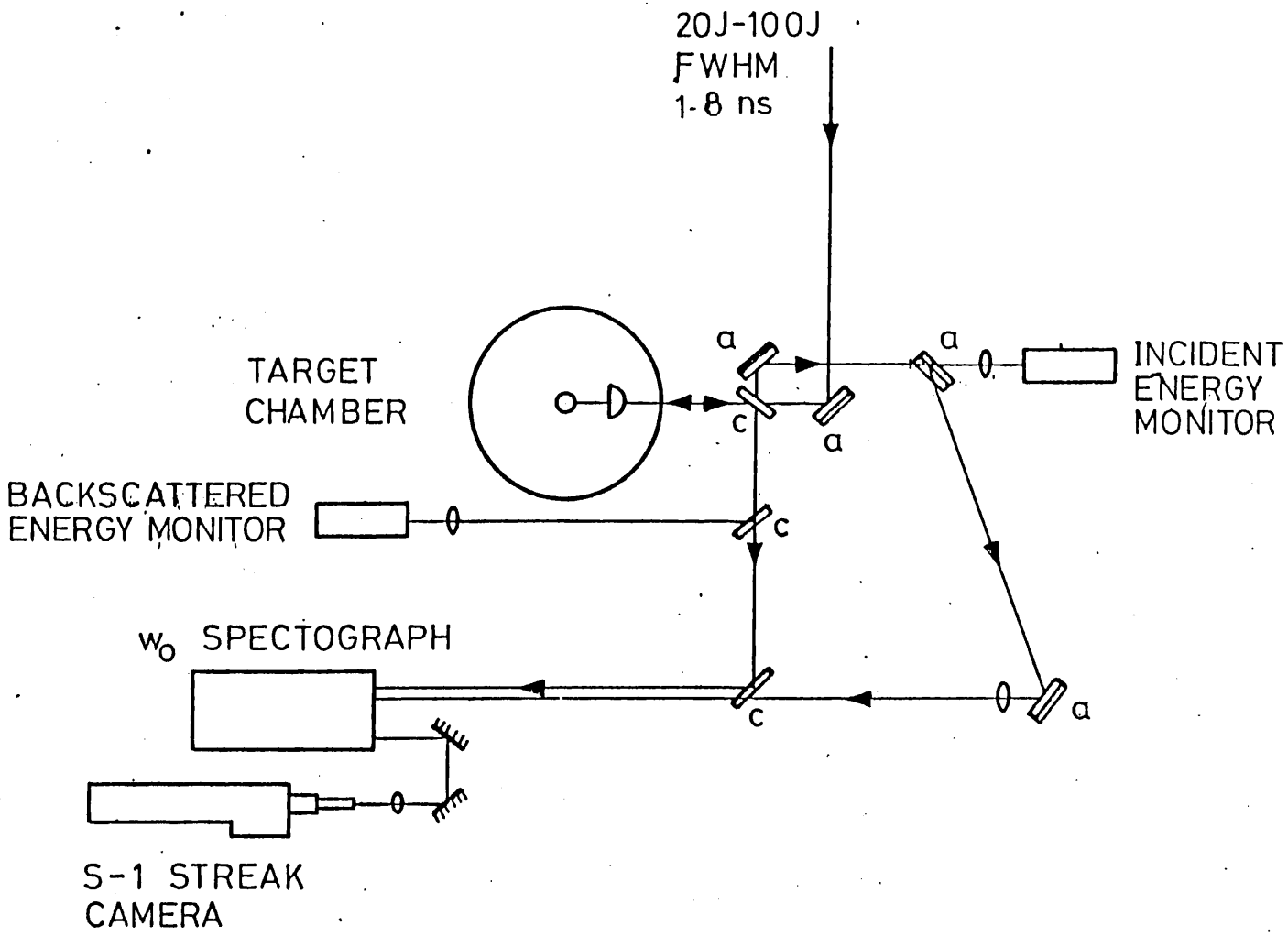

FIG. 6.1 - Experimental layout for temporally and spectrally resolved studies of Brillouin backscatter.

No further loss of spectral resolution was caused by the streak camera as the magnification from the spectrograph to the streak camera was x 2. Hence, the net spectral and temporal resolutions of the system were $\sim$ 1 Å and $\sim$ 40 ps respectively. The streak data were recorded on Kodak 2485 film develped at 30°C for 5 minutes.

The incident and backscattered energies at 1.06 μm were monitored by the two calorimeters as shown in Fig. 6.1.

The targets were microballoons and microspheres in two different size categories to investigate the effect of different sized underdense plasmas: "small" of 70 - 90 μm diameter and "large" of 210 - 250 μm diameter. The effect of different coronal temperatures on the size of the underdense plasma was also investigated by using a range of target material Z; from plastic to U^{238} in the small targets and from plastic to manganese - nickel alloy in the larger size.

The focussing of the laser beam by the f/1 lens was onto the centre of the spherical targets, so that all rays were close to normal incidence. On the small targets the irradiance for a beam energy of 100 J was 4×10^{15} W cm^{-2} and on the larger targets, the corresponding irradiance was 5.2×10^{14} W cm^{-2}.

6.4 Results

6.4.1 ω_o calorimetry

The variation of the backscattered energy at 1.06 μm with incident energy is summarised in Fig. 6.2. The error bars represent uncertainties in the instrumental calibration. The light scattered outside the lens cone was not measured so the angular distribution of scattered light was not determined.

It will be seen from Fig. 6.2, that for a fixed target type, the fraction of energy which is backscattered into the focussing lens remains fairly constant over the limited range of irradiance studied. Hence, no saturation of the backscatter level is observed as reported by Offenberger et al (6.5).

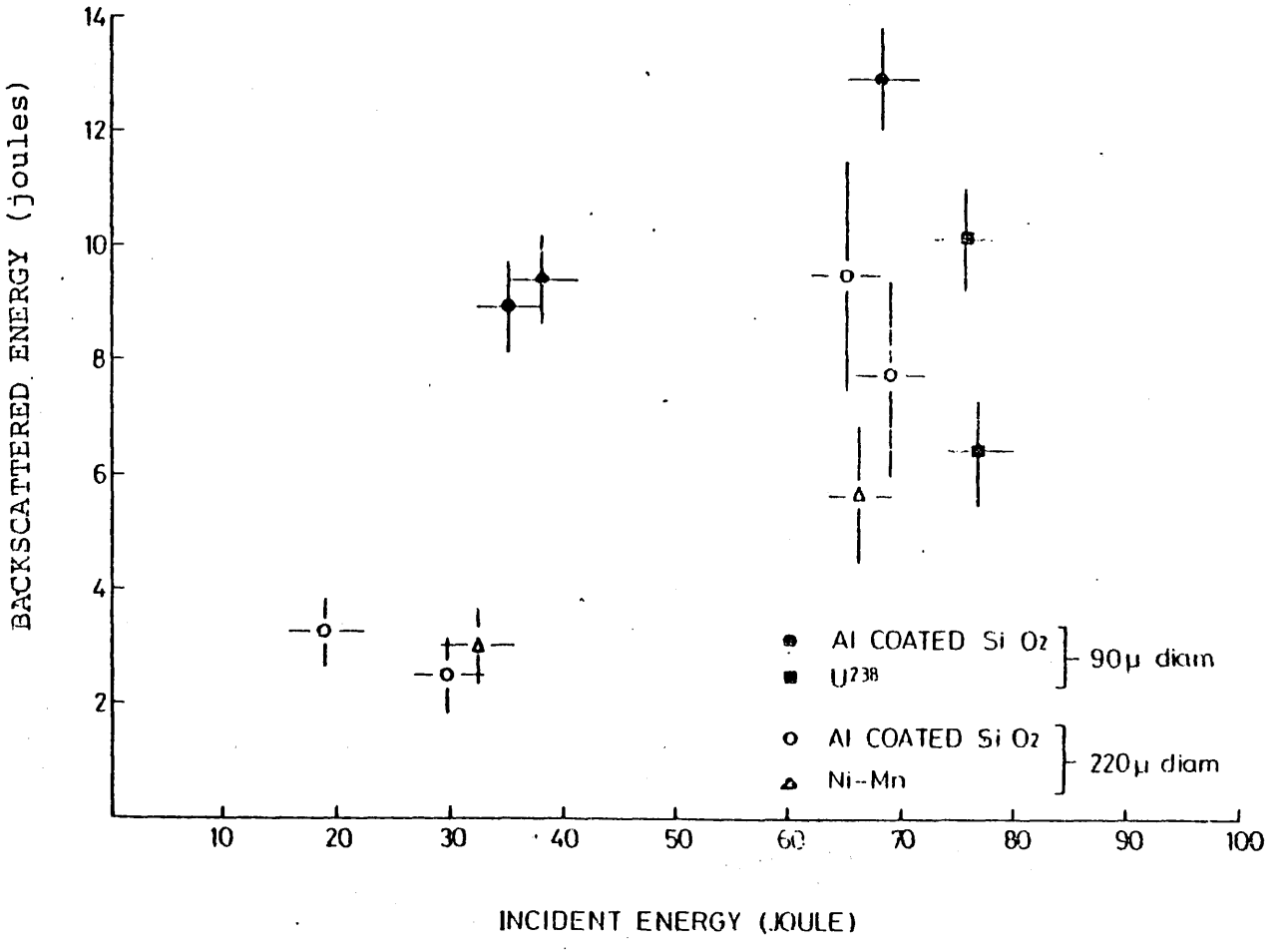

FIG. 6.2 - Graph of incident and backscattered energies.

For low Z targets, small microballons generate more backscattered light (20 - 25%) than large microballoons (10 - 15%) for the same incident energy. Both small and large targets of high Z material exhibit less backscatter (30 - 40% less) compared with the aluminium coated glass microballoons. These results are discussed in Section 6.5.1.

6.4.2 ω_o spectral streaks

Some typical time resolved spectra of the ω_o backscatter are shown in Fig. 6.3. They are characterised by an initial burst < 250 ps of blue-shifted ($\lesssim$ 5 Å) emission, an interval of between 250 - 500 ps, followed by red-shifted emission which then persists throughout the remainder of the laser pulse. This contrasts with observations (6.8) of the backscatter turning off during the incident pulse.

However, a cut-off was observed in the behaviour of ω_o emission from low irradiance ($<10^{14}$ W cm^{-2}) shots on plane brass targets. An example of this is shown in Fig. 6.4. Here, emission spectrally broadened to the blue only, is generated just for the beginning of the incident pulse, with a turn off occurring after about 800 ps.

At high irradiances ($< 10^{14}$ W cm^{-2}) small scale temporal ($\sim$ 80 ps) and spectral ($\sim$ 2 Å) structure is observed. Similar behaviour has been observed by Turner and Goldman (6.9) in their time resolved ω_o spectra, which they attribute to multiple Brillouin scatterings or ion acoustic wave harmonic generation.

On a couple of occasions, modulation of the incident pulse due to mode beating was observed with corresponding modulation of the backscattered emission. This modulation is used to provide information on the Brillouin reflection coefficient for different scale length plasmas (see section 6.5.3).

i) Shot No. 12/130279

$\emptyset = 4.2 \times 10^{14}$ W cm^{-2}

Target:

250 µm Al coated glass microballoon.

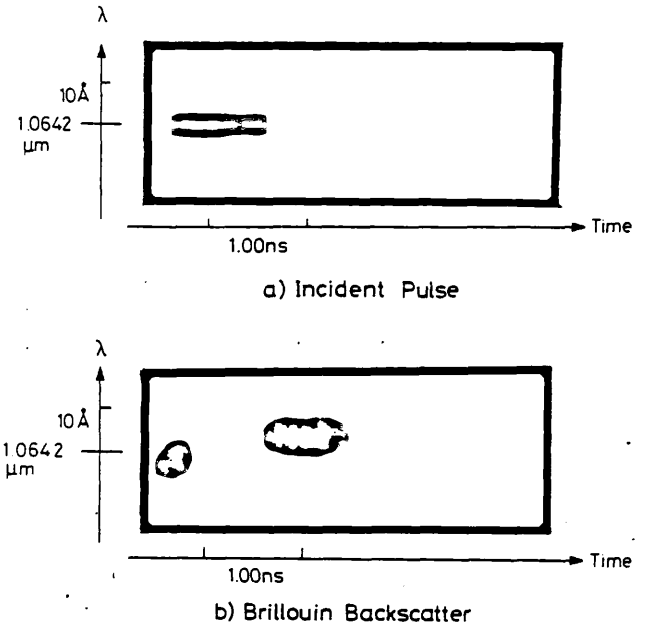

ii) Shot No. 15/130279

$\emptyset = 9.1 \times 10^{14}$ W cm^{-2}

Target:

250 µm Al coated glass microballoon.

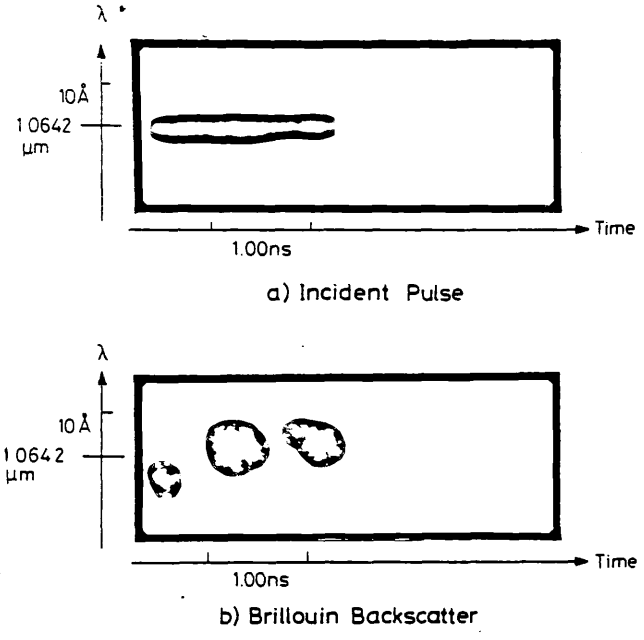

FIG. 6.3 - Time resolved ω_o backscattered spectra

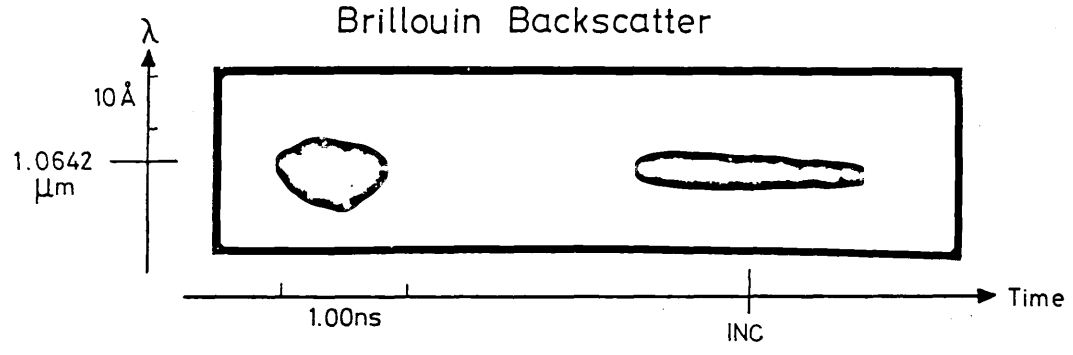

FIG. 6.4 - Time resolved ω_o backscatter from a plane brass target. $\emptyset \sim 10^{13}$ W cm^{-2}.

6.5 Discussion

6.5.1 ω_o Calorimetry

The high Z targets exhibit 30 - 40% less backscatter than the Al-coated glass microballoons. This reduction may be due to the effects of increased absorption for high Z targets. In the underdense plasma there is competition between stimulated Brillouin scattering and inverse bremsstrahlung, the latter being more significant for high Z targets as the coefficient of absorption is proportional to Z^2. If the scale length for inverse bremsstrahlung absorption is less than that for Brillouin scattering then the scattering will be reduced.

Also, the high Z material causes increased line and continuum emission which lowers the coronal electron temperature. However, this has to be balanced against the increased inverse bremsstrahlung absorption but if the electron temperature is reduced the smaller expansion velocity leads to a smaller hydrodynamic scale length and less backscatter.

The scalelength in the underdense plasma can be estimated (6.10) as the focal spot diameter or the ion ablation velocity times the pulse duration, whichever is the smaller. For low Z targets, the larger diameter targets exhibit $\sim$ 50% less backscatter than the smaller diameter ones for the same incident energy. This indicates that the reduced irradiance on the larger diameter targets result in lower electron temperatures, thus reducing the scalelength and hence the backscatter despite the larger irradiated surface.

6.5.2 ω_o Spectral Streaks

The red shift of the backscattered radiation during most of the laser pulse is characteristic of Brillouin scattering. It is believed that the early short blue shifted component is due to specular reflection from the initially steep, moving density step near the critical layer with no Brillouin scattering at this early time. With the evolution of

the underdense plasma, the onset of Brillouin scattering and inverse bremsstrahlung absorption combine to cut off this specular reflection. Towards the end of the laser pulse there is a large underdense plasma where the flow velocity is maintained (6.11), but the incident irradiance is lower than at the peak. Hence, the Brillouin component is reduced but the Doppler component is constant, resulting in a gradual decrease in the overall red shift. This behaviour is also observed by Gorbunov et al (6.4) and Ripin et al (6.3).

The coronal electron temperature can be estimated from the spectral shift by using equation III-28 and the Lawrence Livemore result (6.2) that the Mach number for the flow is 0.82. Unfortunately, this shows that a measurement of the reflected ω_o spectrum is not a good indicator of T_e in the underdense plasma because of the close cancellation of the two contributions to the wavelength shift.

Taking an average value from the high irradiance shots of the Al-coated glass microballoons of $\Delta\lambda = 5$ Å, we have:

$$T_e = \frac{\Delta\lambda}{\lambda_o}\left(\frac{c}{2\,(M-1)}\right)^2 \frac{A}{Z}\, m_p$$

$$= \frac{5}{10640}\left(\frac{c}{2.-0.18}\right)^2 \frac{A}{Z}\, m_p$$

Where $M = 0.82$

m_p = proton mass

Taking $A/Z = 2$, this gives an electron temperature of 3.2 keV and a sound speed of 4×10^7 cm s^{-1}. Rosen et al (6.2) calculated a temperature of 20 ± 10 keV from their Brillouin shifts. Using the scaling adopted in Ref 6.2

$$T_e \sim Z^{2/5}$$

The data of Ref 6.2 for gold (Z = 58) targets imply a temperature for glass microballoons of

$$T_e = \left(\frac{4}{58}\right)^{2/5} 20 \text{ keV} = 6.9 \pm \text{keV}$$

which is in agreement with our result.

6.5.3 Analysis of Mode Beating Shot

Fig. 6.5 shows a shot which exhibits strong mode beating, with four separate pulses, each of about 200 ps FWHM. This was analysed by performing integrations in time and wavelength for the streak record, then normalising to the corresponding calorimeter measurements to obtain the energy contained in each beat of both the incident and backscattered pulses. The ratios of the backscattered to incident energies give the reflectivities for each beat as shown in Table 6.1.

Table 6.1 Reflectivities and scale lengths for Mode Beating Shot

Pulse	1	2	3	4
Reflectivity (%)	6	16	99	∿100
Scale length (μm)	13	23	159	159

The fraction of backscatter associated with the first two beats is small (< 20%) but increases dramatically for the last two beats to about 100%. The backscatter fraction greater than unity is attributed to uncertainties in the film calibration and to the limited dynamic range (∿ 10) of the streak camera.

Density scale lengths may be estimated from the measured reflectivity by using the simple non-linear model described by Kruer (6.12) where the ion waves are limited by ion trapping. He obtains for the reflection coefficient:

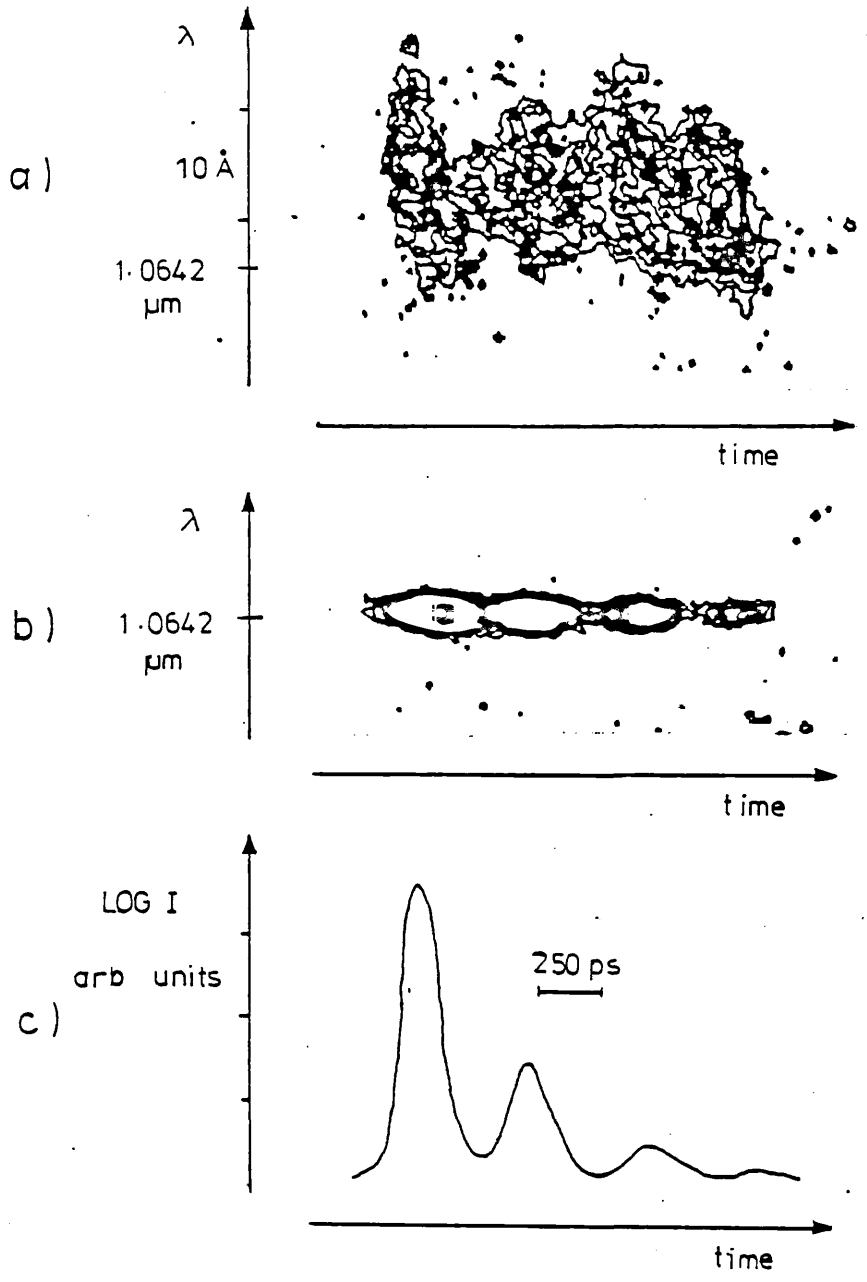

FIG. 6.5 - Modulated Brillouin backscatter resulting from temporal structure (modebeating) in the incident pulse.
a) Isodensity contour map of ω_o backscatter.
b) Isodensity contour map of incident pulse.
c) Microdensitometer trace of incident pulse.

$$r = \left(\frac{1 - \beta^2}{1 + \beta^2} \right) \qquad \text{VI - 3}$$

where $\beta = e^{-\theta}$ and $\theta = \frac{\alpha L \delta n}{n_e}$

$$\alpha = \frac{\pi}{2} \frac{n_e}{n_{CR}} \frac{1}{\lambda_o} \left(1 - \frac{n_e}{n_{CR}} \right)^{-1/2}$$

The amplitude of the ion wave as limited by ion trapping is:

$$\frac{\delta n}{n_e} = \frac{1}{2} \left\{ \left(1 + \frac{T_i}{Z T_e} \right)^{1/2} - \left(\frac{3 T_i}{Z T_e} \right)^{1/2} \right\}^2 \qquad \text{VI - 4}$$

Assuming $T_i << Z T_e$ and putting $T_e/T_i = 10$, the maximum value of $\frac{\delta n}{n_e}$ is $\sim 12\%$. Taking $\frac{n_e}{n_{CR}} = 0.1$ (ref 6.3)

we have,

$$\alpha = \frac{0.166}{\lambda_o} \text{ and } \theta = 0.0199 \left(\frac{L}{\lambda_o} \right)$$

$$\therefore \frac{L}{\lambda_o} \; 0.0199 = \ln \left\{ \left(\frac{1 + \sqrt{r}}{1 - \sqrt{r}} \right)^{1/2} \right\} \qquad \text{VI - 5}$$

For a neodymium laser,

$$L = 26.6 \; \mu m \; \ln \left\{ \left(\frac{1 + \sqrt{r}}{1 - \sqrt{r}} \right) \right\} \qquad \text{VI - 6}$$

which is plotted in Fig. 6.6.

Using this model, the density scale lengths for each of beats are calculated and these are also shown in Table 6.1. The jump in scale

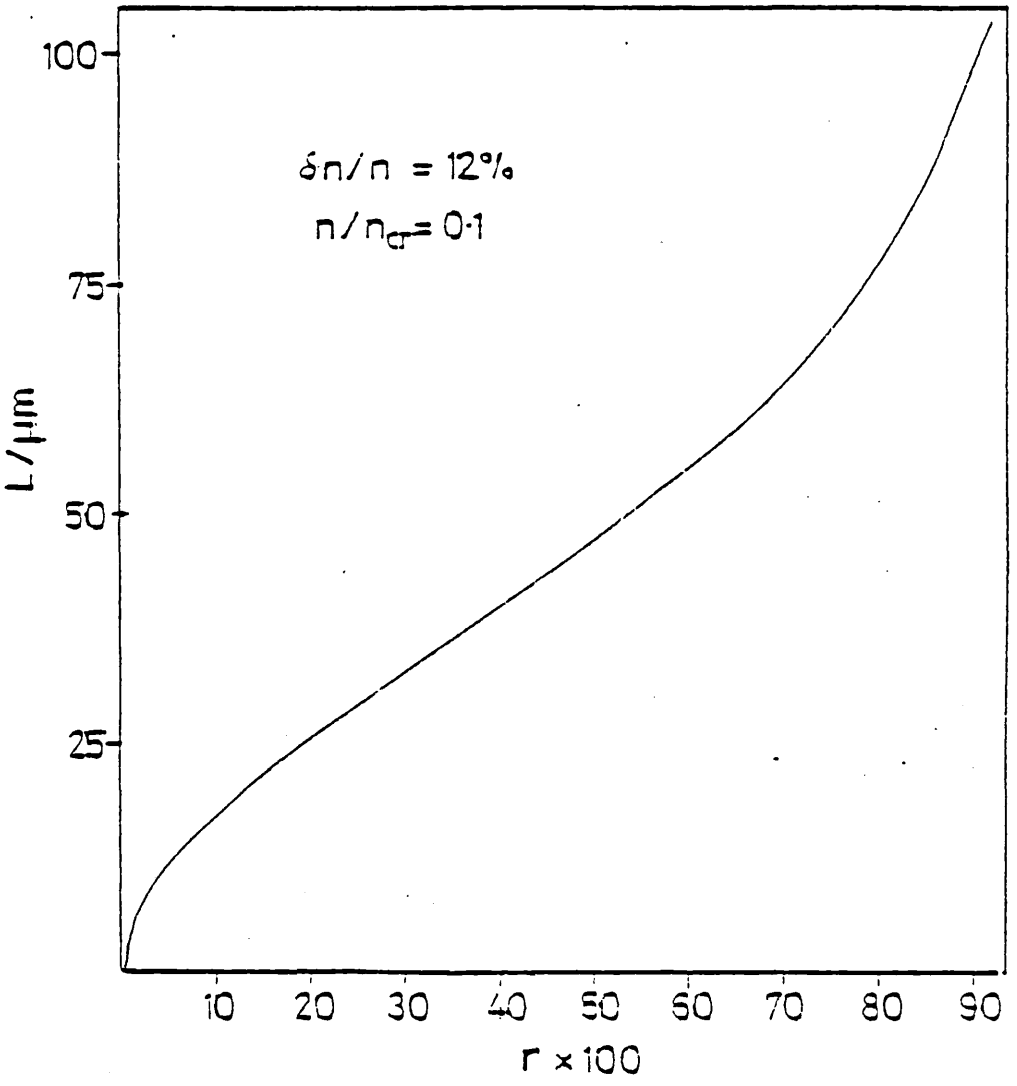

FIG. 6.6 - Density scalelength as a function of reflectivity with the density fluctuation limited by ion trapping.

length between the second and third pulses may be due to the turning off of the ponderomotive force, since the irradiance drops from 7.2 to 1.9 x 10^{15} W cm^{-2} between the two pulses, the latter value being close to the threshold for profile modification (6.13).

The calorimetry shows no saturation level. The ~100% reflectivity for the last two beats are in agreement with the prediction by Evans (6.14), that if Brillouin scattering is only limited by ion trapping, a 1.06 μm laser would produce 100% backscatter given a large enough volume of underdense plasma.

6.6 Conclusion

The main features of the ω_o data reported here are broadly consistent with most reports (6.1 - 6.7). They are:

(i) The red shift in the spectra which is interpreted as evidence of Brillouin scattering.

(ii) Complex structure in time and wavelength. Ref. 6.7 has suggested multiple Brillouin scatterings for (ii), but no satisfactory theoretical models exist at present which explain the data in detail.

Other features do not show such good agreement but in most of the conflicting reports the experimental conditions were different from the present work.

(iii) The ω_o emission is observed to persist for the duration of the incident pulse. This is consistent with the results of Ref. 6.15 where similar conditions existed i.e. $E_L \lesssim 100$ J, $\tau \lesssim 900$ ps. However, Ref. 6.8 reports a cut off which is attributed to profile modification caused by the ponderomotive force.

(iv) The red shifted emission occurs about 300-600 ps after the beginning of the laser pulse. This amount of time indicates the delay required before sufficiently long density scale lengths evolve in the underdense plasma for the onset of the Brillouin instability.

(v) The calorimetry data exhibit less backscatter for high Z targets contrasting with the conclusions of Ref. 6.3 who found little difference between the scattering characteristics of low and high Z targets. They attribute this to the fact that atoms are highly stripped in the hot plasma corona which will therefore expand with similar speeds leading to comparable scale lengths in the underdense plasma for a wide range of Z. However, Ref. 6.3 uses a pre-pulse, unlike here.

(vi) No saturation is observed for the backscatter. Analysis of a mode beating shot gives ∿100% reflectivities for scale lengths of ∿ 160 μm. A jump in the implied scale lengths between the second and third pulse may be due to a turn off in the ponderomotive pressure.

(vii) Estimates of the coronal temperatures and density scale lengths have been made using simple models. The estimate of the electron temperature agrees with the scaling given in Ref. 6.2 i.e. $T_e \sim Z^{2/5}$.

CHAPTER 7

Time-Resolved Studies of Second Harmonic ($2\omega_o$) Emission from Laser Irradiated Spherical Targets

7.1 Introduction

Near the critical density (n_{CR}) surface, second harmonic emission can arise from the interaction of a plasmon, $\omega_p \simeq \omega_o$, with an incident, scattered or reflected photon. Much of the theory of $2\omega_o$ harmonic generation is described by the work of Erohkin et al (7.1 - 7.2), Vinogradov and Pustalov (7.3), and Krohkin et al (7.4). The usual wave matching conditions must be satisfied:

$$\left.\begin{aligned} \omega' + \omega'' &= \omega \\ \underline{k}' + \underline{k}'' &= \underline{k} \end{aligned}\right\} \qquad \text{VII - 1}$$

where ω = wave frequencies and $\underline{k}$ = wave vectors of the coalescing and daughter waves. For an inhomogeneous plasma, the matching conditions can only be satisfied locally. For a homogeneous, isotropic plasma, one, at least, of the two interacting waves must be a longitudinal wave.

$$t' + \ell' \rightarrow t \qquad \text{VII - 2}$$

$$\ell' + \ell'' \rightarrow t \qquad \text{VII - 3}$$

where t = transverse and ℓ = longitudinal oscillations.

The mechanisms responsible for the generation of plasma waves with frequency $\omega_p \simeq \omega_o$ near n_{CR} are examined below.

7.2 Oblique Incidence Generation

The plasmon generated by resonance absorption (section 3, Chapter 3) can coalesce with a photon ($\ell' + t'$) or another plasmon ($\ell' + \ell''$) to give rise to $2\omega_o$ emission. This mode of second harmonic generation can only

occur under the same conditions as resonance absorption i.e. it also requires a p-polarised wave at oblique incidence. The angular variation of the second harmonic emission should also follow the Ginzburg absorption curve (7.5) i.e. a maximum is reached for an optimum angle of incidence given by:

$$\theta = \left(\frac{2\pi L}{\lambda}\right)^{2/3} \sin^2\theta \simeq 0.6 \qquad \text{VII-4}$$

The intensity of the second harmonic emission should also increase quadratically with the intensity of the incident radiation.

This mode of generation is expected to dominate at weak irradiances below the threshold for the parametric decay instability.

7.3 The Silin Model (7.4)

At higher irradiances, exceeding the parametric decay threshold, this instability can excite electron oscillations with frequency $\omega_p \simeq \omega_o$ near n_{CR} as described in Section 3.4.1. . The $2\omega_o$ harmonic can then result from the interaction of the parametrically excited electron wave with an incident or reflected electromagnetic wave. The second harmonic component will be shifted in frequency to the red by an amount equal to the frequency of the ion acoustic wave, ω_{ia} , generated by the parametric decay instability:

$$\Delta\omega = 2\omega_o - 2\omega = \omega_{ia} \qquad \text{VII - 5}$$

where $\omega_{ia} = k_{ia}\, c_s$

k_{ia} = wave number of ion acoustic wave

c_s = sound velocity in the plasma

Near the neighbourhood of n_{CR} , the wave vector of the pump, $\underline{k}_o$ is very small, hence it can be shown:

$$| \underline{k}_{ia} | = \sqrt{3}\, \omega_o / c$$

Furthermore, the equation $\omega_o c_s = \omega_{Li} v_{th}$ connects the velocity of the sound waves and the thermal velocity of the electrons, where ω_{Li} is the Langmuir ion frequency, hence:

$$\Delta\omega = \sqrt{3}\ \omega_{Li}\ \frac{v}{c}th \qquad \text{VII - 6}$$

This calculation for the frequency shift of the 2ω component does not take into account the non-linear effects associated with the electron oscillation in the electric field of the wave. This causes a correction which becomes important at higher irradiances where it is necessary to use the non-linear dispersion relation for the ion acoustic waves.

$$\omega_{ia} = k_{ia} \left(c_s^2 + \frac{m_e}{4m_i} \frac{\omega_o}{\Delta\omega_o} v_{os}^2\right)^{1/2} \qquad \text{VII - 7}$$

in which v_{os} is the oscillation velocity of electrons in the electric field of the incident wave, and $\Delta\omega_o$ the difference in the frequency of the laser wave and the local plasma frequency:

$$\Delta\omega_o(x) = \omega_o - \omega_p(x)$$

$$= \omega_o \frac{x}{2L}$$

$$\Delta\omega_o(x) = \frac{1}{2}\omega_o \left(\frac{c}{L\omega_o}\right)^{2/3} \qquad \text{VII - 8}$$

where x corresponds to the distance between the critical layer and the region of the plasma where the electric field, described by an Airy function, is a maximum.

The displacement to the red of the second harmonic is then:

$$\Delta\omega = \sqrt{3}\,\frac{\omega_o}{c}\left(c_s^2 + \frac{1}{4}\frac{m_e}{m_i}\,\frac{\omega_o}{\Delta\omega_o(x)}\,v_{os}^2 \right)^{1/2}$$

$$\Delta\omega = \sqrt{3}\,\omega_{Li}\left\{\left(\frac{v_{th}}{c}\right)^2 + \frac{1}{4}\frac{v_{os}^2}{c^2}\,\frac{\omega_o}{\Delta\omega_o(x)}\right\}^{1/2} \qquad \text{VII - 9}$$

Comparing this to equation VII - 6, it can be seen that this is the same expression with the addition of a second term which is the correction term for higher flux.

This displacement can be expressed as a function of the fundamental plasma parameters: the local gradient length L, and the irradiance Φ at the critical density layer, by using the following relation:

$$v_{os} = \frac{e\,E_o}{m\,\omega_o} \qquad \text{VII - 10}$$

$$= \frac{e}{m\,\omega_o}\left(\frac{\Phi}{\varepsilon_o c}\right)^{1/2} \qquad \text{VII - 11}$$

giving, $\Delta\omega = \sqrt{3}\,\omega_{Li}\left\{\left(\frac{v_{th}}{c}\right)^2 + \frac{1}{2}\,\frac{e^2}{\varepsilon_o m^2 c^{11/3}}\,\frac{L^{2/3}}{\omega_o^{4/3}}\,\Phi\right\}^{1/2}$ VII-12

For Nd/glass radiation, equation VII - 12 can be represented in more practical units:

$$\Delta\lambda = \frac{\Delta\omega}{4\omega_o}\,\lambda_o = \left(\frac{Z}{A}\right)^{1/2}\left\{ 20T_e + 7 \times 10^{-15}\Phi\left(\frac{L}{\lambda_o}\right)^{2/3}\right\}^{1/2} \qquad \text{VII - 13}$$

where the red shift $\Delta\lambda$ is in Å

electron temperature T_e in keV

irradiance Φ in W cm^{-2}

A is the atomic number of the target material

Z is the charge of the target material

A cascade process can ensue whereby the parametrically created plasma wave can decay into another plasma wave and an ion acoustic wave:

e.g. $\omega_o \rightarrow \omega_p + \omega_{ia}$

$\omega_p \rightarrow \omega_{p'} + \omega_{ia}$

$\omega_{p'} \rightarrow \omega_{p''} + \omega_{ia}$ and so on.

Second harmonic emission can be generated by the interaction of an electromagnetic wave with a subsidiary plasma wave:

$\omega_o + \omega_{p'} \rightarrow 2\omega' + \omega_{ia}$

$\omega_o + \omega_{p''} \rightarrow 2\omega'' + \omega_{ia}$ and so on.

Hence the spectrum of the second harmonic will broaden towards the red.

7.4 The Cairns Model

The Cairns model (7.6) shows that at high irradiances the spectrum of plasma waves generated by the resonance absorption process can be broadened via an ion sound wave, with a corresponding broadening in the second harmonic spectrum.

In a stationary density profile, the resonance absorption process will only produce plasmons at the same frequency as the incident radiation. However, ion acoustic waves may be generated in the vicinity of the critical surface by various mechanismse.g. heat flux instabilities. An ion acoustic wave propagating through the critical surface can lead to a coupling of the incident radiation to plasma waves, whose frequency

differs from that of the incident wave by integral multiples of the ion acoustic frequency.

For supersonic flow of the plasma through the critical surface, the ion acoustic wave propagates outwards, so that energy is preferentially transferred to the lower frequency components. This leads to a broadening of the spectrum to the red.

Cairns has derived the following set of equations describing the generation and coupling of a set of plasma waves at frequencies differing from the laser frequency by multiples of the ion acoustic frequency, ω_{ia} :

$$\beta \frac{d^2E}{dy^2} + \left(y - 21 \frac{\omega}{\omega}ia \right) E_L = \varepsilon e^{-ik_{ia}y} E_{L-1} + \varepsilon e^{-ik_{ia}y} E_{L+1}$$

(+ driving term) VII - 14

where the driving term is the high frequency oscillation field along the density gradient produced by an obliquely incident component of the laser radiation; $\beta = 3 v_e^2/\omega^2 L^2$ and k_{ia} , the wave number of the ion acoustic wave, is taken to be in units of 1/L. If the electron temperature is in keV and the scale length L is in units of $2\pi c/\omega$, then:

$$\beta \simeq 1.5 \times 10^{-4} T_e/L^2 \qquad \text{VII - 15}$$

The solution of equation VII - 14 depends on β, ε, ω_{ia}/ω and k_{ia} . However, numerical results indicate that the solution is insensitive to changes in ω_{ia}/ω. Fig. 7.1 shows a number of spectra plotted for fixed values of β and ε but with k_{ia} varying. Near the critical density surface, Manheimer and Klein (7.7) have shown that $k_{ia} \sim \frac{2}{3} \pi \beta^{-1/3}$, which gives the value 39.5 for the parameters considered by Cairns.

This value of k_{ia} agrees well with the value $k_{ia} = 35$, obtained from the simulations for the case of maximum energy transfer from the driven

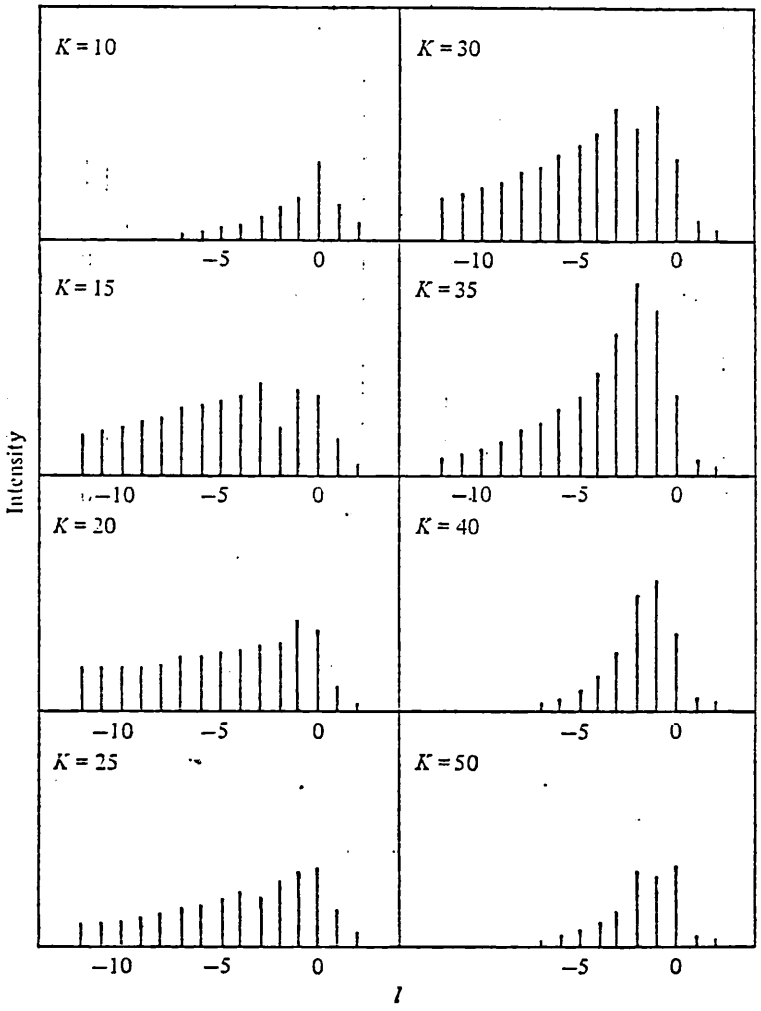

FIG. 7.1 - Spectra for $\beta = 1.5 \times 10^{-4}$, $\varepsilon = 0.1$ and various values of K. (after R.A. Cairns. J. Plasma Physics 22, 149 (1979)).

modes into the laser frequencies.

The wavelength shift in the second harmonic is given by:

$$\frac{\Delta\lambda}{\lambda} = \frac{1}{4}\frac{\omega}{\omega}_{ia} \qquad \text{VII - 16}$$

where λ is the wavelength of the laser.

Neglecting the effects of plasma motion, the ion acoustic frequency is given by Cairns as:

$$\omega_{ia} = \left(\frac{Z}{A}\right)^{1/2}\left(\frac{m_e}{m_i}\right)^{1/2} k_{ia}\left(\frac{\beta}{3}\right)^{1/2} \qquad \text{VII - 17}$$

for a Nd/glass laser and $k_{ia} = \frac{2}{3}\pi\beta^{-1/3}$

$$\Delta\lambda \simeq 50\beta^{1/6}\ \text{Å} \qquad \text{VII - 18}$$

For typical experimental values of $\beta < 1.5 \times 10^{-4}$, this gives displacements of a few angstroms, which with a total width of ten to twenty sidebands, gives a spectrum whose width and shape are consistent with observations (7.8).

7.5 Review of Experimental Evidence for Second Harmonic Emission

There have been many observations reported of the second harmonic emission from laser irradiated targets. Evidence for the oblique incidence generation mechanism of $2\omega_o$ harmonic has been reported by several groups (7.8 - 7.10). One of the most thorough studies was performed by Eidmann and Sigel (7.12) in experiments with the Garching Nd/glass laser facility, using 20 J, 5 ns pulses focussed onto plane solid targets by an f/1 aspherical lens. By masking off the right-hand side of the round incident lens, the spatial distribution of the second harmonic

which was backscattered through the lens was shown to be specularly reflected for p-polarised incident light by simple ray tracing techniques. The energy of the second harmonic radiation was measured as a function of the incident laser energy and shown to have a quadratic relationship. Finally, the polarisation of the second harmonic was checked and found to be linearly polarised.

The second harmonic emission has also been spectrally resolved (7.5, 7.11, 7.13) : Bobin et al (7.14) reported broadening to the red in their experiment with a 15 ns Nd/glass laser pulse incident on a hydrogen stick. Further investigations, by Decroisette et al (7.15), revealed a sharp line imposed on the red wing, implying two different generation mechanisms were involved. The unshifted line was attributed to the oblique incidence mechanism, while the broadening of the spectrum was interpreted as evidence of parametric turbulence.

Time resolved studies of the second harmonic emission have also been made. Jackel et al (7.16) looked at the sidescattered second harmonic emission from spherical targets irradiated by the LLE Nd/glass laser. From streak photographs, they measured the velocity of the critical density surface to be $\sim 10^7$ cm s^{-1} for incident pulse durations of 600 ps. The temporal profile of the second harmonic emission intensity was found to follow that of the incident pulse, but, on a few shots, uncorrelated dips in the intensity were observed. The authors were uncertain whether this represented an actual modulation in the intensity or a shift of the second harmonic emission to frequencies outside the window of their transmission filter. However, dips in the $2\omega_o$ intensity were also noted by Bychenhov et al (7.17) in their time resolved spectral studies, indicating that true modulation was observed.

By simultaneously streaking the $3\omega_o/2$ harmonic emission, Jackel et al (7.18) were able to obtain a value for the scalelength between the critical and quarter critical surfaces of 10 - 30 μm. When Saleres et al (7.19) used a longer incident pulselength, 2.8 ns, they measured

a correspondingly longer scalelength of 60 - 180 μm. They also found that the $2\omega_o$ intensity followed the incident pulse, but was of slightly shorter duration. No modulations in the intensity uncorrelated to the incident light were observed.

The above reports are just a sample of the many observations of second harmonic emission made in recent years. Fur further details, reference should be made to the excellent review article by Basov et al (7.20).

7.6 Experimental Method

The work presented in the rest of this chapter is the result of new temporally and spectrally resolved observations of the second harmonic emission from Nd/glass laser irradiated spherical targets. The experiment was performed with incident pulse lengths of ∿100 ps and ∿ 1.8 ns. For the former a peak irradiance of $\sim 10^{16}$ W cm^{-2} was obtained for an incident energy of 30 J and for the latter a peak irradiance of $\sim 4 \times 10^{15}$ W cm^{-2} was obtained for an incident energy of 100 J. Slightly different experimental arrangements were used for the two incident pulse lengths and these are described separately.

Fig. 7.2 shows the experimental layout for the shorter pulse length observations. TheD-T filled glass microballoon (diameter 70 - 90 μm) targets were irradiated by two opposing beams of the Nd/glass laser. The light backscattered through the east aspheric singlet focussing f/1 lens was imaged onto the slit of the SPEX spectrograph with the 1200 lines mm^{-1} grating. The output plane of the spectrograph was then optically coupled to the Electrophotonics Ltd. streak camera with an S-20 photocathode.

The spectral resolution was limited by the entrance slit width of the spectrograph to ∿ 1 Å , with no further loss of resolution at the streak camera. The temporal resolution of the streak camera (determined by the camera entrance slit width) was about 7 ps, but that of the whole

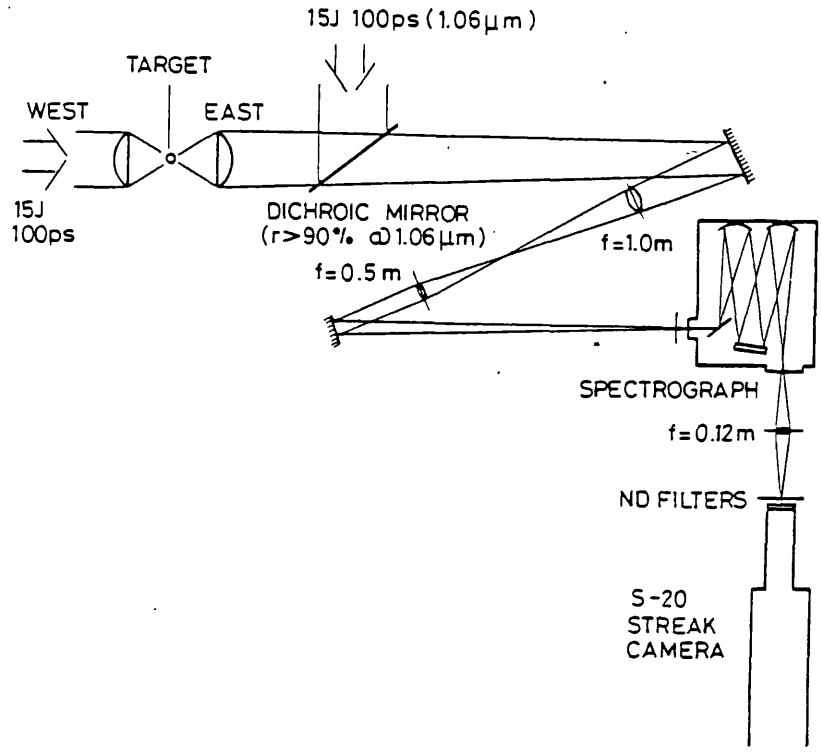

FIG. 7.2 - Experimental layout for $2\omega_o$ time resolved spectroscopy with incident pulselength = 100 ps.

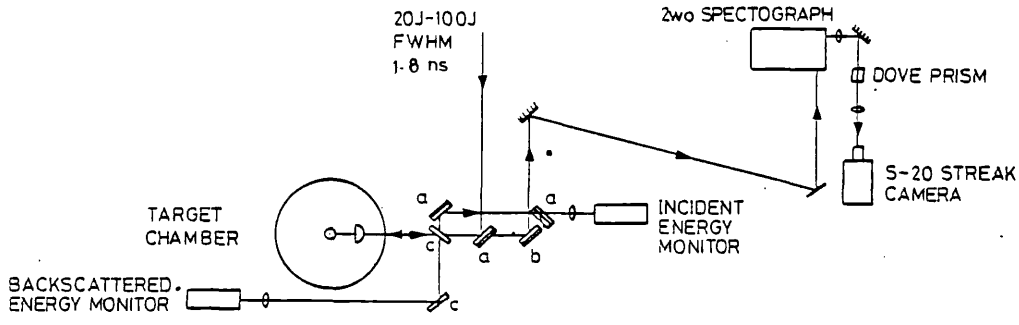

FIG. 7.3 - Experimental layout for $2\omega_o$ time resolved spectroscopy with incident pulselength = 1.8 ns.

system was limited by the range of path lengths in the spectrograph to 10 ps. The spatial resolution in the target plane was limited by the f/1 lens to about 10 μm at 5320 Å.

The streak data were recorded photographically on Kodak 2485 film which was developed at 30°C for 5 minutes in D19 solution. Separate exposures of 5461 Å Hg I line were taken with the spectrograph at different wavelength settings to calibrate the data for wavelength and dispersion. This method of calibration had the disadvantage of relying on the accuracy and reproducibility of the grating drive mechanism, but the errors in that amounted to < 1 Å . The energy on the target was kept constant although a slight variation of the laser output was experienced in practice. The jitter of the streak camera was 2 - 3 ns which was greater than the temporal window ∿ 1.1 ns, hence a large number of shots was required to obtain reproducible data.

Fig. 7.3 shows the experimental layout for the longer incident pulse length laser which was performed concurrently with the Brillouin experiment reported in the previous Chapter. Only one beam of the Nd/glass laser was used and this was focussed onto microspheres and microballoons by the f/1 aspheric doublet lens. The backscattered $2\omega_o$ harmonic emission was diverted to the Spex spectrograph with the 1200 lines mm^{-1} grating. This time the output of the spectrograph was optically coupled to the Hadland Photonic streak camera fitted with an S-20 photocathode. As the streak camera entrance slit is vertical a dove prism was used to rotate the dispersed output from the spectrograph, so that wavelength lay along the camera slit. The spectral and temporal resolutions were ∿ 1 Å and ∿ 20 ps respectively. The streak data were recorded and calibrated in the same manner as in the short pulse length experiment.

The targets were the same as reported in section 6.3, Chapter 6. As also reported in this section the peak irradiance for a beam energy of 100 J on a small target (diameter ∿ 70 - 90 μm) was 4×10^{15} W cm^{-2}

irradiance was 5×10^{14} W cm^{-2} . A range of data was obtained by varying the laser energy incident on the target.

7.7 Results

Time resolved spectra of the second harmonic emission obtained for a short ($\sim$ 100 ps) incident pulse on targets are shown in Fig. 7.9. They display similar spectral widths and broadening to those seen in the time integrated spectrum (7.8). However, the most striking feature of the data is the appearance of intense, spectrally and temporally resolution limited emission spots in the ($\tau\lambda$) plane. The majority of the spots lie in a region centred on the nominal $2\omega_o$ position.

Time resolved spectra of the second harmonic emission obtained for a long ($\sim$ 1.8 ns) incident pulse on spherical targets are shown in Fig. 7.5. At low irradiances ($\lesssim 10^{14}$ W cm^{-2}) the second harmonic emission is spectrally narrow (< 2 Å) and moves continuously in wavelength, presumably due to a Doppler shift given by equation III - 27: $\frac{\Delta\lambda}{\lambda} = \frac{2\ v_a}{c}$. For the experimental paramenters used here, $v_a \sim 10^7$ cm s^{-1}, which for $\lambda_{2\omega} = 5320$ Å , gives a Doppler shift $\Delta\lambda_D \sim 3.5$ Å. At slightly higher irradiances, the second harmonic emission begins with a burst of spectrally broad emission $\sim$ 20 Å, and then reverts to spectrally narrow emission. At irradiances $\gtrsim 10^{15}$ W cm^{-2} the spectrally broad emission persists throughout the laser pulse. The spectrally broad emission is also characterised by the presence of discrete temporal pulses, each close to the instrumental limit of time resolution, with periodic structure in the spectral direction as well.

7.8 Discussion

At the critical density, two mechanisms for generating plasmons of frequency $\omega_p \simeq \omega_o$ exist: resonance absorption and the parametric decay instability. The former has no threshold and in a stationary density profile will produce only plasmons at the same frequency as the incident radiation. The latter has a threshold and the frequency of the parametrically created plasma wave is shifted to the red by an amount

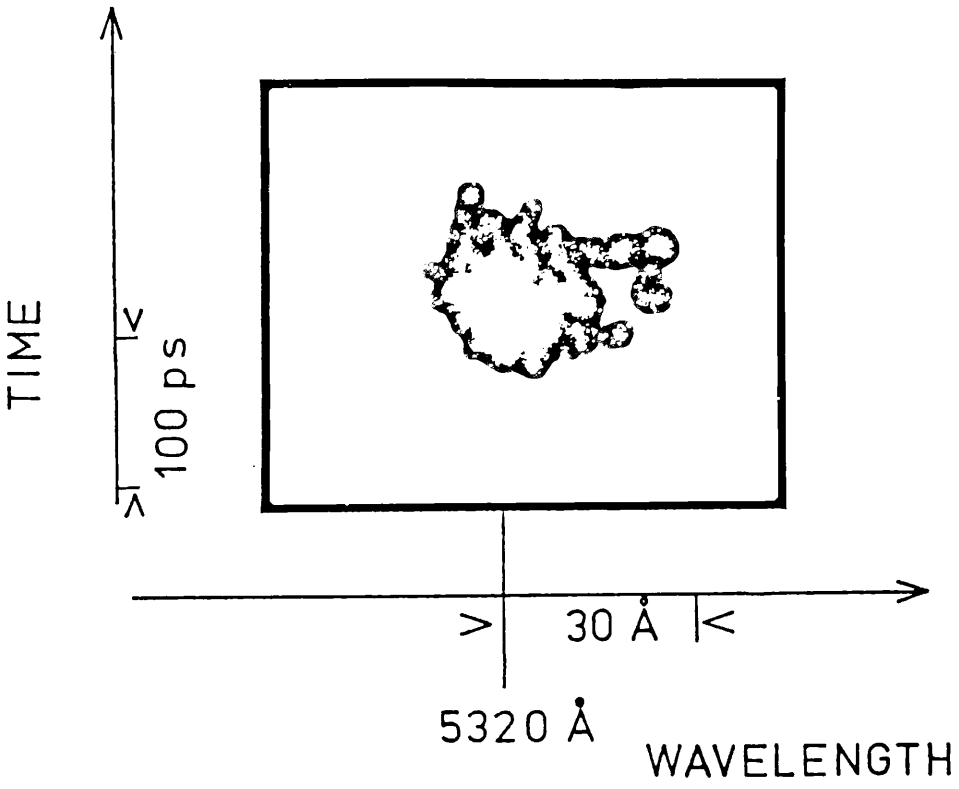

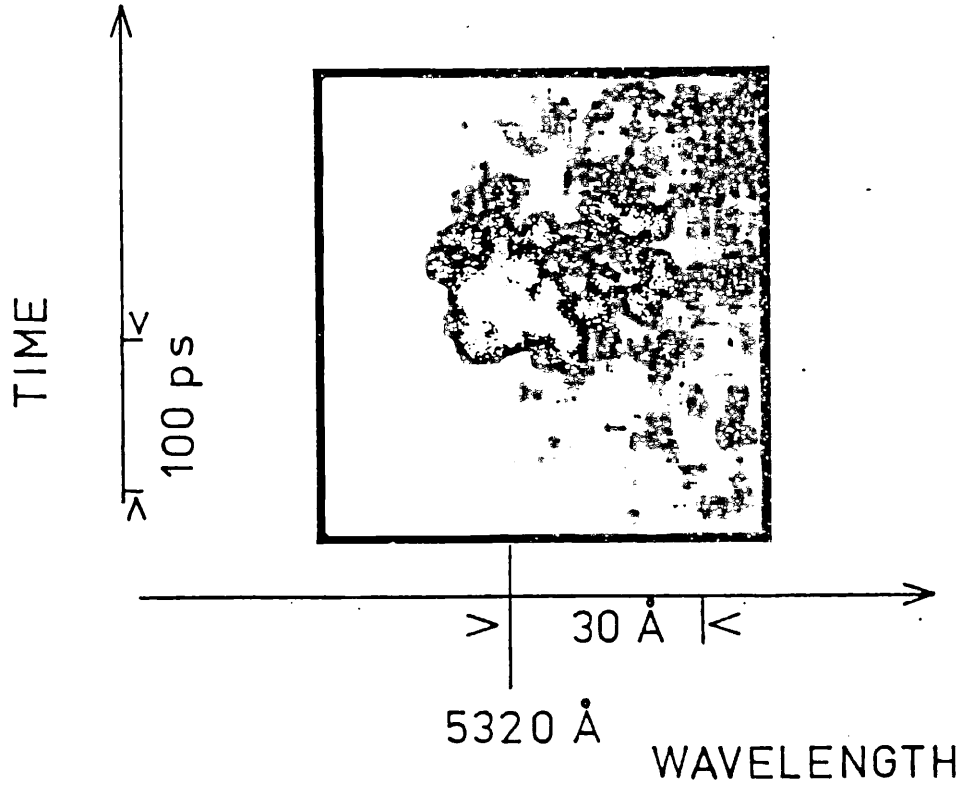

FIG 7.4 - Examples of time resolved $2\omega_o$ spectra with 100 ps incident pulse. a) and b) E_{inc} = 15 J x 2; Target = 80 μm diameter microballoon.

a) Shot No. 12/130279

$\phi = 4.2 \times 10^{14}$ W cm^{-2}

Target:
250 μm Al coated glass microballoon.

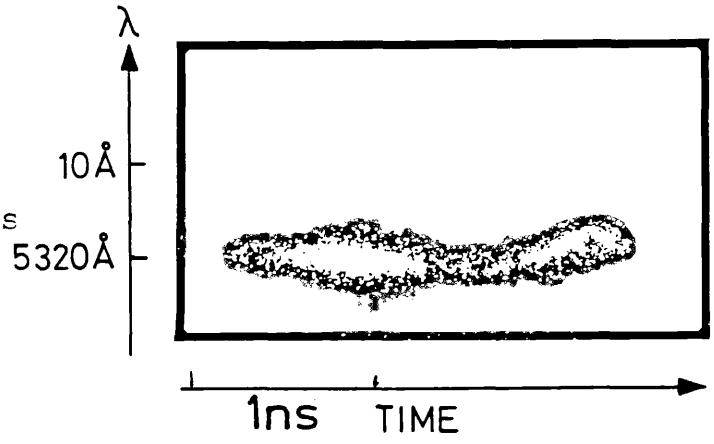

b) Shot No. 15/130279

$\phi = 9.1 \times 10^{14}$ W cm^{-2}

Target:
250 μm Al coated glass microballoon

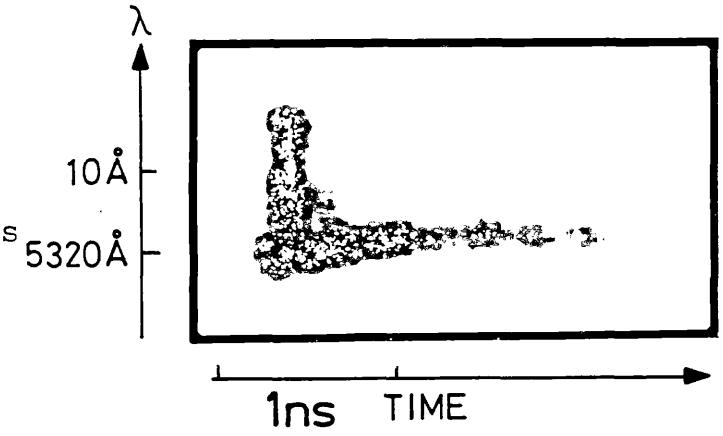

c) Shot No. 7/150279

$\phi = 3.5 \times 10^{15}$ W cm^{-2}

Target:
85 μm Al coated glass microballoon

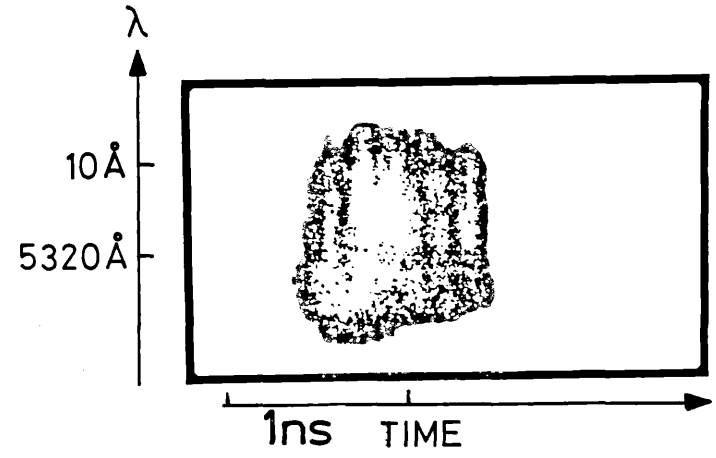

FIG. 7.5 - Examples of time resolved $2\omega_o$ spectra with 1.8 ns incident pulse

equal to the frequency of the ion wave.

In previous observations of the second harmonic emission by Decroisette et al (7.15) both mechanisms were invoked to explain the appearance of a spectrum with a sharp line imposed on a red wing. The unshifted line was attributed to the oblique incidence generation mechanism, while the broadening of the spectrum was interpreted as evidence of parametric turbulence. However, the time resolved spectrally broad second harmonic emission obtained here, do not show the evolution of the cascade process described in section 7.3. Instead, the observations can be explained just by processes involving plasmons generated by resonance absorption.

The difference between the spectrally broad and narrow emissions at $2\omega_o$ (observed for incident pulse length of 1.8 ns) correlate with the appearance of steep density gradients near n_{CR}. In the presence of a steep density profile, resonance absorption is enhanced (see Chapter 3) whereas the threshold for the parametric decay instability increases, since the threshold is inversely proportional to density scale length. Resonance absorption produces fast electrons and the cold electron return current required to maintain charge neutrality in the plasma can drive ion acoustic turbulence. Cairns has demonstrated (7.6) that large amplitude ion waves can induce a spectrum of electron plasma frequencies resulting in a broadened second harmonic spectrum. This mode of generation of second harmonic emission can explain the present observations.

At low irradiances, $\lesssim 10^{14}$ W cm^{-2}, below the threshold for density profile steepening by the ponderomotive force, the spectrally narrow second harmonic emission is attributed to the oblique incidence generation method (section 7.2) which accompanies the resonance absorption process. At moderate irradiances, $\lesssim 5 \times 10^{14}$ W cm^{-2} the ponderomotive force is insufficient to cause steepening of the density profile, but a steep profile exists in the initial part of the laser pulse, coincident with the appearance of the broad second harmonic emission, before significant hydrodynamic motion of the plasma occurs. At higher irradiances $< 10^{15}$ W cm^{-2}, when the second harmonic emission is observed to be

spectrally broad for the duration of the laser pulse, steep density profiles are also expected to exist in the plasma throughout the laser pulse due to the ponderomotive force.

The spectrally broad (~ 30 Å) second harmonic emissions observed for short incident pulse lengths (~ 100 ps) are also explained by the above generation mechanism, since the irradiance of $\sim 10^{16}$ W cm^{-2} incident in all these shots is sufficient (7.21)for significant ponderomotive force steepening of the density profile.

When the second harmonic emission is spectrally broad it also consists of discrete bursts, where the duration of each pulse of emission is less than the temporal resolution of the diagnostic system. Several explanations are possible for this pulsed nature. It may be that individual plasma waves grow on picosecond timescales and saturate, or the observations may be due to spatial motion of several discrete emitting regions through the source area observed with a speed $\gtrsim 10^{8}$ cm s^{-1}, or to rapid variations in the direction of emission in a narrow period from a stationary source, possibly associated with rippling of the critical density surface (7.22).

However, similar pulsed behaviour is observed in the three-halves harmonic emission (see Chapter 8) and there is no reason why different densities should exhibit similar behaviour except for the hydrodynamic flow in the expansion of the plasma. Since the oscillations in the second harmonic emission occur only when the density profile is significantly steepened, it is reasonable to suggest that the ablation flow across the density step may be unstable (7.23).

These density fluctuations then propagate out through the critical density to the quarter critical density region and affect both the second and three-halves harmonic emissions. The timescale of such fluctuations is expected to be $\tau \sim L/v_{ia}$ where L is the density scale length at critical density and v_{ia} is the ion acoustic speed. Taking reasonable values of L ~ 3 μm (cf Ref. 7.21), $v_{ia} \sim 2 \times 10^{7}$ cm s^{-1}, then $\tau \sim 15$ ps

which agrees approximately with the observations.

7.9 Conclusion

The main conclusion drawn from the present study of backscattered second harmonic emission from laser irradiated spherical targets, is that the spectrally broad second harmonic emission is caused by the broadening of the spectrum of electron plasma waves produced by resonance absorption. This interpretation differs from previous studies (7.15) where the presence of a broad second harmonic spectrum was attributed to the occurence of the parametric decay instability.

On present reports, it is difficult to distinguish experimentally between the models suggested by Silin and Cairns, since, although independent experimental evidence (7.24) exists for the presence of resonance absorption in laser plasmas, and much experimental (7.12, 7.25) and theoretical (7.26) work associating second harmonic generation with resonance absorption, there is as yet, no independent evidence for the presence of the parametric decay instability, which has only been inferred from observations of a broadened second harmonic spectrum.

CHAPTER 8

Time-Resolved Studies of Three-Halves Harmonic ($3\omega_o/2$) Emission from Laser Irradiated Spherical Targets

8.1 Introduction

Time-resolved studies of the three-halves harmonic spectral emission from Nd/glass laser irradiated microballoon targets are presented here with higher ($\sim$ 12 ps) temporal resolution than in previous reports (8.1 - 8.3). These results are compared with simple theoretical models which indicate that observations of the three-halves harmonic spectrum may provide a diagnostic for the electron temperature in the underdense plasma.

8.2 Three-Halves Harmonic ($3\omega_o/2$) Generation

Near the quarter critical density surface, two mechanisms exist, which can generate plasmons with the frequency $\simeq \frac{\omega}{2}o$: the stimulated Raman instability and two plasmon decay, both of which have already been discussed in Chapter 3. The $\frac{3\omega}{2}o$ harmonic emission can then arise as a result of the interaction of a photon with a plasmon or the coalescence of three plasmons i.e.

$$\omega_o + \frac{\omega}{2}o \rightarrow \frac{3}{2}\omega_o \qquad \text{VIII - 1}$$

or,

$$\frac{\omega}{2}o + \frac{\omega}{2}o + \frac{\omega}{2}o \rightarrow \frac{3}{2}\omega_o \qquad \text{VIII - 2}$$

Although the second mechanism is a non-linear process of a higher order than the first, it can have an equivalent efficiency due to the difficulty of obtaining the matching conditions for the wave vectors for

the first process.

In an inhomogeneous plasma, the dominant generation mechanism for plasmons in the $\frac{n_{CR}}{4}$ region is believed to be the two plasmon decay, as stimulated Raman scattering has the higher threshold (8.4). The two plasmon instability can produce a forward-scattered plasmon (ω_1 , $\underline{k}_1$) and a backscattered plasmon (ω_2 , $\underline{k}_2$) from the incident photon (ω_o , k_o) as shown in Fig. 8.1.

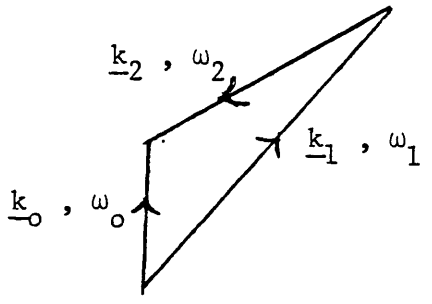

Fig. 8.1

From the geometry, it is obvious that $k_2 < k_1$, hence $\omega_2 < \omega_1$. As the two plasmons result from the decay of an incident photon, (ω_o , $\underline{k}_o$) : $\omega_2 \lesssim \frac{\omega_o}{2} \lesssim \omega_1$. The recombination of a photon with a plasmon to generate light near to $3\omega_o/2$ results in either a photon with a slightly higher frequency than $3\omega_o/2$ or one with a slightly lower frequency. Hence, there are two components of three-halves harmonic emission - one shifted to the blue and the other to the red from the wavelength corresponding to $3\omega_o/2$ exactly. The red-shifted component is directly backscattered at the $n_{CR}/4$ surface, but the blue-shifted component is forward scattered to the 9 $n_{CR}/4$ surface, where it suffers some absorption upon being reflected. The blue-shifted component is therefore expected to be less intense than the red-shifted component when observed in the scattered light spectrum.

8.3 The Avrov Model

The spectrum of the three-halves harmonic emission has been calculated by Avrov (8.5) assuming that the wavelength of the parametrically excited plasmons is much shorter than the pump wavelength i.e. $k >> k_o$. The generation mechanism for the $\omega_o/2$ plasmons is assumed to be the two plasmon decay since it has a lower threshold than the stimulated Raman

scattering instability. The dispersion relation for the plasmons is:

$$\omega_t \ (\underline{k}) = \frac{1}{2} \omega_o \ \left(1 + \frac{3}{2} \ \underline{k} \ \underline{k}_o \ r_{De}^{\ 2} \right) \qquad \text{VIII - 3}$$

where r_{De} = electron Debye radius

For the process where a photon interacts with a plasmon, Avrov calculates the shift of each satellite from the nominal $3\omega_o/2$ position:

$$\Delta\omega_{3/2} = 4.6 \times 10^{-3} \ T_e \ \omega_o \ | \cos \theta |$$

Therefore,

$$\Delta\lambda_{3/2} = 21.7 \ T_e \ | \cos \theta | \ \text{Å} \qquad \text{VIII - 4}$$

The width of the satellite is given by:

$$\delta\omega_{3/2} = 2.3 \times 10^{-2} \ \omega_o \ T_e^{\ 1/2} \qquad \text{VIII - 5}$$

For the coalescence of three plasmons, Avrov predicts a frequency shift given by:

$$\Delta\omega_{3/2} = 4.8 \times 10^{-3} \ T_e \ \omega_o \cos \theta$$

Therefore,

$$\Delta\lambda_{3/2} = 22.7 \ T_e \cos \theta \ \text{Å} \qquad \text{VIII - 6}$$

Where the sign of the frequency shift depends on the scattering angle θ.

There will be a small correction to these equations due to Doppler shifts arising from the expansion of the plasma. However, forboth processes,

Avrov predicts the separation between the blue and red shifted peaks is independent of the incident irradiance, but, in the backscatter direction, will depend only on the electron temperature, T_e. Hence, observation of the $3\omega_o/2$ harmonic spectrum may provide an evaluation of the electron temperature in the corona.

8.4 The Barr Model

Barr has calculated (8.6) the spectrum of the $3\omega_o/2$ harmonic emission for the case when $k \sim k_o$. The threshold given by Rosenbluth (8.4) for the two plasmon decay instability used the restriction $k >> k_o$. Without this restriction, Barr uses the following threshold expression in his calculations:

$$\frac{1}{44} \left(\frac{v_e}{v_{th}} \right)^2 k_o L > 1 \qquad \text{VIII - 7}$$

The corresponding irradiance Φ is given by:

$$\Phi > 2.3 \times 10^{16} T_e/L \text{ W cm}^{-2} \qquad \text{VIII - 8}$$

Where T_e is in keV and L in μm

From equation II - 24, the dispersion relations for the incident wave at ω_o and the scattered wave at $\omega_{3/2}$ are given by:

$$\omega_o^2 = \omega_p^2 + k_o^2 c^2 \qquad \text{VIII - 9}$$

$$\omega_{3/2}^2 = \omega_p^2 + k_{3/2}^2 c^2 \qquad \text{VIII - 10}$$

At the quarter critical surface $\omega_p = \omega_o/2$. Hence, equation VIII - 9 gives:

$$\omega_o = (\frac{4}{3})^{1/2} k_o c \qquad \text{VIII - 11}$$

substituting VIII - 11 into VIII -10 gives:

$$k_{3/2} = k_o (\frac{8}{3})^{1/2} \qquad \text{VIII - 12}$$

If sufficiently above threshold, the spectrum will be broad. The $3\omega_o/2$ emission can arise in four ways - the mixing of a plasmon with:

i) a pump photon, or

ii) a specularly reflected photon, or

iii) a Brillouin scattered photon,

or iv) the mixing of three plasmons.

The frequency shifts due to the Bohm-Gross dispersion relation for the plasmons have been calculated by Barr for each of the above cases.

i) Ingoing pump photon + plasmon

k, k_o and $k_{3/2}$ are the wavenumbers of the plasmon, incident photon and the scattered photon respectively.

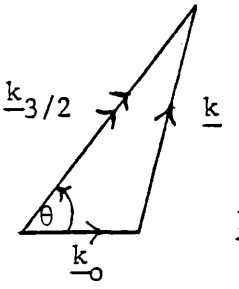

Fig. 8.1

Resolving the scattered wave into components along the z direction:

$$k_x = k_{3/2} \cos\theta + k_z \qquad \text{where } k_z = \underline{k}_o + k_B$$

$$k_y = k_{3/2} \sin\theta$$

From the Bohm-Gross dispersion relation, the frequency shift is given by:

$$\Delta\omega_{3/2} = \frac{3\, k_o\, k_B\, v_{th}^2}{\omega_o}$$

$$= 3\,\frac{k_o}{\omega_o}\,\left(k_{3/2} \cos\theta - \frac{3}{2} k_o \right) v_{th}^2$$

since $k_{3/2} = k_o \left(\frac{8}{3} \right)^{1/2}$

$$\frac{\Delta\omega_{3/2}}{\omega_o} = \frac{9}{4}\,\frac{v_{th}^2}{c^2}\,\left\{ \left(\frac{8}{3} \right)^{1/2} \cos\theta - \frac{3}{2} \right\}$$

Therefore,

$$\Delta\lambda_{3/2} = -\ 33.8\ (\cos\theta - 0.92)\ T_e \quad \text{Å} \qquad \text{VIII - 13}$$

From Liu and Rosenbluth (8.4) the maximum growth rate for the plasmon is given by:

$$k_B^2 = \frac{k_o}{4}^2 + k_y^2 \rightarrow \left(k_{3/2} \cos\theta - \frac{3}{2} k_o \right)^2 = \frac{k_o^2}{4} + k_{3/2}^2 \sin^2\theta$$

Thus, solving for cos θ

$$\cos\theta = -\ 0.12 \text{ or } \theta = 97^o$$

Therefore, this generation mechanism only gives a red-shifted component where:

$$\underline{\Delta\lambda_{3/2} \sim -\ 35\ T_e \quad \text{Å}} \qquad \text{VIII - 14}$$

ii) Specularly reflected pump photon + plasmon

Similarly,

$$k_{3/2} \cos\theta = k_z - k_o$$

$$k_{3/2} \sin\theta = k_y$$

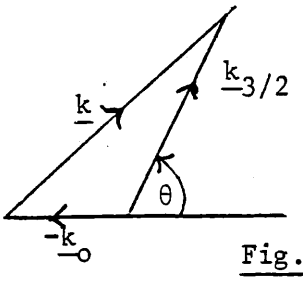

Fig. 8.2

The frequency shift is given by:

$$\frac{\Delta\omega_{3/2}}{\omega_o} = \frac{9}{4} \left(\frac{v}{c}th\right)^2 \left\{ \left(\frac{8}{3}\right)^{1/2} \cos\theta + \frac{1}{2} \right\}$$

Therefore,

$$\Delta\lambda_{3/2} = - 33.8 \left(\cos\theta + 0.31 \right) T_e \quad \text{Å}$$

The maximum growth rate condition for the plasmon gives:

$$\cos\theta = 0.8766 \text{ or } 0.5709$$

Therefore,

$$\theta = 151^o \text{ or } 55^o$$

$$\Delta\lambda_{3/2} = 19\ T_e \text{ Å or } - 29.8\ T_e \text{ Å}$$

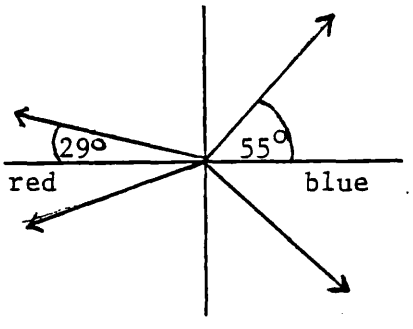

Fig. 8.3

This generation mechanism gives two components, where the blue-shifted component is forward scattered to be reflected at the 9 $n_{CR}/4$ surface and is only observed in the backscatter direction if this surface is present.

iii) Brillouin Scattered Pump + Plasmon

This process requires a significant amount of Brillouin scattering to occur in the region $n_e \gtrsim n_{CR}/4$. The frequency shift is given by:

$$\frac{\Delta\omega_{3/2}}{\omega_o} = \omega_o - \omega_{ia} + \frac{\omega}{2}o + \frac{3\, k_o\, k_B\, v_{th}^2}{\omega_o} \qquad \text{VIII - 16}$$

The additional frequency shift due to the Brillouin component is:

$$\frac{\Delta\omega}{\omega_o}B = \frac{2\, k_o\, c_s}{\omega_o} = 1.77 \times 10^{-3} \left(\frac{Z\, T}{A} e \right)^{1/2}$$

where c_s is the ion sound velocity and A is the atomic weight of the target.

$$\Delta\lambda_B = + 8.3 \left(\frac{Z\, T}{A} e\right)^{1/2} \quad \text{Å} \qquad \text{VIII - 17}$$

So, the Brillouin component gives a small additional shift in frequency to the red compared with case ii)

iv) Coalescence of Three Plasmons

Similarly,

$$\omega_{3/2} = \sum_{i=1}^{3} \omega_i$$

$$= \frac{3}{2}\omega_o + \left(\sum_{i=1}^{3} k_i \right) \frac{3\, k_o\, v_{th}^2}{\omega_o}$$

where $k_{3/2} \cos\theta = \sum_i k_{iz} = \frac{3}{2} k_o + \sum_i k_i \hat{i}\, \hat{k}_i = k_{3/2} \cos\theta - \frac{3}{2} k_o$

$$k_{3/2} \sin\theta = \sum_i k_{iy}$$

Therefore,

$$\Delta\lambda_{3/2} = - 33.8 \left(\cos\theta - 0.92 \right) T_e \quad \text{Å} \qquad \text{VIII - 18}$$

This generation mechanism gives the same asymmetric spectrum (red-shifted component only) as in case i).

v) Summary

The Barr model (like the Avrov model) predicts the frequency shift is proportional to T_e . Additional shifts due to Brillouin scattering or expansion of the plasma are small and proportional to $T_e^{1/2}$.

8.5 Review of Experimental Evidence for $3\omega_o/2$ Harmonic Emission

Time integrated studies of $3\omega_o/2$ harmonic emission have been reported from various targets irradiated by Nd/glass laser pulses.

Observations in a direction of 45^o from the incident beam axis were reported by Bobin et al (8.7) of an asymmetric $3\omega_o/2$ spectrum, with broadening occurring only towards the lower frequencies.

Sigel et al (8.8) investigated backscattered $3\omega_o/2$ harmonic emission from various plane targets and found the spectrum consisted of a doublet, with the blue-shifted component ($\Delta\lambda_b \sim -10$ Å) being of lower intensity than the red-shifted one ($\Delta\lambda_r \sim +10$ to 40 Å). They also determined the threshold for the onset of the $3\omega_o/2$ harmonic emission to be 2×10^{13} W cm^{-2} and from side-on photographs, concluded it was generated at the quarter critical surface.

Avrov et al (8.5) used the nine beam Kalmer laser system at a mean flux of $\Phi = 10^{14}$ W cm^{-2} on solid glass microspheres to study the forward and backscattered $3\omega_o/2$ harmonic emission. In both directions, a $3\omega_o/2$ spectrum with a doublet structure was observed. The red-shifted component ($\Delta\lambda_r \sim 15$ to 32 Å) was more intense than the blue-shifted component ($\Delta\lambda_b \sim 7$ to 13 Å). The minimum between the two peaks corresponded to the exact value of $3\omega_o/2$ to within 2 to 3 Å .

Carter et al (8.9) have obtained backscattered $3\omega_o/2$ spectra which show a double peaked structure, where the two components are shifted symmetrically from the nominal position of $3\omega_o/2$. Raven (8.10) has

obtained spatially resolved side on images which show the $3\omega_o/2$ harmonic emission occurring from localised spots of very high intensity and size less than the resolution of the optics (i.e. < 5 μm).

There have also been time-resolved studies of the $3\omega_o/2$ harmonic emission. Jackel et al (8.1) streaked the $2\omega_o$ and $3\omega_o/2$ harmonic emissions simultaneously as reported in Section 7.6 to obtain a measurement of the density scale length. Leonard and Cover (8.2) streaked the sidescattered $3\omega_o/2$ harmonic emission from microballoon targets to monitor the expansion of the $n_{CR}/4$ surface. They noticed pulsing of short duration ($\lesssim$ 5 ps) in the harmonic intensity which was uncorrelated with the temporal structure in the incident pulse. This they attribute to quarter critical density surface modulations as predicted by the simulations of Lasinski et al (8.11).

Bychenkov et al (8.3) have streaked the $3\omega_o/2$ harmonic spectra from glass and aluminium microspheres. They used a long pulse ($\sim$ 5 ns) and their temporal resolution was $\sim$ 100 ps. No temporal structure uncorrelated with the intensity of the incident pulse was observed, but the separation of the two peaks was found to vary by up to 30% during the pulse length.

8.6 Experimental Method

In the present investigation, an experiment was performed to study the evolution of the $3\omega_o/2$ harmonic spectrum from laser irradiated microballoons. This work differs from previous investigations (8.3) by virtue of the high temporal resolution ($\sim$ 10 ps) simultaneous with a spectral resolution of $\sim$ 30 Å. The Nd/glass laser facility provided an irradiance of 2×10^{16} W cm^{-2} in a 100 ps pulse on glass microballoon targets of 50 - 90 μm diameter.

The experimental layout is shown in Fig 8.5 and is similar to those described in the two preceding Chapters. The backscattered $3\omega_o/2$ radiation was collected by the f/1 doublet lens used to focus the laser light on the target. This lens produced a 60 x magnified image at $3\omega_o/2$

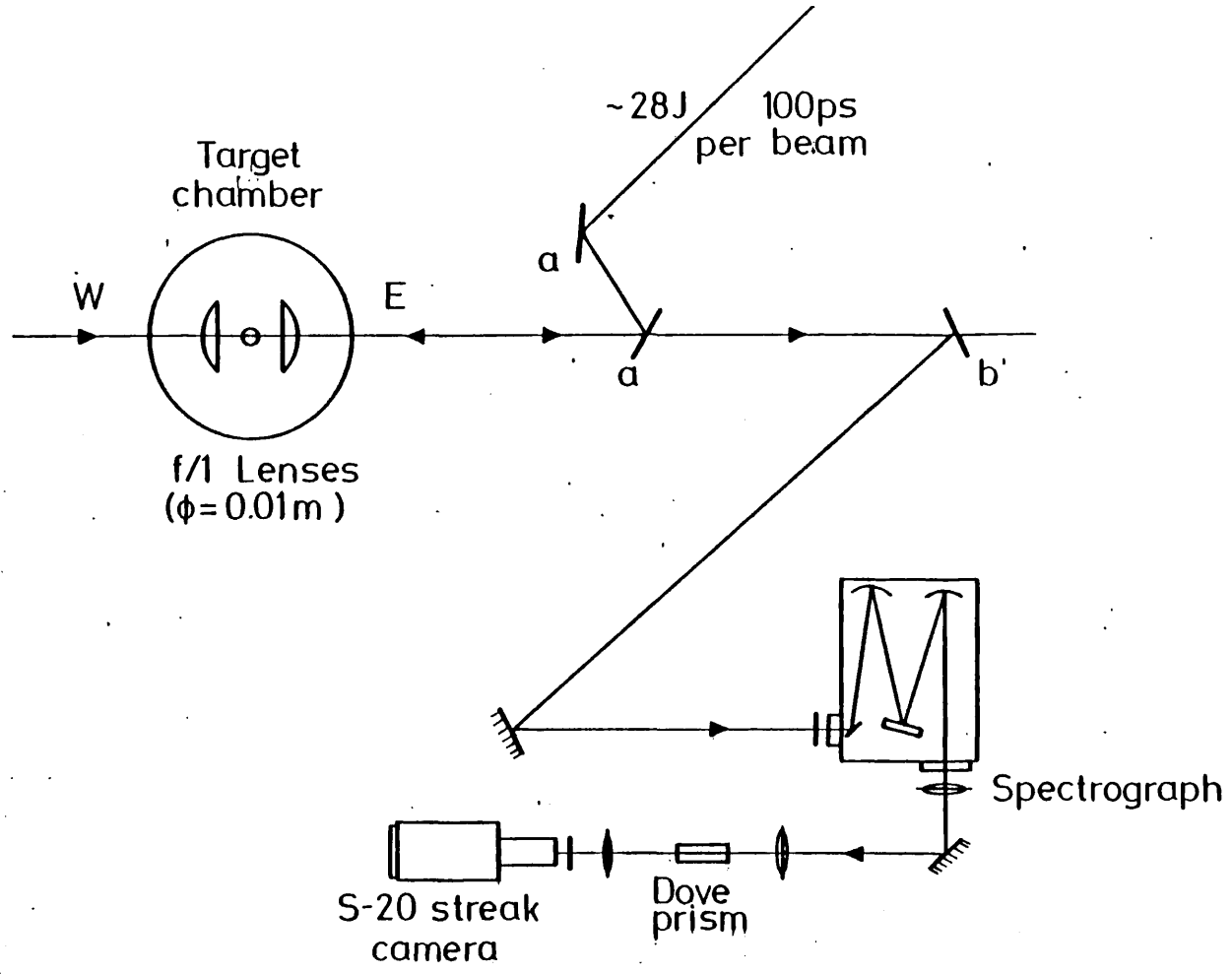

FIG. 8.5 - Experimental layout for $3\omega_o/2$ time resolved spectroscopy.

on the slit of the 0.5 m, 600 line mm^{-1} grating spectrograph. The slit width restricted the spectral resolution to $\sim$ 30 Å . The output plane of the spectrograph was optically coupled to the Hadland Photonics streak camera fitted with an S-20 photocathode. A dove prism rotated the image so that wavelength would be dispersed along the direction of the streak camera slit. The time resolution of the whole system was limited by the temporal dispersion of the spectrograph grating to $\sim$ 10 ps. The spectrograph was also used in second order with corresponding temporal and spectral resolutions of $\sim$ 20 ps and $\sim$ 15 Å respectively.

Photographic recordings of the streak data were made on Kodak 2485 film (developed as for Chapter 6 and 7). Separate exposures of the 5461 Å Hg I line were taken with the spectrograph at different wavelength settings to calibrate both wavelength and dispersion.

8.7 Results

Examples of the time-resolved $3\omega_o/2$ harmonic emission spectra are shown in Fig. 8.6. The $3\omega_o/2$ emission has a pulsed nature where the duration of the pulses appear to be less then the temporal resolution limit set by the diagnostic system ($\sim$ 10 ps).

The blue-shifted and red-shifted components are generated simultaneously but with their wavelength separation varying in time. Spectra with monotonically decreasing wavelength separation (Fig. 8.6 a)) are obtained for low prepulse levels i.e. less than 10^{-5} times the main laser pulse energy. However, spectra showing an increasing then decreasing wavelength separation (Fig. 8.6 b)) occur as a result of larger prepulse levels. The blue-shifted component appears more intense than the red-shifted one which is the reverse of the time integrated observations reported earlier (8.9). This is probably due to the spectral sensitivity of the S-20 photocathode falling off rapidly in the red near 7093 Å and may be accentuated by any error between the direction of the spectral dispersion and the streak camera slit.

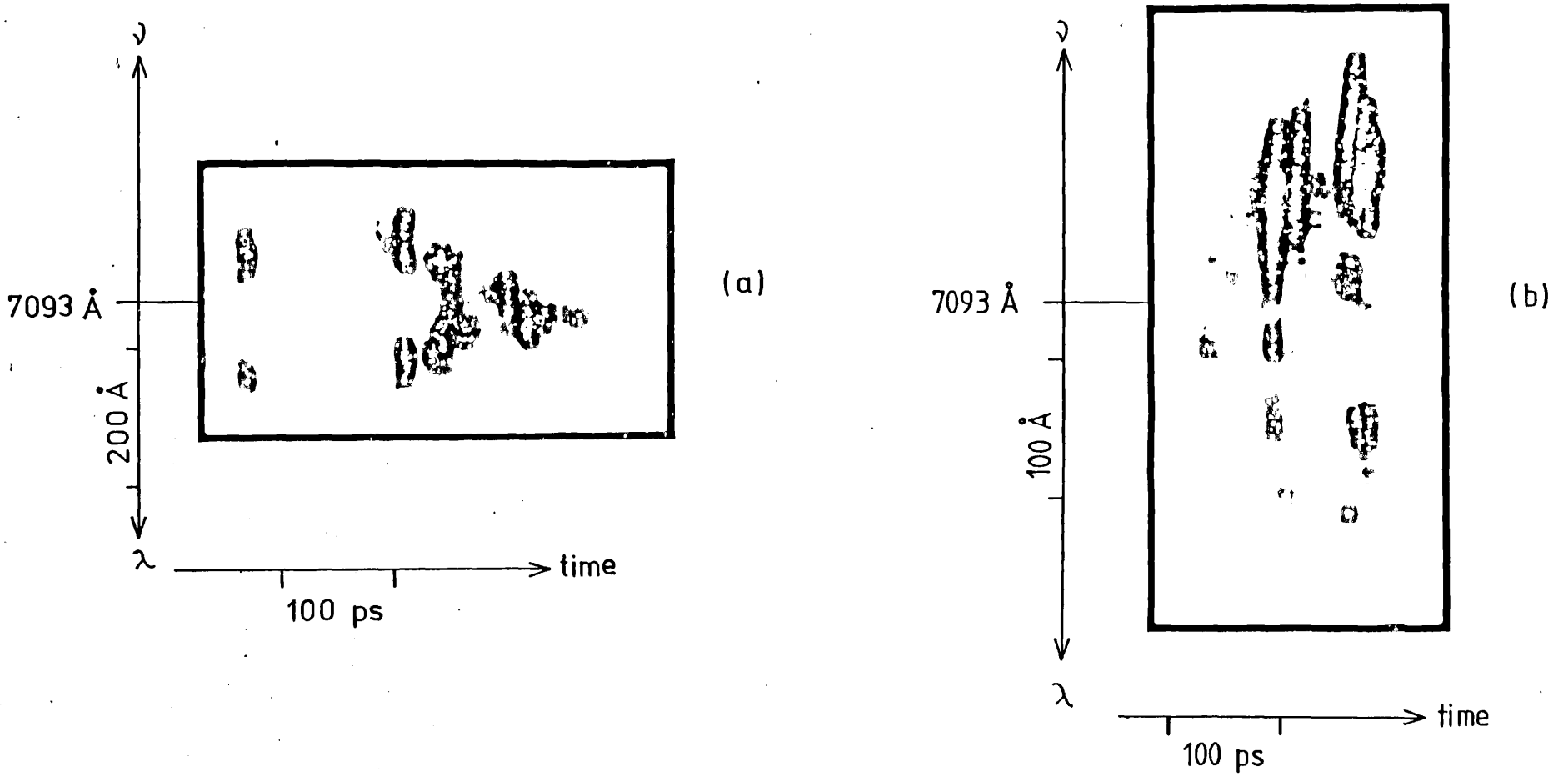

FIG. 8.6 - Examples of time resolved $3\omega_o/2$ spectra. a) No prepulse: decreasing separation in time between peaks; temporal resolution ∿10 ps, spectral resolution ∿30 Å b) With prepulse: increasing, then decreasing separation in time between peaks; temporal resolution ∿ 20 ps, spectral resolution ∿ 15 Å.

8.8 Discussion

The difference between the spectra of Figs. 8.6 (a) and 8.6 (b) may be explained by the results of the Barr theory (the Avrov theory is not applicable since $k \sim k_o$ in the present experiment).

The Barr theory considers the dominant mechanism for the production of $\omega_o/2$ plasmons to be the two plasmon decay since its threshold in an inhomogenous plasma is lower than that for stimulated Raman scattering. In the case of a small laser prepulse i.e. Fig. 8.6 (a), the density scalelength during the rising half of the laser pulse is very small and the threshold for the two plasmon decay instability is only exceeded after the peak of the laser pulse as the density scale length increases. The decreasing separation of the red and blue peaks is then a reflection of the decreasing electron temperature during the falling part of the laser pulse (8.12). With a significant prepulse ($> 10^{-5}$ times the main incident pulse energy), the initial density scale lengths during the main pulse are longer and the threshold for the instability exceeded earlier. The spectral separation then follows the rise and fall of the electron temperature with the laser irradiance.

The spectra obtained experimentally show a symmetrical shift of the red and blue wings. The discrepancy between this and the Barr theory may be due to rippling (8.11) of either the critical or quarter critical density surfaces giving rise to an uncertainty in the angular relationship of the plasma waves and electromagnetic waves. Also the Barr theory assumes that the nine-fourths critical density layer is parallel to the quarter critical surface and this may not be the case.

The pulsed nature of the $3\omega_o/2$ harmonic emission may be due to density profile modification of the quarter critical density surface due to the ponderomotive force of the plasma waves. This has been predicted by plasma simulations (8.11) and observed by interferometry (8.13). The saturation of the two plasmon decay instability by profile steepening and by driven ion waves and its subsequent recurrence has been observed in simulations by

Langdon et al (8.14), who indicated that there would be corresponding bursts of $3\omega_o/2$ harmonic emission. However, the simulations show that saturation by driven ion waves has too short a relaxation time (less than 1 ps), while the longer timescale associated with saturation due to profile steepening is not given for realistic electron-ion mass ratios.

Similar behaviour in the nature of the $2\omega_o$ harmonic emission (see Chapter 7) indicate that a hydrodynamic instability is responsible. The timescale for such an instability was calculated in section 7.7 Chapter 7 to be $\sim$ 15 ps which is of the order of the observations of the pulsed $3\omega_o/2$ emission.

8.9 Estimation of the Electron Temperature (T_e) in the Underdense Plasma

The experimental observations described in section 8.7 indicate that the separation of the blue-shifted and red-shifted peaks in the $3\omega_o/2$ harmonic spectrum is related to the electron temperature, T_e , in the underdense plasma.

If only the fastest growing mode of the plasma wave is considered, the Barr model shows the dominant contribution to the spectrum of the $3\omega_o/2$ harmonic emission backscattered through the f/1 lens, arises from the combination of the reflected pump and plasma waves. The shifts due to Brillouin and Doppler effects are negligible compared with the observed shifts of the $3\omega_o/2$ radiation i.e. 10-20 Å compared with observed shifts of 50-200 Å. Moreover, the Brillouin shift is reduced to zero if the expansion of the plasma is at the sound speed.

For the narrow range of irradiances $\sim 10^{16}$ W cm^{-2} employed in these observations the typical separation of blue-shifted and red-shifted peaks is $\sim$ 150 Å. From equation VIII - 15:

$$\Delta\lambda_r + \Delta\lambda_b \sim 50\ T_e\ \text{Å}$$

where T_e is in keV

giving $T_e \sim 3$ keV. This is a reasonable value compared with estimates of T_e from x-ray diode measurements taken with similar laser parameters (8.15).

CHAPTER 9

General Conclusion

9.1 Conclusions

At the start of the work reported in this thesis, much information had been derived by other workers from studying the scattered light spectrum for non-linear interactions between the intense laser radiation and the plasma. However, most of these previous studies were time-integrated and it was hoped that by employing high temporal resolution (of the order of picoseconds) new observations would be obtained.

A streak camera coupled to the output of a spectrograph was chosen as a suitable high speed spectroscopic diagnostic despite the limited dynamic range possessed by streak cameras, in general, for picosecond operation. The reasons for the poor dynamic range performance were investigated and it was concluded that space charge effects in the region where the electron trajectories cross-over were not significant factors. This conclusion has been confirmed elsewhere (9.1 - 9.2). Subsequent calibration measurements of the streak cameras used for these experiments showed they possessed adequate dynamic range ($\sim$ 10-15) to study the evolution of the scattered light spectrum.

Backscattered light at the fundamental frequency ω_o was observed which displayed the characteristic red shift of Brillouin scattering. Unlike previous reports (9.3 - 9.4) no saturation level in the backscatter energies was observed, even for an irradiance of $\sim 10^{15}$ W cm^{-2} . Analysis of a shot where the laser was mode beating revealed levels of $\sim$ 100% backscatter for scale lengths of $\gtrsim$ 160 μm. Hence, the stimulated Brillouin scattering instability poses a serious problem for 1.06 μm laser light coupling with plasmas.

At irradiances greater than 10^{15} W cm^{-2} , an asymmetric $2\omega_o$ spectrum was observed, broadened to the lower frequencies only. Although this

observation agrees with previous reports (9.5), the interpretation of the broadened $2\omega_o$ spectrum differs from previous explanations which attribute the broadening to the presence of the parametric decay instability. Instead, the generation mechanism for the ω_o plasmons is ascribed to resonance absorption. The present results can be explained by the model suggested by Cairns (9.6) that ion acoustic turbulence can induce a broadening of the plasma wave spectrum with a corresponding broadening of the $2\omega_o$ spectrum.

The observation of a double-peaked $3\omega_o/2$ harmonic spectrum was in agreement with previous reports (9.5). The frequency separation of the peaks varied during the incident pulse length in a manner consistent with theories suggesting that the frequency separation between the blue-shifted and red-shifted components is proportional to the electron temperature in the underdense plasma. None of the existing theoretical models exactly fits the experimental observations, but the Barr model which predicts the most similar spectrum to that observed gives a reasonable estimate for T_e i.e. $\sim$ 3 keV.

The high temporal resolution showed that both the $2\omega_o$ and $3\omega_o/2$ harmonic emissions display pulsations on a picosecond timescale, which suggest a hydrodynamic instability exists, possibly caused by an unstable ablation flow across a steepened density gradient.

9.2 Proposals for Future Work

As a result of the studies of the high speed streak camera, it is apparent that it would be a more versatile instrument if the dynamic range were greater. One method of extending the range would be to reduce the magnification of the electron optics; enabling higher photocurrents to be drawn before saturation.

The investigations of the backscattered light spectrum can be extended by doubling or trebling the frequency of the Nd/glass laser (by using a suitable crystal) to obtain shorter wavelengths i.e. visible and

uv. A wavelength scaling factor could then be obtained for the scattering processes e.g. the Brillouin instability, and other harmonics may be studied. For example, with a frequency trebled Nd/glass laser the frequency of the $\omega_o/2$ harmonic emission is $\sim$ 0.7 μm, which is in the easily detectable visible range and also cannot be confused with unconverted laser light.

All the investigations reported here could be repeated with a wider range of target materials. This is particularly relevant to the observations of the $3\omega_o/2$ spectrum which could provide a valuable diagnostic for the electron temperature in the underdense plasma near the quarter critical density surface.

Chapter 1 References

1.1 J. Nuckolls, L. Wood, A. Thiessen and G. Zimmerman
Nature Vol. 239, p 139. (1972)

1.2 A.F. Gibson
Phys. Techno. Vol. 9, p 72. (1978)

1.3 N.G. Basov and O.N. Krohkin
3rd Quant. Electronics Conf. Paris 1963 ed N. Bloembergen and P. Grivet. Columbia University Press N.Y. (1964)

1.4 J.D. Lawson
Proc. Phys. Soc. (Lond) B70, 6 (1957)

1.5 V.L. Ginzburg
Propagation of Electromagnetic Waves in Plasma. Pergamon Press Oxford. (1974)

1.6 T.P. Hughes
Laser Light and Plasmas. Adam Hilger London (1975)

1.7 C.S. Liu, M.N. Rosenbluth and R.B. White
Phys. Fluids 17, 1211 (1974)

1.8 E.A. Jackson
Phys.Rev. 153, 235 (1965)

C.S. Liu and M.N. Rosenbluth
Phys. Fluids 19, 967 (1976)

1.9 K. Nishikawa
J. Phys. Soc. Jap. 24, 916 and 1152 (1968)

1.10 T. Leonard, G. Charatis, M. Gredell and J. Ash
SPIE Vol 97 High Speed Photography. Toronto (1976)

1.11 D.J. Bradley and W. Sibbett
Appl. Phys. Lett. 27, 383 (1975)

1.12 R.A. Haas, W.C. Mead, W.L. Kruer, D.W. Phillion, H.N. Kornblum, J.D. Lindl, D. MacQuigg, V.C. Rupert and K.G. Tirsell
Phys. Fluids 20, 322 (1977)

1.13 J.L. Bobin, M. Decroisette, B. Meyer and Y. Vitel
Phys. Rev. Lett. 30, 594 (1973)

1.14 R. Sigel, K. Eidmann, H.C. Pant and P. Sachsenmaier
Phys. Rev. Lett. 36, 1369 (1976)

1.15 Section 1. Annual Report to the Laser Facility Committee 1978
Laser Division. Report No. RL-78-039. Rutherford Laboratory

1.16 Section 1. Annual Report to the Laser Facility Committee 1979
Laser Division. Report No. RL-79-036. Rutherford Laboratory

Chapter 2 References

2.1 N.A. Krall and A.W. Trivelpiece Principles of Plasma Physics
McGraw-Hill U.S.A. (1973)

2.2 T.P. Hughes Plasmas and Laser Light

2.3 D. Bohm and E.P. Gross
Phys. Rev. 75, 1851 (1949)

2.4 T.P. Hughes. An Introduction to the Absorption of Laser Light in Plasmas. Laser Plasma Interactions SUSSP (1979)

2.5 W.L. Kruer Theory and Simulation of Laser Plasma Coupling
Laser Plasma Interactions SUSSP (1979)

Chapter 3 References

3.1 F.F. Chen Laser Interaction and Related Plasma Phenomena
3, 291 Plenum N.Y. (1974)

3.2 K. Nishikawa
J. Phys. Soc. Jap. 24, 916 (1968)

K. Nishikawa
J. Phys. Soc. Jap. 24, 1152 (1968)

3.3 F.W. Perkins and J. Flick
Phys. Fluids 14, 2012 (1971)

3.4 R.N. Franklin, S.M. Hamberger, G. Lampis and G.J. Smith
Phys. Rev. Lett. 27, 1119 (1971)

3.5 J.L. Bobin, M. Decroisette, B. Meyer and Y. Vitel
Phys. Rev. Lett. 30, 594 (1973)

3.6 E.A. Jackson
Phys. Rev. 153, 235 (1967)

Y.C. Lee and P.K. Kaw
Phys. Rev. Lett 32, 135 (1974)

H.H. Chen and Liu
Phys. Rev. Lett 39, 881 (1974)

3.7 C.S. Liu and M.N. Rosenbluth
Phys. Fluids 19, 967 (1976)

3.8 P.D. Carter, S.M.L. Sim, H.C. Barr and R.G. Evans
Phys. Rev. Lett. 44, 1407 (1980)

3.9 A.B. Langdon, B.F. Lasinski and W.L. Kruer
Phys. Rev. Lett. 43, 133 (1979)

3.10 H.A. Baldis
10th Annual Anomalous Absorption Conference. San Fransicso 1980

3.11 W.L. Kruer
Comments Plasma Phys. 3, 129 (1978)

3.12 J.S. Pearlman and M.K. Matzen
Phys. Rev. Lett. 39, 140 (1977)

J.E. Balmer and T.P. Donaldson
Phys. Rev. Lett. 34, 312 (1975)

R.P. Godwin, R. Sachsenmaier and R. Sigel
Phys. Rev. Lett. 39, 1198 (1977)

3.13 K. Manes, V.C. Rupert, J.M. Auerbach, P. Lee and J.E. Swain
Phys. Rev. Lett. 39, 281 (1977)

3.14 R.A. Cairns
Plasma Phys. 20, 991 (1978)

3.15 C.S. Liu, M.N. Rosenbluth and R.B. White
Phys. Fluids 17, 1211 (1974)

3.16 R.G. Evans
Section 3.4.2. Annual Report to the Laser Facility Committee 1980
Report No. RL-80-026. Rutherford Laboratory

3.17 W.L. Kruer, K. Estabrook, B.F. Lasinski and A.B. Langdon
Phys. Fluids 23, 1326 (1980)

3.18 D.W. Phillion
UCRL - 84148 preprint

3.19 J. Elazar, W.T. Toner and E.R. Wooding
Plasma Physics 23, 813 (1981)

3.20 W.L. Kruer Theory and Simulation of Laser Plasma Coupling Laser Plasma Interactions. SUSSP (1979)

3.21 A. Raven
Section 3.2. Annual Report to the Laser Facility Committee 1978
Report No. RL-78-039. Rutherford Laboratory

3.22 T.P. Hughes An Introduction to the Absorption of Laser Light in Plasma Laser Plasma Interactions SUSSP (1979)

Chapter 4 References

4.1 H.P. Weber
J. Appl. Phys. 38, 2231 (1967)

E.P. Ippen, C.V. Shank and A. Diennes
Appl. Phys. Lett. 17, 1725 (1966)

4.2 R.C. Eckhardth and C.H. Lee
Appl. Phys. Lett. 15, 425 (1969)

C.C. Wang and E.L. Baardsen
Appl. Phys. Lett. 15, 396 (1969)

4.3 D.J. Bradley, G.H. New and S.J. Caughey
Phys. Lett. 30A, 78 (1969)

4.4 P.M. Rentzepis, C.H. Mitschele and A.C. Saxman
Appl. Phys. Lett. 17, 122 (1970)

4.5 D.H. Auston
Appl. Phys. Lett. 18, 249 (1971)

4.6 G. Mayer and F. Gires
Compt. Rad. Acad. Sci. (Paris) 258, 2039 (1964)

4.7 S.L. Shapiro and M.A. Duguay
Phys. Lett. 28A, 698 (1969)

4.8 M.A. Duguay and J.W. Hansen
Opt. Comm. 1, 254 (1969)

4.9 Data Sheet Spectra Physics Model 403B Photodiode

4.10 J.S. Courtney-Pratt
Research Suppl. 2, 267 (1949)
Proc. Roy. Soc. A204, 27 (1950)

4.11 Proc. of 11th Int. Cong. High Speed Photog.
ed. P.J. Rolls, pub. Chapman and Hall. London (1974)
pp 32, 101, 107, 112, 118, 124, 130, 136

4.12 D.J. Bradley and W. Sibbett
Appl. Phys. Lett. 27, 383 (1975)

4.13 E.K. Zavoiskii and S.D. Fanchenko
Appl. Opt. 4, 1135 (1965)

4.14 M. Ya Schelev, M.C. Richardson and A.J. Alcock
Rev. Sci. Inst. 43, 1819 (1972)

4.15 N. Ahmed, B.C. Gale and M.H. Key
Adv. in Elec. and Elec. Phys. 28B, 999 (1969)

4.16 W. Friedman, S. Jackel, W. Seka and F.J. Zimmerman
Proc. 12th Int. Cong. High Speed Photog. Toronto (1976)

4.17 D.J. Bradley, S.F. Bryant, J.R. Taylor and W. Sibbett
Rev. of Sci. Instrum. 49, 219 (1978)

4.18 S. Majumder
To be published

4.19 R. Kalibjian
J. Appl. Phys. 46, 4875 (1975)

4.20 D.R. Hull and N.J. Freeman
J. Phys. E. Sci. Inst. 13, 685 (1980)

Chapter 5 References

5.1 P. Lee, D.V. Giovanelli, R.P. Godwin and G. McCall
Appl. Phys. Lett. 24, 406 (1974)

5.2 Dale Electronics Ltd. Data Sheet D3003 B-3

Chapter 6 References

6.1 R.A. Haas, W.C. Mead, W.L. Kruer, D.W. Phillion, H.N. Kornblum, J.D. Lindl, D. MacQuigg, V.C. Rupert and K.G. Tirsell
Phys. Fluids 20, 322 (1979)

6.2 M.D. Rosen D.W. Phillion, V.C. Rupert, W.C. Mead, W.L. Kruer, J.J. Thomson, H.N. Kornblum, V.W. Slivinsky, G.J. Caporaso, M.J. Boyle and K.G. Tirsell
Phys. Fluids 22, 2020 (1979)

6.3 B.H. Ripin and E.A. McLean
Appl. Phys. Lett. 34, 809 (1979)

6.4 L.M. Gorbunov, S. Yu Kas'yanov, V.V. Korohkin, A.N. Polyanichev and A.P. Shevel'ko
JETP Lett. 27, 227 (1979)

6.5 A. Ng, L. Pitt, D. Salzmann and A.A. Offenberger
Phys. Rev. Lett. 42, 307 (1979)

6.6 A. Ng, A.A. Offenberger and S.J. Karttunen
Opt. Comm. 36, 200 (1981)

6.7 D.C. Slater, R.L. Berger, G. Busch, C.M. Kinzer, F.J. Mayer, L.V. Powers and D.J. Tanner
KMJ-U-950 (1980)

6.8 H. Azechi et al
Paper IAEA - CN-37-19-4
Conf. on Plasma Phys. and Controlled Nuclear Fusion Research
Innsbruck. Aug. 1978

6.9 R.E. Turner and L.M. Goldman
Rhys. Fluids 24, 186 (1981)

6.10 W.L. Kruer, K. Estabrook, B.F. Lasinski and A.B. Langdon
Phys. Fluids 23, 1326 (1980)

6.11 M.K. Matzen and R.L. Morse
Phys. Fluids 22, 654 (1979)

6.12 W.L. Kruer
Phys. Fluids 23, 1273 (1980)

6.13 O. Willi
Private Communication

6.14 R.G. Evans
Section 3.4.2. Annual Report to the Laser Facility Committee 1980
Report No. RL-80-026. Rutherford Laboratory

6.15 B.H. Ripin, J.M. McMahon, E.A. McLean, W.M. Manheimer and J.A. Stamper
Phys. Rev. Lett. 33, 634 (1974)

Chapter 7 References

7.1 N.S. Erohkin, V.E. Zakhorov and S.S. Moiseev
Sov. Phys. JETP 29, 101 (1969)

7.2 N.S. Erohkin, S.S. Moiseev and V.V. Muhkin
Nucl. Fusion 14, 333 (1974)

7.3 G.J. Vinogradov and V.V. Pustavalav
Sov. Phys. JETP 36, 492 (1973)

7.4 O.N. Krohkin, V.V. Pustovalov, A.A. Rupasov, V.P. Silin, G.V. Sklizkov, A.N. Starodub, V.P. Tikhonchuk and A.S. Shikanov
JETP Lett. 22, 21 (1975)

7.5 V.L. Ginzburg
Propagation of Electromagnetic Waves in Plasma
Pergamon Press Oxford (1974)

7.6 R.A. Cairns
J. Plasma Phys. 22, 149 (1979)

7.7 W.M. Manheimer and H.H. Klein
Phys. Fluids 18, 1299 (1975)

7.8 P.D. Carter, E. Fabrikesi, T.A. Hall, T.P. Hughes and M.S. White
Section 2.3. Annual Report to the Laser Facility Committee 1978
Report No. RL-78-039. Rutherford Laboratory

7.9 N.G. Basov, O.N. Krohkin, V.V. Pustovalov, A.A. Rupasov, V.P. Silin G.V. Sklizkov, V.T. Tikhonchuk and A.S. Shikanov
Sov. Phys. JETP 40, 61 (1974)

7.10 L.M. Goldman, J. Soures and M.J. Lubin
Phys. Rev. Lett. 31, 1184 (1973)

7.11 E. Fabre, C. Garban, C. Popovics, A. Porquerusse, C. Stenz and J. Virmont
Opt. Comm. 18, 218 (1976)

7.12 K. Eidmann and R. Sigel
Phys. Rev. Lett. 34, 799 (1975)

7.13 V.V. Aleksandrov, V.D. Vikharev, V.P. Zorov, N.G. Koval'skii and M.I. Pergament
JETP Lett. 24, 508 (1977)

7.14 J.L. Bobin, M. Decroisette, B. Meyer and Y. Vitel
Phys. Rev. Lett. 30, 594 (1973)

7.15 M. Decroisette, B. Meyer and Y. Vitel
Phys. Lett. 45A, 443 (1973)

7.16 S. Jackel, B. Perry and M. Lubin
Phys. Rev. Lett. 37, 95 (1975)

7.17 V. Yu Bychenkov, Yu A. Zakharenkov, O.N. Krohkin, A.A. Rupasov, V.P. Silin, G.V. Sklizkov, A.N. Starodub, V.T. Tikhonchuk and A.S. Shikanov
JETP Lett. 26, 364 (1977)

7.18 S. Jackel, J. Albritton and E. Goldman
Phys. Rev. Lett. 35, 514 (1975)

7.19 A. Saleres, M. Decroisette and C. Patou
Opt. Comm. 13, 321 (1975)

7.20 N.G. Basov, V. Yu Bychenkov, O.N. Krohkin, M.V. Osipov, A.A. Rupasov, V.P. Silin, G.V. Sklizkov, A.N. Starodub, V.T.Tikhonchuk and A.S. Shikanov
Sov. J. Quantum Electron. 9, 1081 (1979)

7.21 A. Raven and O. Willi
Phys Rev. Lett. 43, 278 (1979)

7.22 R.A. Cairns
Plasma Phys. 20, 991 (1978)

7.23 C. Max and C.F. McKee
Phys. Rev. Lett. 39, 1336 (1977)

7.24 K. Manes, V.C. Rupert, J.M. Auerbach, P. Lee and J.E. Swain
Phys Rev. Lett 39, 281 (1977)

7.25 A. Maaswinkel
Opt. Comm. 35, 236 (1980)

7.26 G. Auer, K. Sauer and K. Baumgärtel
Phys. Rev. Lett. 42, 1744 (1979)

Chapter 8 References

8.1 S. Jackel, J. Albritton and E. Goldman
Phys. Rev. Lett. 35, 514 (1975)

8.2 T.A. Leonard and R.A. Cover
J. Appl. Phys. 50, 3241 (1979)

8.3 V. Yu Bychenkov et al
JETP Lett. 26, 364 (1977)

8.4 C.S. Liu, M.N. Rosenbluth and R.B. White
Phys. Fluids 17, 1211 (1974)

8.5 A.I. Avrov, V. Yu Bychenkov, O.N. Krohkin, V.V. Pustovalov, A.A. Rupasov, V.P. Silin, G.V. Sklizkov, V.T. Tikhonchuk and A.S. Shikanov
Sov. Phys. JETP 43, 507 (1977)

8.6 H.C. Barr
Unpublished

8.7 J.L. Bobin, M. Decroisette, B. Meyer and Y. Vitel
Phys. Rev. Lett. 30, 594 (1973)

8.8 R. Sigel, K. Eidmann, H.C. Pant and P. Sachsenmaier
Phys. Rev. Lett. 36, 1369 (1969)

8.9 P.D. Carter, E. Fabrikesi, T.A. Hall, T.P. Hughes and M.S. White
Section 2.3. Annual Report to the Laser Facility Committee 1978
Report No. RL-78-039. Rutherford Laboratory

8.10 A. Raven
Section 3.2. Annual Report to the Laser Facility Committee 1978
Report No. RL-78-039. Rutherford Laboratory

8.11 A.B. Langdon and B.F. Lasinski
UCRL 50021-75, p. 309 (1976)

8.12 C. McClellan, P.H.Y. Lee and G. Caporaso
Phys. Rev. Lett. 44, 658 (1980)

8.13 H.A. Baldis, J.C. Sampson and P.B. Corkum
Phys. Rev. Lett. 41, 718 (1978)

8.14 A.B. Langdon, B.F. Lasinski and W.L. Kruer
Phys. Rev. Lett. 43, 133 (1979)

8.15 A. Pugatschew
Private Communication

Chapter 9 References

9.1 R. Kalibjian
J. Appl. Phys. 46, 4875 (1975)

9.2 D.R. Hull and N.J. Freeman
J. Phys. E. Sci. Instrum. 13, 685 (1980)

9.3 A. Ng, A.A. Offenberger and S.J. Karttunen
Opt. Comm. 36, 200 (1981)

9.4 A. Ng, L. Pitt, D. Salzmann and A.A. Offenberger
Phys. Rev. Lett. 42, 307 (1979)

9.5 J.L. Bobin, M. Decroisette, B. Meyer and Y. Vitel
Phys. Rev. Lett. 30, (1973)

9.6. R.A. Cairns
J. Plasma Phys. 22, 149 (1979)

ACKNOWLEDGEMENTS

I would like to thank Dr. E.R. Wooding for continuing the excellent supervision of the late Dr. V.I. Little, whose untimely death was a tragic loss, but the memory of whom remained the inspiration for the completion of this work.

I am extremely grateful to P.D. Carter for his help with the time-resolved $2\omega_o$ and $3\omega_o/2$ harmonic emission studies; P.J. Dooley for his aid with the image-converter tubes experiment and A.J. Cole, D.R. Gray, J. Murdoch and W.T. Toner for their assistance with the Brillouin experiment. I am also grateful to Dr. R.G. Evans for his invaluable advice about the analysis of the Brillouin and harmonic emission data; Dr. H.C. Barr for helpful discussions about $3\omega_o/2$ harmonic generation; and Dr. S. Majumdar (image-converter tubes) and T.P. Hughes ($2\omega_o$ harmonic emission) for their advice and encouragement. Many thanks are due to all the staff at the SERC Laser Facility, Rutherford Laboratory for their excellent technical assistance.

Finally, I am indebted to Linda Beal for typing this thesis.

Financial support throughout this work was provided by a Postgraduate studentship from the Science and Engineering Research Council.

THE DYNAMIC RANGE OF FOUR IMAGE CONVERTER TUBES IN NANOSECOND AND SUBNANOSECOND PHOTOGRAPHY

P. Dooley, V. I. Little, S. Sim and S. Majumdar
Royal Holloway College
Surrey, England

Abstract

The relative importance of space charge inside an electrostatically focussed tube (i) near the photo-surface and (ii) at the electron trajectory cross-over point is evaluated by comparing the performance of four electrostatically focussed single stage image converter tubes. A 3 nanosecond long Nitrogen laser pulse was used for these experiments.

The electron optics of these tubes were sufficiently varied, so that a proper evaluation of photo-cathode surface resistance could also be carried out.

The results suggest that the most important area of space charge contribution for electron image degradation is the region near the photo-cathode. It was also observed that the degradation of spatial resolution, for an image tube with high photo-cathode conductivity and more than 2 KV/cm^2 electric field near the photo-cathode, was not significant until the photo-current density reached above 40 ma/cm^2. This current density is much greater than that normally available from picosecond streak tubes, if good time resolution is expected from these tubes.

In the light of these experiments, the importance of vacuum space charge in an image tube for picosecond time resolution is discussed.

Introduction

The current density requirements for recording subnanosecond events using image converter-instensifier systems can be defined by the following equation (Schelev et al, 1972)[1]

$$\frac{I\tau}{e} > \frac{\alpha\beta^2 S}{K\gamma\omega} \qquad (1)$$

where α = energy of protons/cm^2 on film
I = current density
τ = required time resolution
β = overall magnification
S = 1 cm^2 - area illuminated on the first photocathode.
K = overall amplification of output photon energy from the fast image converter.
γ = number of photons at the output phosphor of image converter per photo-electron.
ω = energy per photon emitted by first phosphor.

The same authors observed that for 1 picosecond time resolution using a single stage image converter camera, a current density of several hundred milliamperes per cm^2 is required even for a unity dynamic range recording of the event.

Several groups[2, 3, 4] have since reported ~2 picosecond time resolution using image intensifiers capable of detecting single photo-electrons to intensify the output from the high speed image converter tube. These systems showed very severe limitations to their useful dynamic range. The best reported dynamic range was that given by Thomas et al (1974)[5] (over a hundred dynamic range for 120 picosecond pulse).

Analyses of the reported systems (as far as practicable from the reports) suggest[6] that the maximum current density that has been extracted from the photocathode of the high speed image converter, for 1-5 picosecond time resolution (operated in the streak mode) is $\ll$ 1 mA/cm^2. At higher current densities, time resolution of the streak camera has been reported to become worse.

However, it has been known for a long time that photodiodes can be used with better than 0.5 nanosecond time resolution when handling current densities in excess of 1 A/cm^2 (for example, ITT photodiode type F4000 or I.T.L. photodiode type HD125), without losing linearity of response.

It has been suggested that the reason for nonlinear behaviour of picosecond streak

cameras at photocurrent densities above 100-300 $\mu A/cm^2$ could be due to:

(i) Space charge retardation of photoelectron velocity between the photocathode and the next electrode,
(ii) Space charge at the electron optical cross over point in the streak tubes (which are mostly electrostatically focussed).

Several authors have reported on the behaviour of tubes[5,6], at various current densities. And the results have shown the onset of such space charge induced loss of spatial resolution (and hence time resolution) do not occur much below 10 mA/cm^2 photocathode current densities.

In this paper we report results of experiments performed on 4 electrostatically focussed image converter cameras of differing electron optical configurations, with a view to evaluating the relative importance of space charge near the photocathode and that at the electron optical cross over point. The details of the four tubes are given in Table I.

Table 1. Details of tubes and optical systems

	Tube 1	Tube 2	Tube 3	Tube 4
Operating Voltage (V)	8 kV	8 kV	11.5 kV	6.5 kV
Magnification (β)	0.9	0.9	2.6	0.33
Phosphor Efficiency (η)	0.1	0.1	0.1	0.1
Collection Efficiency (Ω)	0.015	0.015	0.7	0.7
Photon Energy Density on the Film (α)	3×10^{-10} J/cm^2	3×10^{-10} J/cm^2	3×10^{-10} J/cm^2	3×10^{-10} J/cm^2
Photocathode Substrate Resistance (R)	100 Ω/□	100 Ω/□	100 Ω/□	1000 Ω/□
Electric field near photocathode (E)	2000V/cm	3500V/cm	400V/cm	200 V/cm
Type of photocathode	S-20	S-1	S-20	CsTe
Maximum resolution of 3 ns N_2 laser pulse	10 lp/mm	10 lp/mm	10 lp/mm	10 lp/mm

It will be observed, at equal anode potential, each tube has a different field near the photocathode. Thus, it was possible to separate out the effect of space charge due to the electric field near the photocathode and that at the anode cone where cross over of electron trajectories occurred.

Two of the four tubes had S-20 photocathodes while the others were CsTe and S-1 photocathodes respectively.

Experimental

A nitrogen laser with $\frac{1}{2}$ width (i.e. duration at half maximum amplitude) of 3 nanoseconds was used in all the experiments as a short light source to illuminate different resolution charts. Figure 1 shows schematically the details of the experimental set up.

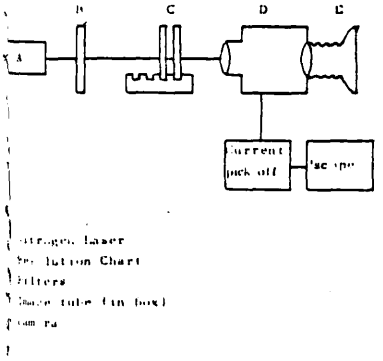

Fig. 1a

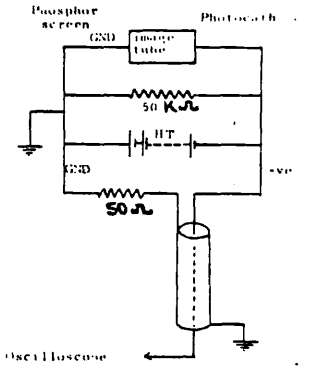

Fig. 1b

Fig. 1a Schematic of experimental set-up.

Fig. 1b Current pick-off circuit.

The total area on the photocathode which was illuminated by the laser was kept small. In most experiments there were large unilluminated areas around the illuminated spots - the resolution chart was a simple printed circuit board with equispaced holes. The input optics on the photocathode was such that the diameter of the illuminated dots were 0.6 mm for all the tubes. Although this is a very coarse resolution test, this was an adequate pattern for our observations concerned.

The total illuminated area on the photocathode of each camera was known and the photocathode current density was evaluated by measuring the voltage on a capacitor used to collect the charge according to the following equation:

$$I = \frac{i}{a} = \frac{Q}{a.\tau} = \frac{C \cdot V}{a \cdot \tau} \qquad (2)$$

where a = illuminated cathode area
i = photocurrent
V = measured voltage
I = current density
τ = N_2 laser pulse = 3 nanoseconds

The intensity profile of the nitrogen laser pulse was measured using a beam splitter photodiode combination.

A large number of recordings had to be taken to average out any errors due to the laser output fluctuations (both in amplitude and spatial pattern).

The tubes 3 and 4, unlike the other two, had fibre optic output windows. An F2 relay lens with 1:1 magnification was used to record the phosphor image of tubes 1 and 2 on 35 mm film. HP4 plate film was used to record the output from tube 3.

Photographic records were taken on Kodak 2475 when tube 1 was being tested. Since this tube had no fibre optic output window, it required a much higher current density than the other tubes to produce any recordable image. It was not possible to get an undistorted image on any other film when this tube was used. FP4 film was used to record images from tube 2 successfully. Figure 2 showed a series of photographs with current densities increasing from threshold of recording to serious distortions for tube 1.

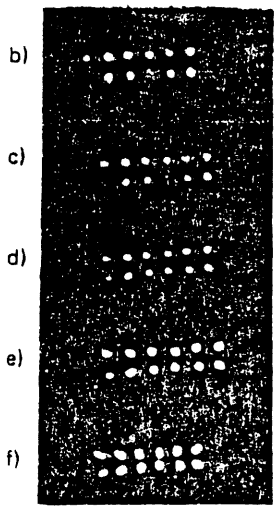

Fig. 2 Photographs taken on Kodak 2475 film using tube 1. Photocurrent densities were

a) 7 mA/cm^2
b) 28 mA/cm^2
c) 64 mA/cm^2
d) 110 mA/cm^2
e) 200 mA/cm^2
f) 240 mA/cm^2

However it will be noticed that no serious distortion was observed below current densities of about 40 mA/cm^2. The electric field near the photocathode of this tube was estimated to be around 2000 V/cm, a value much higher than in either tube 3 (~ 400 V/cm) or tube 4 (~ 200 V/cm). It was interesting to note that even at current densities of around 200 mA/cm^2 the resolution of this tube was better than 0.3 mm at photocathode, although

was very serious collapse of the image towards the centre due to space charge.

In Figure 3 a similar series of photographs are shown for tube 2. The distortion of image remained tolerable up to a current density of 180 mA/cm^2 (Kodak FP4 film was used).

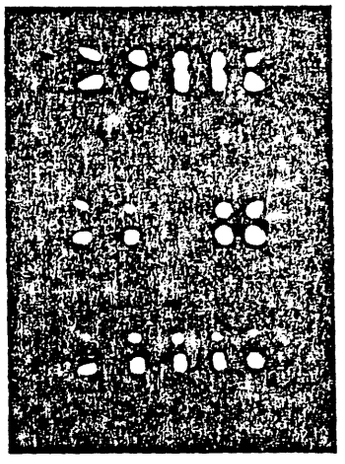

Fig. 3 Photographs taken on Kodak FP4 film using Tube 2. Photo-current densities were

a) 100 mA/cm^2

b) 150 mA/cm^2

c) 180 mA/cm^2

Figure 4 a similar series of photographs are shown for tube 3. Here, the distortion image could be considered negligible up to a photo-electron current density of imately 3.5 mA/cm^2. The lower electric field in this tube compared to the above uld cause space charge effects to appear at the levels observed. The upper end of namic range of the tube could be recorded on HP4 plates, which was used in this of photographs.

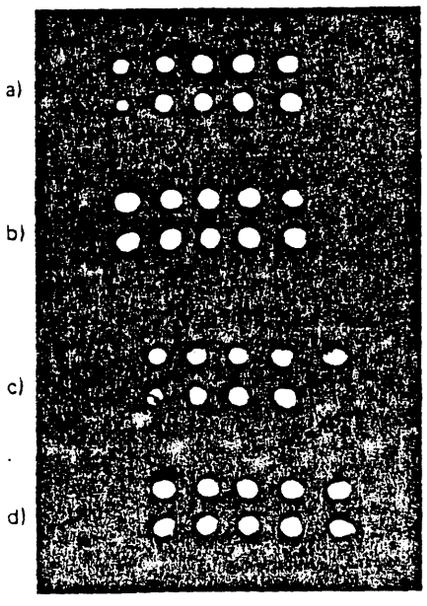

Fig. 4 Photographs taken on Ilford HP4 film using Tube 3. Photo-current densities were

a) 0.8 mA/cm^2

b) 3.2 mA/cm^2

c) 9 mA/cm^2

d) 13 mA/cm^2

We had to use a less sensitive film (Ilford FP4 or Kodak Pan F) to get at the upper end of the dynamic range of tube 4. Figure 5 shows prints of exposures taken using Kodak Pan F film.

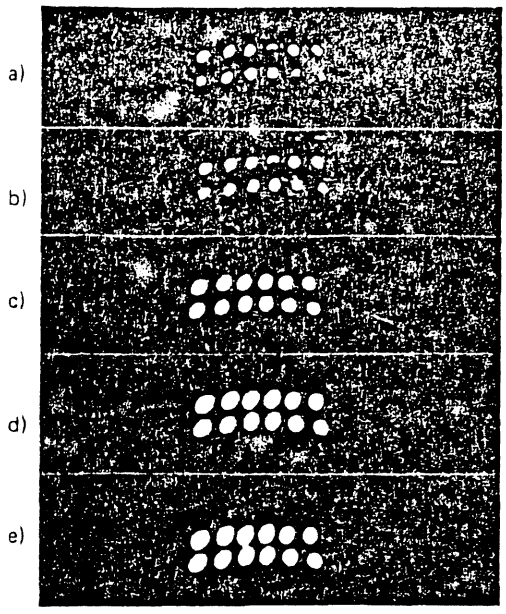

Fig. 5 Photographs taken on Kodak Pan F film using tube 4. Photo-current densities were

a) 0.3 mA/cm^2

b) 0.6 mA/cm^2

c) 1.2 mA/cm^2

d) 2.5 mA/cm^2

e) 4 mA/cm^2

Here again, we could see very similar image distortion as the current density at the photocathode was increased. However, the maximum current densities at which image distortion could still be considered negligible was around 1.2 mA/cm^2. Again, the lower still electric field near the photocathode of this tube could explain the lower current handling capacity of this tube. If three halves power low was applied to the three tubes to explain the threshold of space-charge limited image distortion, the ratio of current densities at which this effect should be expected, for the four tubes is about 32:73:3:1.

The photocathode substrate resistance of tube 4 was too high and non uniform in the middle of the tube. Hence an area near the outer edge of the photocathode had to be chosen to get the pictures shown in Figure 5. This caused a slight loss in the sharpness of the projected image on the photocathode and the oblong shape of the circular apertures.

Tube 4 had CsTe photocathode, which is non-conducting at room temperature. It is also not sensitive to visible light. Its quantum efficiency at 3371 Å (N_2 laser output) is much less than 0.5%; whereas for S-20 photocathodes of the other two tubes, the quantum efficiency at 3371 Å is nearly 5%. This meant that the photon density at the photocathode of tube 4 was at least an order of magnitude higher than that for the other two tubes. The light level, however, was too low to produce any significant non-linear photo-electric effect.

The effect of photocathode resistance on the image quality, was not significant in the current densities considered for tube 1, tube 2 and tube 3 - they had substrate resistance of the order of 100 Ω/□. With tube 4, when the right photocathode area was chosen, the effect of the photocathode surface resistance could be minimised to tolerable limits for current densities up to 1.2 mA/cm^2.

The experiments discussed above were done using nitrogen laser outputs of 3 nanosecond duration. In order to evaluate any possible change in tube behaviour for picosecond pulses, a series of experiments was performed using a ruby laser pumped mode-locked dye laser on tube 1. The mode-locked pulse train contained six or seven individual pulses of ~30 picosecond duration. A polaroid film (3000 ASA) was used for recording the integrated train of pulses. A resolution in excess of 5 line pairs per mm was achieved in this experiment. The tube did not show any substantial change in behaviour. Figure (6) shows a record of such an exposure.

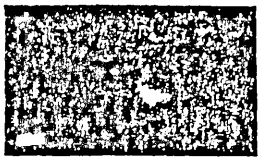

g. 6a Photograph of a grid pattern luminated by a train modelocked ruby ser pumped dye lasers. Seven individual ses were superimposed and integrated onto 3000A, polaroid film. Estimated current sity required for this photograph was 00 mA/cm^2.

Fig. 6b Oscillograph of modelocked dye laser pulse train. Time interval between pulses was 3.5 nanoseconds.

Results and Conclusions

The results are summarised in Table 2. It was found that tubes 1, 2 and 3 showed the collapse of the image towards the centre typical of space charge limitation near the photocathode. There was good agreement between the experimental limits of space charge with Child's law of space charge limitation, when the electric field near the photocathode was considered as the prime cause of image distortion observed.

Table 2

	Tube 1	Tube 2	Tube 3	Tube 4
Film	Kodak 2475	FP 4	HP4	Ilford FP4 or Kodak Pan F
Maximum current densities	40mA/cm^2	100mA/cm^2	3.5mA/cm^2	1.2mA/cm^2
Minimum current densities	5mA/cm^2	11mA/cm^2	0.5mA/cm^2	0.2mA/cm^2
Dynamic Range normalised for Kodak 2475	8	36	12	80

Of particular importance is the results obtained from tubes 1 and 2. These two tubes were of identical electron optical design except that tube 2 was of smaller dimensions than tube 1. When operated at the same anode potential, tube 1 had a field of about 2000 V/cm near the photocathode as opposed to 3500 V/cm for tube 2. The fact that tube 2 showed the onset of space charge induced distortion at a current density of 100 mA/cm^2 which is 3 times that for tube 1, at the same anode voltage, was a clear indication that the space charge effect at the cross over point of electron trajectory was negligible in comparison to that near the photocathode.

Tube 4 did not have a conventional photocathode, nor did it have a high conductivity substrate. As a result, this tube showed effects due to charging up of the photocathode surface[7,8]. This tube also had a very low electric field near the photocathode. Because of the two above 'faults', this tube could only be operated satisfactorily up to a photocathode current density of 1.2 ma/cm^2. However, its dynamic range was still the highest and this could be due to its demagnifying electron optics.

Acknowledgements

The authors are indebted to the Atomic Weapons Research Establishment for the loan of

tubes 3 and 4, and the the loan of other equipment for carrying out some of the experiments. They gratefully acknowledge the enthusiastic help of technical and clerical staff of the department and the interest shown by Professor D. W. O. Heddle in this work.

References

1. Schelev, M., Richardson, M. and Alcock, A. J., Rev. Sci. Instr., Vol 43, p. 1819, 1972.
2. Bradley, D. J., Bird, P. R. and Sibbet, W., Proc. 11th International Congress on High Speed Photography, p. 112, published by Chapman and Hall, 1975.
3. Coleman, L. W., Thomas, S. W., Houghton, J. W. and Tripp, G. R., Proc. of the 11th International Congress on High Speed Photography, p. 101, published by Chapman and Hall, 1975.
4. Schelev, M., Proc. 11th International Congress on High Speed Photography, p. 32, published in 1975 by Chapman and Hall.
5. Thomas, S. W., Houghton, J. W. and Coleman, L. W., Advances in Instrumentation, Vol. 29, part III, p. 745, 1974.
6. Majumdar, S.,"Current handling capacity of photocathodes with 1 to 1000 picosecond time resolution", To be published.
7. Thomas, B. R., Proc. 3rd Symposium of Photo-electronic Image Devices, 1970 Published in Adv. in Electronics and Electron Phys., Vol 33, p. 1119, Academic Press, 1970.
8. Diament, L., Proc. of the 5th Symposium on Photo-electronic Image Devices, 1975. To be published in Advances in Electronics and Electron Physics, Academic Press.

Reprinted from:

OPTICS COMMUNICATIONS

Volume 27, No. 3, December 1978

TIME RESOLVED SPECTROSCOPY OF SECOND HARMONIC EMISSION FROM LASER IRRADIATED MICROBALLOONS

P.D. CARTER and S.M.L. SIM
Dept. of Physics, Royal Holloway College, University of London, Egham, Surrey, TW20 OEX, UK

T.P. HUGHES
Dept. of Physics, University of Essex, Colchester, Essex, CO4 3SQ, UK

pp. 423–425

NORTH-HOLLAND PUBLISHING COMPANY–AMSTERDAM

TIME RESOLVED SPECTROSCOPY OF SECOND HARMONIC EMISSION FROM LASER IRRADIATED MICROBALLOONS

P.D. CARTER and S.M.L. SIM
Dept. of Physics, Royal Holloway College, University of London, Egham, Surrey, TW20 OEX, UK

T.P. HUGHES
Dept. of Physics, University of Essex, Colchester, Essex, CO4 3SQ, UK

Received 25 August 1978

Time resolved second harmonic spectra from glass microballoons irradiated by neodymium laser pulses ($\sim 10^{16}$ W cm^{-2}, $\sim$ 100 ps) have been recorded with a resolution of $\sim$ 10 ps in time, $\sim$ 1 Å in wavelength and $\sim$ 10 μm in the target plane. Intense, time and wavelength resolution-limited spots appear, whose origin has not yet been explained.

Observations of spectrally and spatially resolved second harmonic emission from laser produced plasmas have been reported by several authors [1–6]. These have provided information about possible interaction processes and have been used to determine density scale lengths near the critical surface. Time resolved backscattered emission studies have also been reported [7,8]. We present here time resolved observations, with a spectral resolution of ~1 Å and temporal resolution of ~10 ps, of the spectrum of radiation emitted near the second harmonic wavelength from plasmas produced by two opposing Nd laser beams ($I_0 \sim 10^{16}$ W cm^{-2} $\Delta t \sim$ 100 ps) incident on D-T filled glass microballoon targets.

From earlier work [9], a typical time integrated second harmonic system is shown in fig. 1, with a red-shifted peak and asymmetric broadening mainly to the red. The total width is approximately 30 Å. The radiation was collected by one of the $f/1$ singlet lenses used to focus laser light on the target, and relay lenses produced a magnified image on the slit of the 0.5 m grating spectrograph. The limited solid angle illuminating the 1200 line mm^{-1} grating restricted the spectral resolution to about 0.3 Å.

To study the evolution of the spectrum in time, an Electrophotonics Photochron II streak camera with an S-20 photocathode was optically coupled to the output plane of the spectrograph, as shown in fig. 2. The singlet lenses were replaced with aspheric focussing doublet types. The size of the image on the spectrograph entrance slit was further increased which reduced the spectral resolution to ~1 Å, but gave good time resolution: although the time resolution of the camera alone (~5 ps) was determined by the camera entrance slit width, that of the entire system was limited by the range of path lengths in the spectrograph to 10 ps. The spatial resolution in the target plane was limited by the $f/1$ lens to about 10 μm at 5320 Å. The streak data were recorded photographically on Kodak type 2485 film. Separate exposures of the 5461 Hg I line

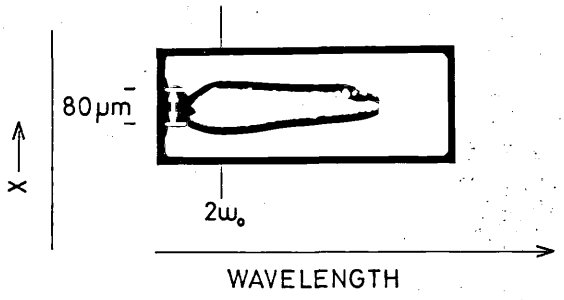

Fig. 1. Typical time integrated second harmonic spectrum $\Delta\lambda \sim$ 30 Å.

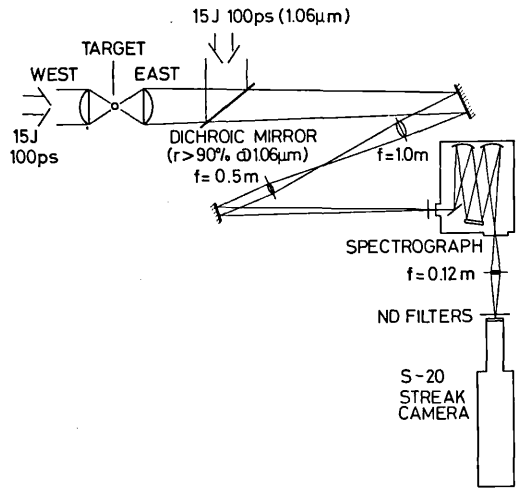

Fig. 2. Experimental layout for time resolved studies.

were taken with the spectrograph at different wavelength settings to define accurately both wavelength and dispersion. The temporal calibration was made using an air-gap etalon with 50% and 100% mirror reflectivities, in conjuction with a mode locked dye laser in an auxiliary experiment.

Three typical time resolved spectra are shown in fig. 3. They display similar spectral widths and broadening to those seen in the time integrated spectrum. However, the most striking feature of the data is the appearance of intense, spectrally and temporally resolution-limited, emission spots in the ($t\lambda$) plane. The majority of the intense spots lie in a region corresponding to a small blue shift (~ -4 Å). (There is some tentative indication that regular patterns of spots occur.)

The results are open to various interpretations. Existence of the spots cannot simply be attributed to Doppler shifts unless the plasma flow is oscillatory due to some hydrodynamic instability. Such an instability may be produced by the ablation flow across the density step, at critical density produced by the ponderomotive force of the laser beam. Another explanation for the pulsed second harmonic emission is that individual plasma waves grow on picosecond timescales and saturate by "wave breaking", producing fast electrons [10]. The fast electrons may then modify the plasma dielectric function and change the plasmon frequency for a constant density and wave number, thus shifting the second harmonic emission frequency. The observations might also be due to spatial motion of several descrete emitting regions through the source area observed, with a speed $\gtrsim 10^8$ cm s^{-1}; or to rapid variations in the direction of emission in a narrow pencil from a stationary source, possibly associated with rippling of the critical density surface [11].

The authors are grateful to the Science Research Council for support and for the use of the Rutherford Laboratory Laser Facility. They would also like to thank Dr. R.G. Evans for valuable discussions, Dr. E.

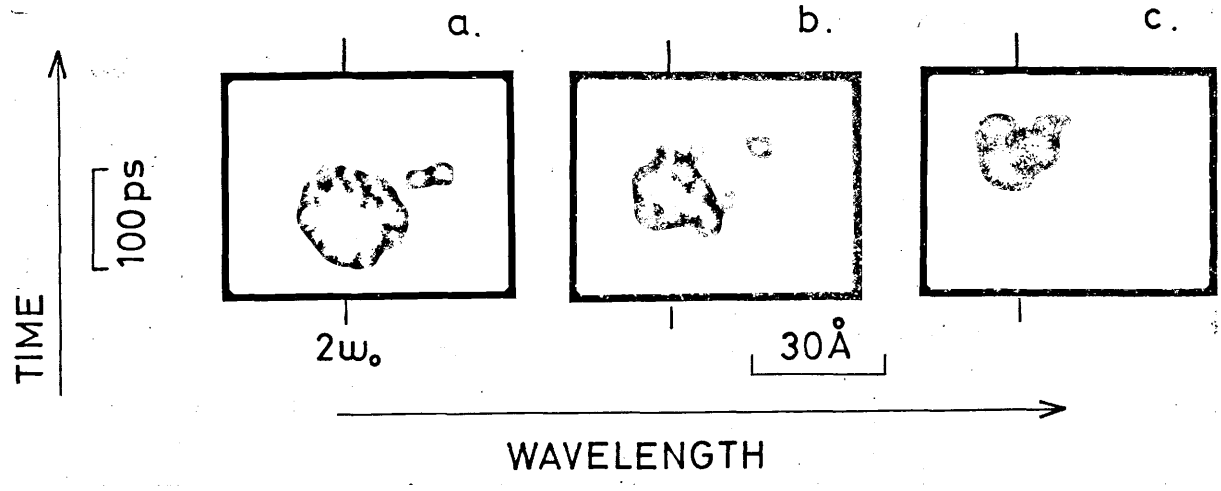

Fig. 3. Typical time resolved second harmonic spectra showing resolution limited emission "spots".

R. Wooding for guidance and other members of the Rutherford Laboratory Laser Division for assistance with the experiments.

References

[1] J.L. Bobin, M. Decroisette, B. Meyer and Y. Vitel, Phys. Rev. Lett. 30 (1973) 594.
[2] S. Jackel, B. Perry and M. Lubin, Phys. Rev. Lett. 37 (1976) 95.
[3] O.N. Krokhin et al., JETP Lett. 27 (1975) no. 1.
[4] E.A. McLean, J.A. Stamper, B.H. Ripin, H.R. Griem, J.M. McMahon and S.E. Bodner, Appl. Phys. lett. 31 (1977) 12.
[5] K. Eidman and R. Sigel, Phys. Rev. Lett. 34 (1975) 799.
[6] C. Yamanaka, T. Yamanaka, T. Sasaki, J. Mizui and H.B. Kang, Phys. Rev. Lett. 32 (1974) 1038.
[7] B.H. Ripin, J.M. McMahon, E.A. McLean, W.M. Manheimer and J.A. Stamper, Phys. Rev. Lett. 33 (1974) 634.
[8] V.Yu. Bychenkov et al., JETP Lett. 26 (1977) no. 6.
[9] SRC, Rutherford Laboratory report LD/78/04.
[10] J. Albritton and P. Koch, Phys. Fluids 18 (1975) 1136.
[11] R.A. Cairns, private communication.

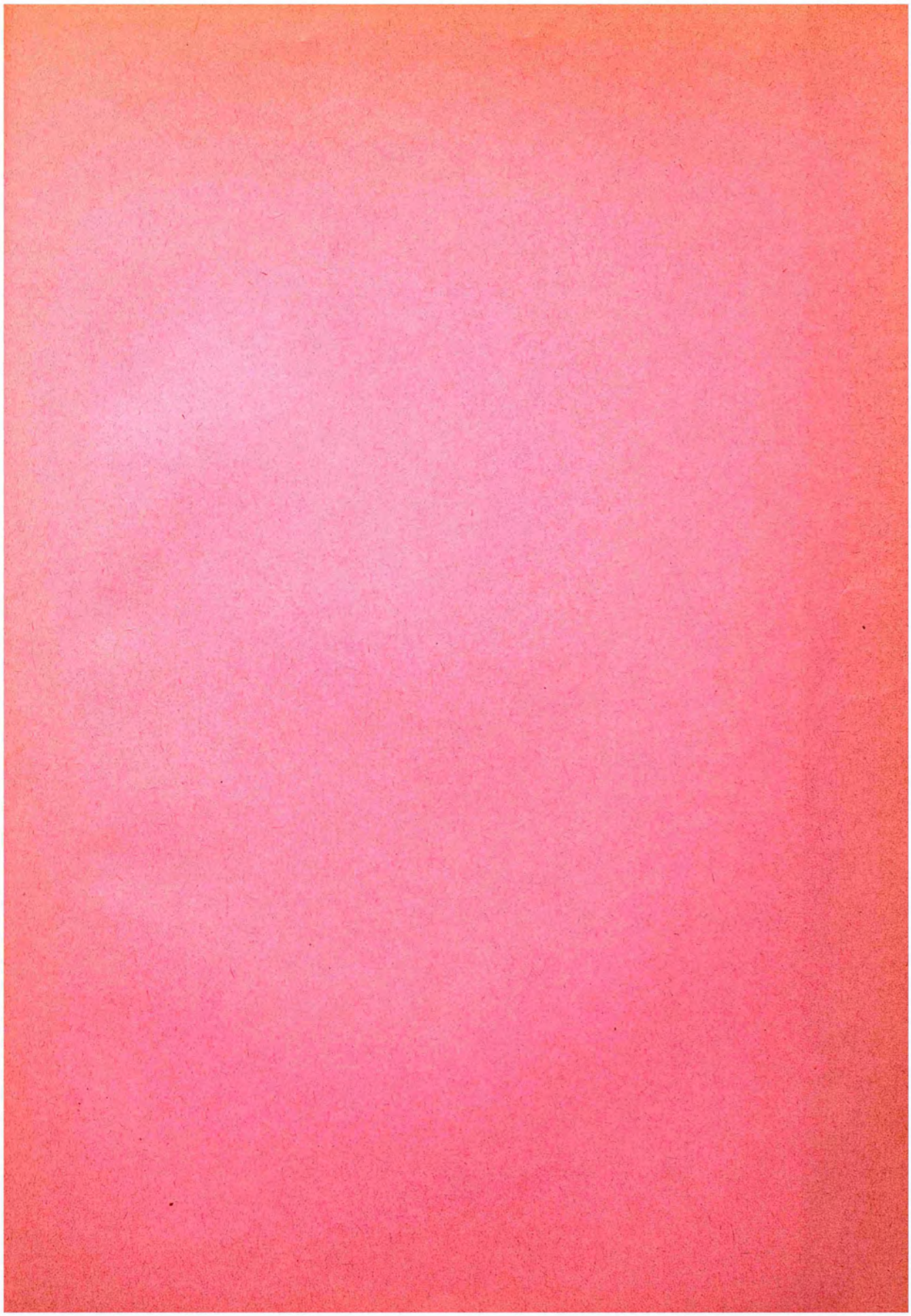

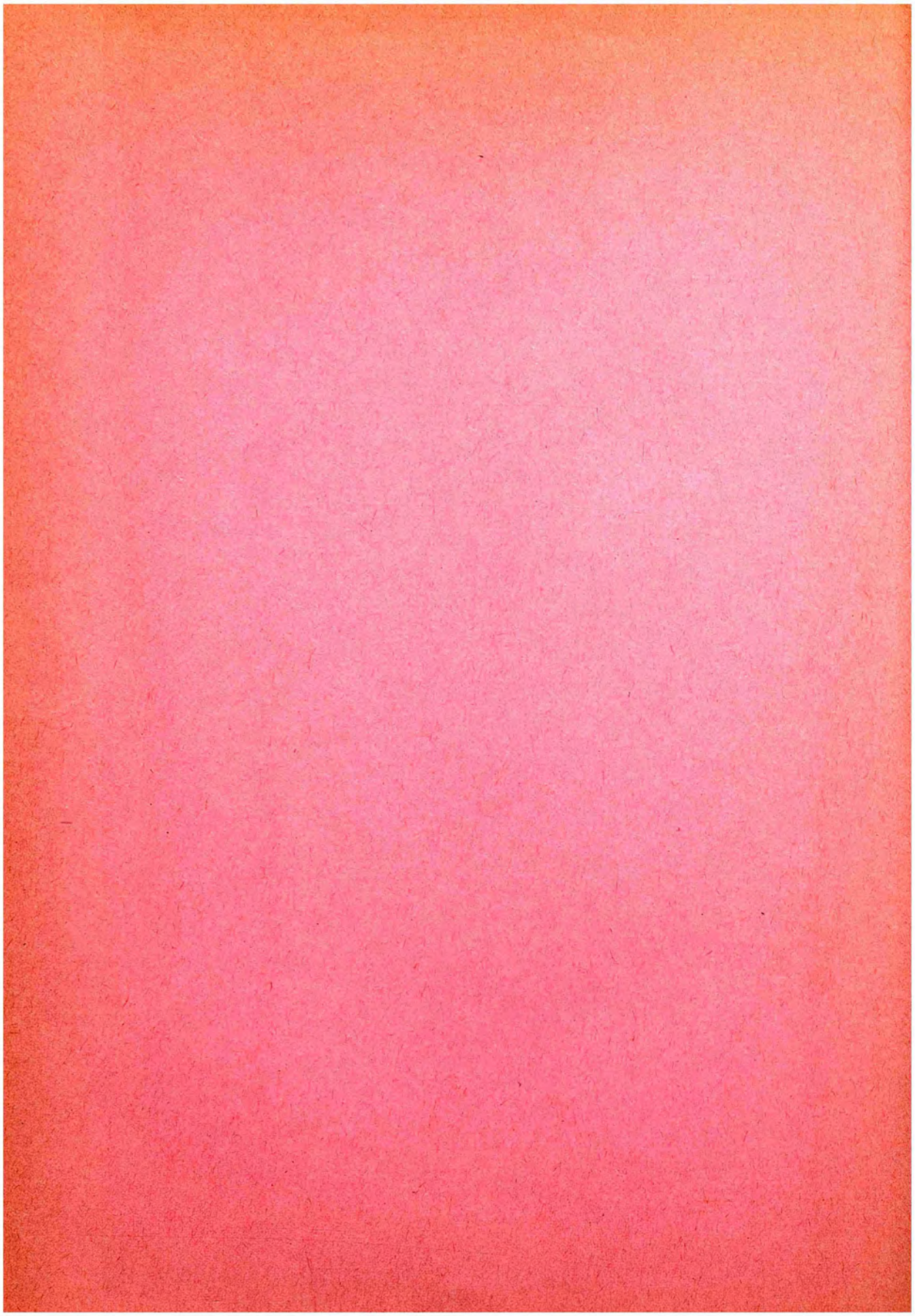

Plasma Physics, Vol. 22, pp. 967 to 976
Pergamon Press Ltd., 1980. Printed in Northern Ireland

TIME-RESOLVED SPECTROSCOPIC STUDIES OF LASER-PRODUCED PLASMAS

D. R. GRAY and J. MURDOCH
Imperial College, London SW7, U.K.

S. M. L. SIM
Royal Holloway College, Egham, Surrey, U.K.

and

A. J. COLE, R. G. EVANS and W. T. TONER
Rutherford Laboratory, Chilton, Didcot, Oxfordshire, U.K.

(*Received* 7 *December* 1979; *and in revised form* 1 *May* 1980)

Abstract—Temporally and spectrally resolved measurements of backscattered light at fundamental and 2nd harmonic are presented. Spherical targets (70–250 μm dia, $Z = 3$–50) are irradiated with a single beam from a Nd glass laser at irradiances of $I \sim 5$–50×10^{14} W cm^{-2}. The results show the presence of stimulated Brillouin scattering and other mechanisms. Calorimeter data shows reduced backscatter from high Z targets.

1. INTRODUCTION

STIMULATED Brillouin scattering (FORSLUND *et al.*, 1973, 1975. LIV *et al.*, 1974; PHILLION *et al.*, 1977; RIPIN *et al.*, 1977) is a process which severely reduces the efficiency with which laser energy can be coupled to a target. The incident laser wave at ω_0 couples to an ion wave at ω_{ia} and a scattered electromagnetic wave at ω^1 such that both energy and momentum are conserved.

$$\omega_0 = \omega^1 + \omega_{ia}$$
$$k_0 = k^1 + k_{ia}.$$

The energy of the ion acoustic wave is very small compared with the photon energy so very little of the laser energy is coupled into the plasma. The Brillouin instability may occur anywhere in the underdense plasma but is most likely at densities of a few tenths of the critical density (FORSLUND *et al.*, 1973, 1975; LIV *et al.*, 1974). A significant fraction of the incident energy is therefore prevented from penetrating to the critical density region where inverse bremsstrahlung absorption is more effective and where the collective absorption mechanisms operate. Stimulated Brillouin scattering (SBS) requires the presence of many wavelengths of underdense plasma and may be severe with the laser pulse durations of more than ~1 ns used for laser compression studies.

The characteristic signature of Brillouin scattering is the frequency shift to the red of the scattered radiation near ω_0 and a convenient means of investigating Brillouin scattering is to study the spectral and temporal properties of the light backscattered through the focusing lens. Both planar (ROSEN *et al.*, 1978; MEAD *et al.*, 1976; RIPIN *et al.*, 1974; GORBUNDV *et al.*, 1978) and spherical (AZECHI *et al.*, 1978) targets have been used. Time-integrated spectra of backscattered light generally display a small (~5 Å) red shift. The Brillouin red shift is partially cancelled by a Doppler blue shift associated with the expanding underdense

plasma. Tilting plane targets (ROSEN; RIPIN *et al.*, 1974) allows the Brillouin component to be isolated under the assumption that the plasma expands normal to the target surface.

Time-resolved studies have been conducted by a number of laboratories. Some workers (MEAD *et al.*, 1976; AZECHI *et al.*, 1978) report that, above some irradiance threshold, the backscattered component cuts off during the incident pulse. This has been explained by energy deposition arguments (MEAD *et al.*, 1976; KRUER *et al.*, 1975) by enhanced damping of ion waves or by reduced density scale lengths due to the ponderomotive pressure (AZECHI *et al.*, 1978).

Such behaviour is not observed by GORBUNOV *et al.* (1978) who have obtained time-resolved spectra from plane polyethylene and aluminium targets.

Results from NRL (RIPIN *et al.*, 1974) also do not display the cut-off behaviour, although a large prepulse modified the target behaviour in this case.

Time-resolved spectra generally display an early red shifted component, with the red shift subsequently decreasing with time. It is indicated below that we may identify blue shifts with supersonic plasma flow and red shifts with subsonic flow. The late blue components can then be understood as due to the build-up of a significant flow at large radii from the target.

In the present work, spherical targets are irradiated with a single, 1.06 μm beam and the light backscattered into the f/1 focusing lens is monitored. Principle diagnostics are (i) calorimetry at 1.6 μm (ii) time resolved spectra at 1.6 μm and (iii) simultaneous time resolved spectra at 0.53 μm. The effect of varying incident energy, target dia and target composition are presented in Section 3, followed by a discussion of the results in Section 4. Experimental details are given in Section 2.

2. EXPERIMENTAL ARRANGEMENT

The experimental arrangement is shown in Fig. 1. The main laser beam contains up to 110 J in 1.6 ns at a wavelength of 1.06 μm and is focused onto plane and microballoon targets by an aspheric doublet f/1 lens. The backscattered ω_0 radiation is directed onto a 1 m MONOSPEC grating spectrograph and the dispersed output is optically coupled onto an Electro-Photonics S1 streak camera. The wavelength and time resolutions are approximately 1 Å and 40 ps respectively and the relative timing of incident and reflected pulses is known to about 260 psec.

Simultaneous with the ω_0 spectroscopy, the backscattered $2\omega_0$ radiation is taken via a dichroic mirror to a 0.5 m SPEX grating spectrograph and an Imacon S-20 streak camera. The wavelength and time resolutions at $2\omega_0$ are about 1.0 Å and 5 ps respectively, approaching $\Delta t \Delta \nu = 1$.

The incident and reflected energies at 1.06 μm are monitored by two calorimeters, as shown in Fig. 1.

The targets are microspheres and microballoons in essentially two different sizes; 'small' of 70–90 μm dia and 'large' of 210–240 μm dia. A range of Z is used from plastic polymer to U^{238} in the small targets and from plastic to manganese nickel alloy in the larger size.

The duration (1.6 ns FWHM) and shape of the laser pulses were nominally unchanged throughout these experiments except for one or two multi-peaked pulses caused by mode beating in the laser cavity. The focusing of the laser

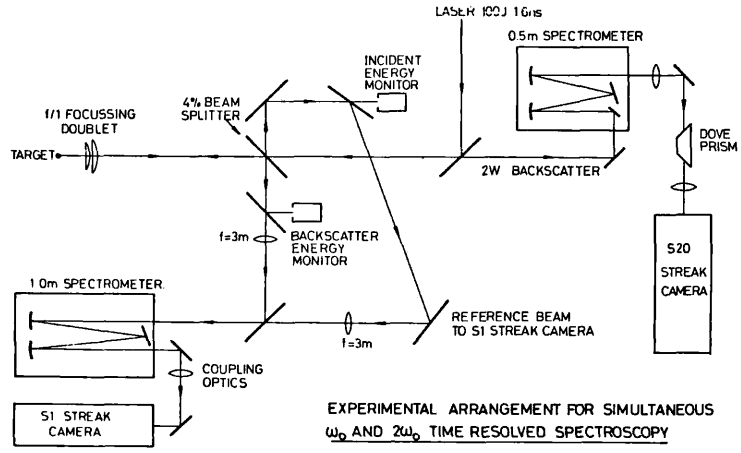

FIG. 1.—Experimental arrangement.

radiation by the f/1 lenses is onto the centre of the spherical targets so that all rays are close to normal incidence. On the small targets the peak irradiance for a beam energy of 100 J is 4×10^{15} W cm^{-2} and on the larger targets the corresponding irradiance is 5.2×10^{14} W cm^{-2}.

3. RESULTS

The backscattered energy measurements at 1.06 μm are summarised in Fig. 2, the error bars representing uncertainties of instrumental calibration. For a fixed target type, the fraction of laser energy which is backscattered into the focusing lens remains fairly constant over the limited range of irradiance that was studied. The light scattered outside the lens cone was not measured so that the angular distribution of scattered light was not determined.

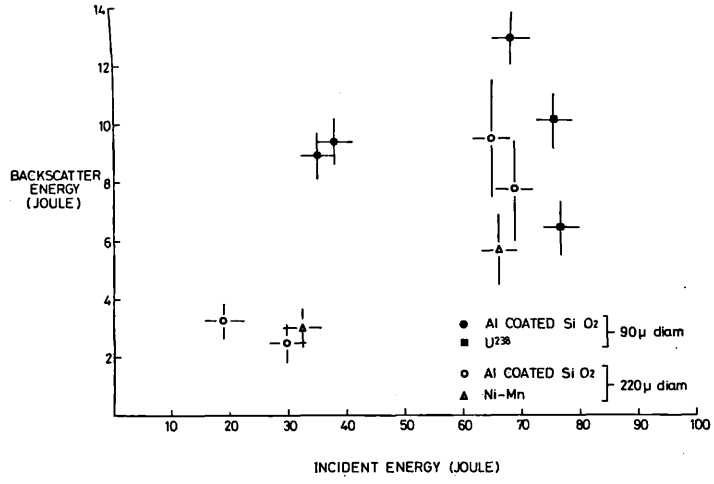

FIG. 2.—Calorimeter data; energy backscattered into f/1 focusing lens as a function of incident energy for various types of target.

FIG. 3.—Examples of time-resolved spectra

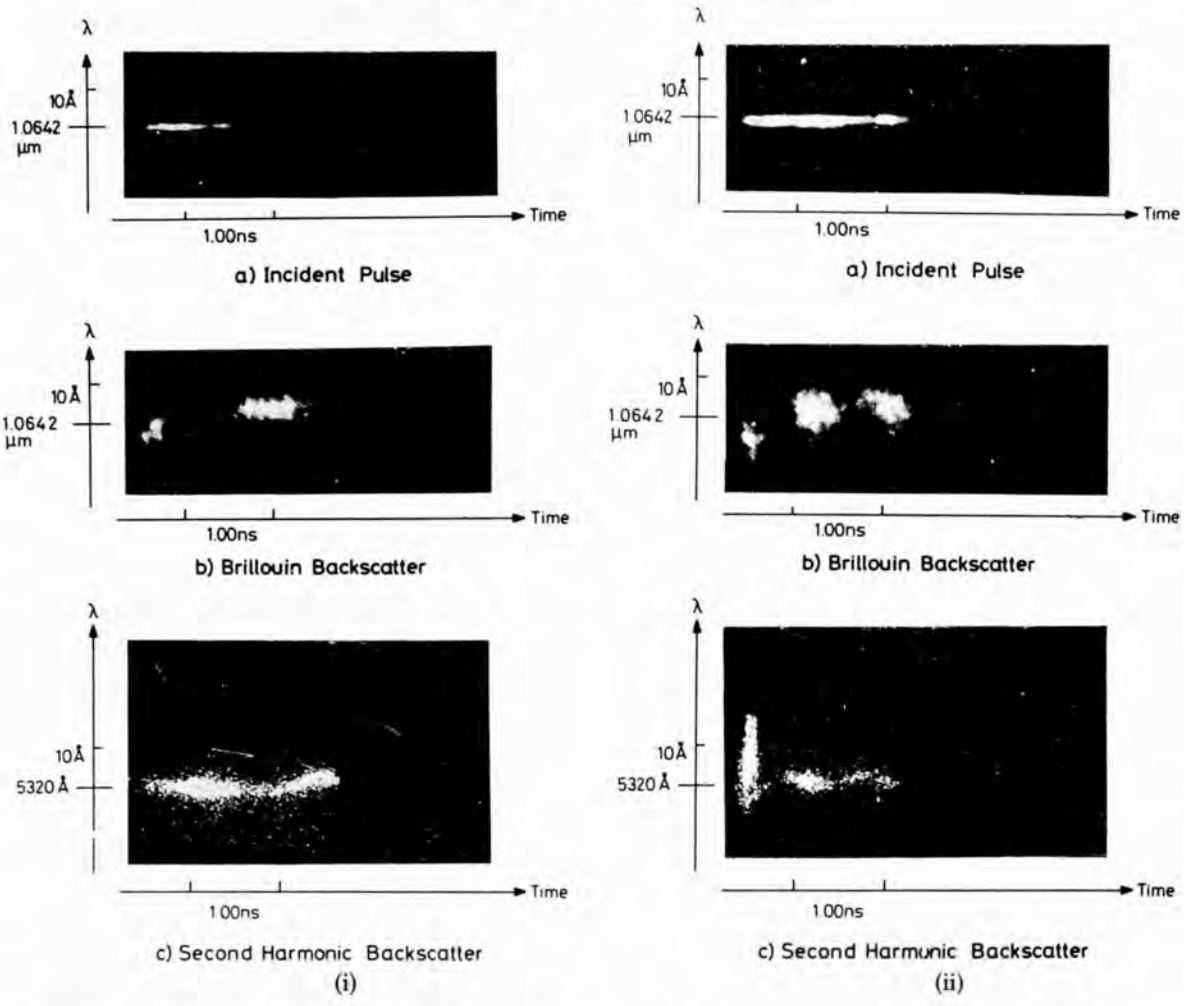

FIG. 3(i).—$E_{LAS} = 33$ J, $\phi = 4.2 = 10^{14}$ W cm^{-2}.

FIG. 3(ii).—$E_{LAS} = 76$ J, $\phi = 9.1 \times 10^{14}$ W cm^{-2}. Target = 250 μm Al coated glass microballoon.

For low Z targets, small microballoons generate more backscattered light (20–25%) than large microballoons (10–15%) for the same energy on target. This result appears to contradict the association of increased backscatter from larger plasmas. However, irradiance on the larger targets is substantially less than on the small targets and, as well as reducing the SBS growth rate, this may reduce the coronal temperatures sufficiently to inhibit the generation of long scale lengths in the underdense region. This is discussed further in the next section.

Both small and large targets of high Z material exhibit less backscatter (30–40% less) compared with the aluminium coated microballoons. We attribute this to the lower temperatures, and consequently smaller scale lengths, achieved in high Z targets because of their substantial radiative losses.

Some typical time-resolved spectra of the backscattered ω_0 radiation are shown in Fig. 3. The characteristic development of the spectra is as follows. A short burst of blue shifted ($\lesssim 5$ Å) light occurs very early in the incident pulse, followed by a long, red shifted component which generally lasts throughout the

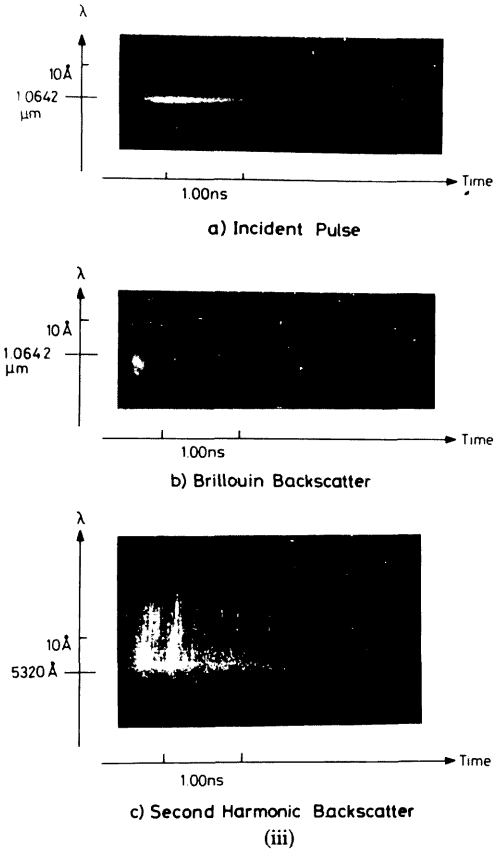

(iii)

FIG 3(iii).—$E_{LAS} = 35$ J, $\phi = 1.8 \times 10^{15}$ W cm^{-2}. Target = 90 μm U^{238} microsphere.

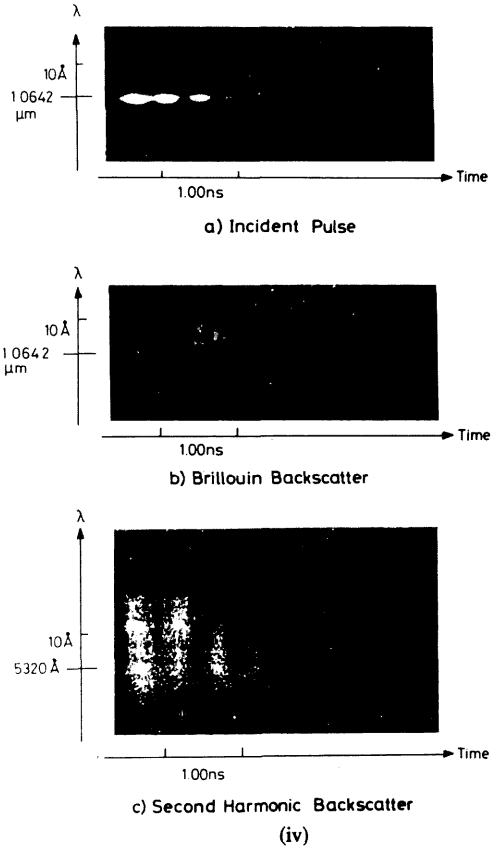

(iv)

FIG. 3(iv).—$E_{LAS} = 70$ J, $\phi = 3.5 \times 10^{15}$ W cm^{-2}. 85 μm Al coated glass microballoon.

incident pulse. Usually, the two components appear separate in time on the streak photographs.

Results from low irradiance ($<10^{14}$ W cm^{-2}) alignment shots on plane brass targets are of the form shown in Fig. 4. Here, spectrally broad but unshifted reflection is generated at first but cuts off during the incident pulse. This behaviour is similar to that observed by some other workers (HEAD *et al.*, 1976; AZECHI *et al.*, 1978) but is in marked contrast to our microballoon data.

In addition to the broad features, time-resolved spectra, especially the well exposed pictures, exhibit small scale structure in time (80 ps) and wavelength ~2 Å) which is not well understood.

Examples of the time-resolved $2\omega_0$ backscattered spectra are also shown in Fig. 3. At low irradiances ($\leqslant 10^{14}$ W cm^{-2}), the $2\omega_0$ emission is spectrally narrow and moves continuously in wavelength, presumably due to a Doppler shift. The spectral narrowness of the emission (<2 Å), would suggest that this emission is due to a 'resonant' effect at the critical density without the involvement of any ion acoustic waves. At slightly higher irradiances the $2\omega_0$ emission begins with a burst of spectrally broad emission, ~20 Å, and then reverts to spectrally narrow

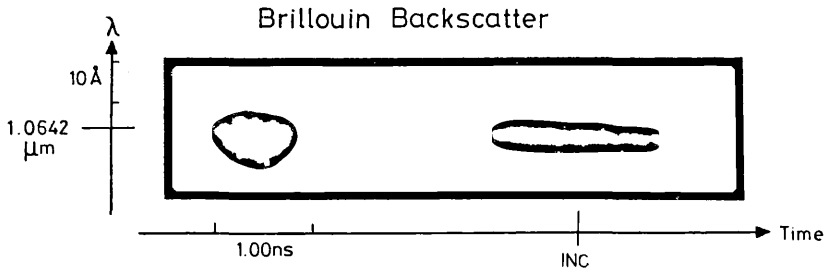

FIG. 4.—Time resolved ω_0 backscatter spectrum from a plane brass target; spot diameter $\simeq 30$ μm, $\phi \lesssim 10^{14}$ W cm^{-2}, incident pulse is marked 'INC'.

emission as on the lower irradiance shots. At irradiances of $>10^{15}$ W cm^{-2}, the broad emission persists throughout much or all of the laser pulse and appears as a series of discrete temporal pulses. Each pulse is close to the instrumental limit of time resolution and in many cases the pulses also break up into a set of fairly regular 'spots' in the spectral direction. The reasons for this small scale structure are being investigated.

4. DISCUSSION

(a) *Calorimeter data*

With the high Z targets there is competition between Brillouin scattering and inverse bremsstrahlung absorption. If the scale length for inverse bremsstrahlung absorption is less than that for Brillouin scattering, then the Brillouin scattering will be partially quenched. The high Z targets will have lower coronal temperature than the Al targets because of increased line and continuum radiation and this will reduce the hydrodynamic scale length of the blow-off plasma provided this is less than the geometrical scale length set by the target radius and the spherical divergence of the ablation flow.

On the basis of this geometrical scale length one would expect the large targets to have larger scale lengths and consequently larger Brillouin backscatter. The fact that this is not observed suggests that the reduced irradiance on the large targets gives smaller temperatures and the 1.6 ns pulse duration is then insufficient for these long scale lengths to evolve.

(b) ω_0 *Spectra*

The red shift of the backscattered radiation during most of the laser pulse is consistent with Brillouin scattering but the frequency shift also contains a component $\Delta\lambda_D$ due to the Doppler shift of the ablating material.

We can write the Doppler shift $\Delta\lambda_D$ as

$$\Delta\lambda_{D/\lambda_0} = -2v_{a/c} = \frac{-2Mv_{ia}}{c}$$

where v_a is the ablation velocity, v_{ia} is the ion acoustic phase velocity $v_{ia} = \sqrt{(ZkT_e/m_i)}$, and M is the Mach number of the flow. The red shift due to the ion

acoustic wave generated by Brillouin scattering will be

$$\Delta\lambda_{B/\lambda_0} = \frac{\omega_{ia}}{\omega_0} = \frac{2k_0 v_{ia}}{\omega_0} = \frac{2v_{ia}}{c}$$

where we have used the result that the wave number of the ion acoustic wave has modulus $\sim 2k_0$.

The net red shift is then

$$\Delta\lambda/_\lambda = \frac{2v_{ia}}{c}(1-M)$$

showing that the shift is to the red if the flow is subsonic and to the blue if the flow is supersonic.

In their experiments on high Z disk targets the Livermore group (Rosen *et al.*, 1978) have shown that the Brillouin and Doppler components of the frequency shift may be separated, at least approximately, by tilting the target by 45°. The Doppler shift is then reduced by cos 45° while the Brillouin shift is essentially unchanged. Their results, at irradiances of 3.10^{14} W cm^{-2} and 3.10^{15} W cm^{-2} with a 1 ns pulse on a gold target, show that the flow Mach number M is about 0.8 and 0.84 respectively. Unfortunately this shows that a measurement of the reflected ω_0 spectrum is not a good indicator of the electron temperature in the under dense plasma because of the close cancellation of the two contributions to the wavelength shift. If we use the value of the Mach number of $M = 0.82$ and take $\Delta\lambda = 5$ Å for the high irradiance shots on Al coated microballoons ($\phi \sim 4 \cdot 10^{15}$ W cm^{-2}) then

$$v_{ia} = \frac{c\Delta\lambda}{2\lambda(1-M)} = 4\times 10^7 \text{ cm s}^{-1}.$$

Also $v_{ia} = [ZkT_e/A_p{}^m]^{1/2}$ where A is the ion mass number and m_p the proton mass.

Thus if $M/Z = 2$, we have as an estimate of the coronal electron temperature; $T_e = 3.3$ KeV.

One of the laser shots exhibited very strong mode beating with four separate pulses each of about 200 ps FWHM. We have performed integrations in wavelength and time for the backscattered ω_0 spectrum and by normalising to the total backscattered energy, we calculate the amount of SBS in each of the four beats. The time history of the laser pulse is shown in Fig. 5 and the incident and backscattered energies are summarised in Table 1. The third and fourth beats of the laser pulse have backscatter fractions greater than unity but we attribute this to uncertainties in the film calibration and to the very limited dynamic range of the streak camera. Simulations of this shot with our 1-D hydro code show strong profile modification for the first two beats of the laser pulse and in those conditions strongly 2-D effects in the plasma flow will be expected. For the third and fourth beats of the laser, the profile modification is weak and more nearly spherical flow and very long density scale lengths ~ 100 μm are expected. These results are in qualitative agreement with the predictions of Kruer *et al.* (1975).

We note that these measurements suggest very low absorption for pulse

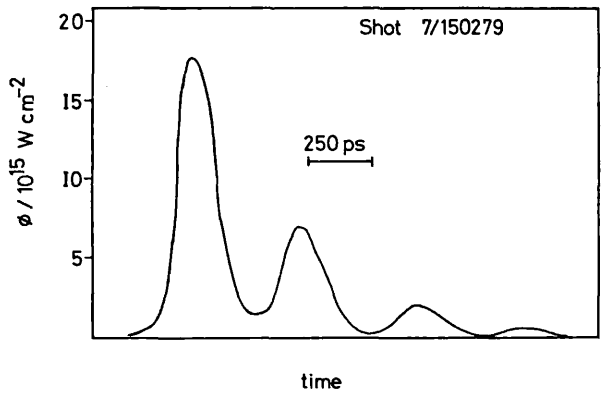

FIG. 5.—Multi-peaked incident laser pulse used to calculate reflectivities (see text).

lengths significantly greater than 1 ns at irradiances $\sim 10^{14}$–10^{15} W cm^{-2} on moderate Z targets. Little data is available but recent results from NRL (RIPIN *et al.*, 1979), show large absorption for 6 ns pulses at irradiances up to 10^{14} W cm^{-2} on fairly high Z targets. We assume that in this case the SBS is partly suppressed by large inverse bremsstrahlung absorption.

The centroid of our backscattered spectrum, although red shifted, is generally moving towards the blue by the end of the incident pulse. This is consistent with the observations of RIPIN *et al.* (1974) and GORBUNOV *et al.* (1978).

We also observe a short blue component that occurs early in the incident pulse. We believe this to be due to specular reflection from the initially steep, moving, density jump near the critical layer with no Brillouin scattering at this early time. At the very highest irradiances (Fig. 3 iv) no initial blue shifted component is observed probably due to the fact that the Brillouin threshold is exceeded earlier.

(c) $2\omega_0$ *Spectra*

The difference between the spectrally narrow and broad emissions at $2\omega_0$ appears to correlate with steep density gradients near critical density. At moderate irradiances $\leqslant 5 \times 10^{14}$ W cm^{-2} the ponderomotive pressure of the laser beam is not sufficient to cause steepening of the density profile but a steep profile will exist in the initial part of the laser pulse before significant hydrodynamic motion has

TABLE 1.—SHOT 7/150279; TARGET 85 μm DIA Al-COATED, GLASS MICROBALLOON

Pulse	E_{INC} (J)	E_{BS} (J)	r (%)
1	41.2	2.4	6
2	19.0	3.0	16
3	5.7	5.7	100
4	1.8	1.9	~100
	67.7	13.0	

occurred. At higher irradiances, when the ponderomotive pressure is important, the steep density profile will persist throughout the laser pulse. In the presence of the steep density profile, resonance absorption is enhanced and is known to produce many fast electrons; the cold electron return current needed to maintain charge neutrality can drive ion acoustic turbulence. This is probably responsible for the spectrally broadened $2\omega_0$ emission since large amplitude ion waves can induce a spectrum of electron plasma wave frequencies.

We note also that when the $2\omega_0$ emission is spectrally broad, there is a modulation of the emission into bursts of less than 15 ps duration spaced by about 30–40 ps. This could be explained in terms of saturation of the mechanisms of production of $2\omega_0$ emission but we believe that this is unlikely since identical behaviour has been observed (CARTER *et al.*, 1980) in $\frac{3}{2}\omega_0$ emission from similar targets.

There appears to be no reason why different densities should exhibit similar behaviour except for the hydrodynamic flow in the expansion of the plasma. Since the oscillations in the $2\omega_0$ emission occur only when the density profile is significantly steepened, it is reasonable to suggest that the ablation flow across the steep density profile may be unstable (MAX and MCKEE, 1977).

These density fluctuations will then propagate out through critical density to the quarter critical density region and affect both the $2\omega_0$ and $\frac{3}{2}\omega_0$ emissions. The time scale of such fluctuations would be expected to be $\tau \sim L/v_{ia}$ where L is the density scale length at critical density and v_{ia} is the ion acoustic speed. If we take the plausible values $L \sim 3\,\mu\text{m}$, $v_{ia} \sim 2 \times 10^7\,\text{cm s}^{-1}$ then $\tau \sim 15\,\text{ps}$ which is in reasonable agreement with the observed value.

5. CONCLUSION

This work has shown that the target material can significantly change the amount of Brillouin backscatter, high Z materials producing less backscatter. Further work is needed to make these conclusions more quantitative and also to establish the variations of Brillouin backscatter with target radius and laser irradiance.

The time development of the backscattered fundamental frequency shows that the backscatter persists for the whole of the laser pulse but also exhibits very short duration modulations which are yet unexplained. The nature of the second harmonic emission suggests that the spectral broadening is associated with fast electron production through the ion turbulence set up by the fast electron return current. Oscillations in the $2\omega_0$ emission occur only in the presence of steep density gradients and are suggestive of a hydrodynamic flow instability.

REFERENCES

AZECHI H., FUJITA H., IMASAKI K., IZAWA Y., KATO Y., KAWAMURA Y., MATOBA M. MIMA K., MIYAMOTO S., MIZUMOTO Y., MOCHIZUKI T., NAKAI S., NISHIHARA K., NISHIMURA H., NORIMATSU T., SASAKI T., TAKABE H., THOMSON J. J., YOSHIDA K., YAMANAKA T., and YAMANAKA C. (1978) Paper IAEA-CN-37-M-4. Conference on Plasma Physics and Controlled Nuclear Fusion Research, Innsbruck, August.

CARTER P. D., SIM S. M. L. BARR H. C. and EVANS R. G. to be published in *Phys. Rev. Lett.*

FORSLUND D. W., KINDEL J. M. and LINDMANN E. L. (1973) *Phys. Rev. Lett.* **30,** 739.

FORSLUND D. W., KINDEL J. M. and LINDMANN E. L. (1975) *Phys. Fluids* **18,** 1002.

GORBUNOV L. M., KAS'YANOV YU. S., KOROBKIN V. V., POLYANICHEV A. N. and SHEVEL'KO A. P. (1978) *JETP Lett.* **27,** 226.
KRUER W. L., VALEO E. J. and ESTABROOK K. G. (1975) *Phys. Rev. Lett.* **35,** 1076.
LIU C. S., ROSENBLUTH M. N. and WHITE R. B. (1974) *Phys. Fluids* **17,** 1211.
MAX C. E. and MCKEE C. F., (1977) *Phys. Rev. Lett.* **39,** 1336.
MEAD W. C., HAAS R. A., KRUER W. L., PHILLION D. W., KORNBLUM H. N. LINDL J. D., MACQUIGG D. R. and RUPERT V. C. (1976) *Phys. Rev. Lett.* **37,** 489.
PHILLION D. W., KRUER W. L. and RUPERT V. C. (1977) *Phys. Rev. Lett.* **39,** 1529.
RIPIN B. H., MCMAHON J. M., MCLEAN E. A., MANHEIMER W. M. and STAMPER J. A. (1974) *Phys. Rev. Lett.* **33,** 634.
RIPIN B. H., YOUNG F. C., STAMPER J. A., ARMSTRONG C. M., DECOSTE R., MCLEAN E. A. and BODNER S. E. (1977) *Phys. Rev. Lett.* **39,** 611.
RIPIN B. H., WHITLOCK R. R., YOUNG F. C., OBENSCHAIN S. P., MCLEAN E. A. and DECOSTE R. (1979) *Phys. Rev. Lett.* **43,** 350.
ROSEN M. D., PHILLION D. W., RUPERT V. C., MEAD W. C., KRUER W. L., THOMSON J. J., KORNBLUM H. N., SLIVINSKY V. W., CAPORASO G. J., BOYLE M. J. and TIRSELL K. G. (1978) Lawrence Livermore Laboratory Report No. UCRL 82146.

TIME-RESOLVED OBSERVATIONS OF THE THREE-HALVES HARMONIC SPECTRUM FROM LASER-PRODUCED PLASMAS

P. D. Carter, S. M. L. Sim, H. C. Barr, and R. G. Evans

Reprinted from PHYSICAL REVIEW LETTERS Vol. 44, No. 21, 26 May 1980
1407

Time-Resolved Observations of the Three-Halves Harmonic Spectrum from Laser-Produced Plasmas

P. D. Carter and S. M. L. Sim[a]
Department of Physics, Royal Holloway College, University of London, Egham, Surrey TW20 0EX, United Kingdom

and

H. C. Barr
School of Mathematics and Computer Science, University College of North Wales, Bangor, Gwynedd LL57 2DG, Wales

and

R. G. Evans
Laser Division, Rutherford Laboratory, Chilton, Didcot, Oxon OX11 0QX, United Kingdom
(Received 26 March 1980)

Time-resolved $\frac{3}{2}\omega_0$ spectra from glass microballoons irradiated by 100-ps, 2×10^{16}-$W\cdot cm^{-2}$ laser pulses have been obtained with a temporal resolution of 20 ps and a spectral resolution of 15 Å. Pulsed emission is observed, with a pulse duration of less than the instrument limit. Both red and blue peaks appear simultaneously, with their separation varying in time.

PACS numbers: 52.25.Ps, 52.50.Jm

In recent years much theoretical and experimental work has been performed to study the various parametric processes which occur in laser-produced plasmas at high irradiances. At one quarter of the critical density both stimulated Raman scattering[1] and two-plasmon decay[2] can

occur, and either of these can give rise to the emission of radiation at $\frac{3}{2}\omega_0$. These instabilities at a quarter of critical density are probably not very important for the overall absorption of laser energy by the plasma,[3] but may be responsible for the production of a significant number of fast electrons.[4]

Previous observations of the $\frac{3}{2}\omega_0$ emission have been of time-integrated spectra[3,5] or of the time-resolved intensity.[6,7] Bychenkov *et al.*[8] have obtained time-resolved spectra with a long laser pulse and time resolution of 100 ps. We present here new observations of the time-resolved spectra with high time resolution of ~10 ps and simultaneous spectral resolution of 30 Å. The measurements were made with the Rutherford Laboratory Nd-glass laser facility providing an irradiance of 2×10^{16} W cm^{-2} in a 100-ps pulse on glass microballoon targets of 50–90 μm diam.

The experimental layout is shown in Fig. 1. The backscattered $\frac{3}{2}\omega_0$ radiation was collected by the $F1$ doublet lens, used to focus the laser light on the target. This lens produced a 60× magnified image at $\frac{3}{2}\omega_0$ on the slit of the 0.5-m, 600-line·mm^{-1} grating spectrograph; the slit size of 1 mm restricted the spectral resolution to about 15 Å. The output plane of the spectrograph was then optically coupled to a Hadland Photonics streak camera fitted with an S-20 photocathode, with use of a dove prism to rotate the image so that wavelength would be dispersed along the streak camera slit.

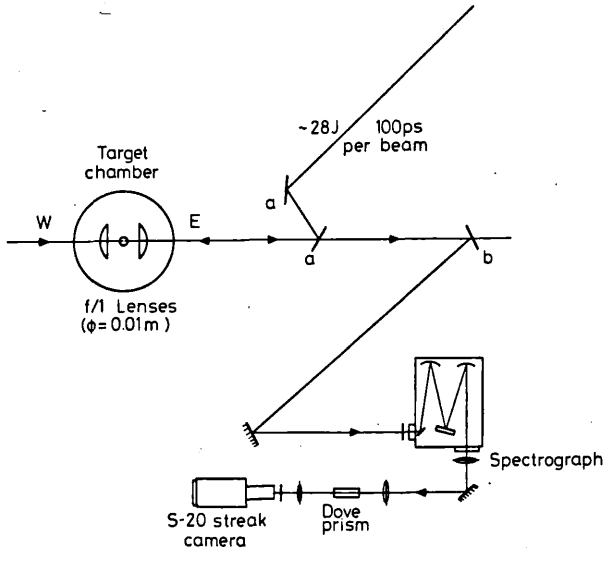

FIG. 1. Experimental layout for time-resolved $\frac{3}{2}\omega_0$ spectra.

Although the time resolution of the streak camera alone (~5 ps) was determined by its entrance slit width, that of the entire system was limited by the range of path lengths in the spectrometer to ~20 ps. Photographic recordings of the streak data were made on Kodak 2485 film and separate exposures of the 5461-Å Hg I line were taken with the spectrograph at different wavelength settings to calibrate both wavelength and dispersion. The sweep speed of the streak camera was calibrated in an auxiliary experiment using a mode-locked dye laser and an air-gap etalon with 70% mirror reflectivities.

Two typical time-resolved spectra are shown in Fig. 2. Both spectral streaks show that the $\frac{3}{2}\omega_0$ harmonic emission has a pulsed nature, where the duration of the pulses is less than the ~20-ps temporal resolution of the system, with the spectrograph in second order. (Spectra showing resolution-limited bursts of < 10 ps were obtained with the spectrograph in first order.)

The blue-shifted and red-shifted peaks appear simultaneously but with their separation varying in time. Spectra with monotonically decreasing separation [Fig. 2(a)] were obtained when the laser prepulse level was low (< 10^{-5} times the main pulse energy) while spectra showing an increasing and then decreasing separation [Fig. 2(b)] occurred as a result of larger prepulse levels. The blue-shifted peaks appear more intense than the red-shifted peaks which is the reverse of the time-integrated observations.[3,5] This is probably due to the spectral response of the S-20 photocathode which falls off rapidly in the red near 7093 Å and may also be accentuated by any error between the direction of spectral dispersion and the slit of the streak camera.

The spectrum of the $\frac{3}{2}\omega_0$ emission has been calculated by Avrov[9] and by Barr.[10] The Barr theory differs from Avrov's theory is that Avrov neglects the wave number k_0 of the pump wave, compared with the wave number k of the plasma waves, while Barr makes no such assumption. For the conditions of our experiment plasma waves with $k \gg k_0$ are strongly Landau damped so that the Avrov theory is not applicable.

The Barr theory considers three mechanisms for the production of $\frac{3}{2}\omega_0$ radiation: combination of three plasma waves, combination of a plasmon with an incident pump photon, or combination of a plasmon with a pump photon reflected from critical density. The blue-shifted wing of $\frac{3}{2}\omega_0$ emission arises from forward scattering, i.e., towards higher densities and the light must then be

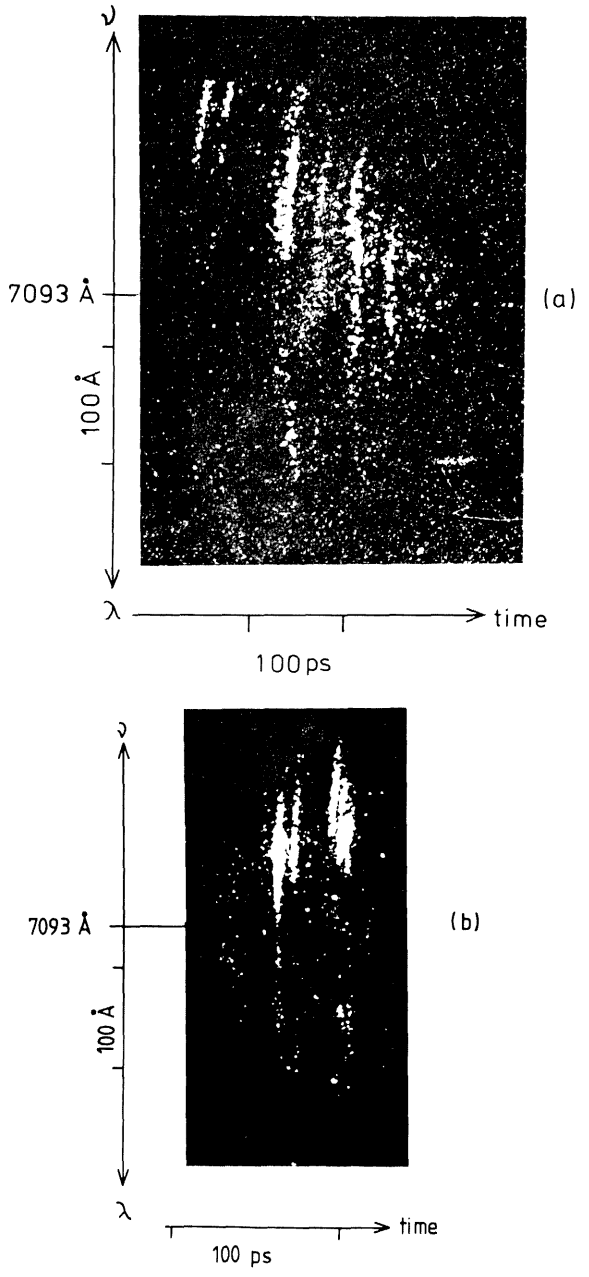

FIG. 2. (a) $\frac{3}{2}\omega_0$ spectral streak showing decreasing separation (in time) between peaks; temporal resolution ~20 ps, spectral resolution ~15 Å. (Curvature is due to "pincushion" distortion in the image intensifier.) (b) $\frac{3}{2}\omega_0$ spectral streak showing increasing, then decreasing separation in time between peaks; temporal resolution ~20 ps, spectral resolution ~15 Å.

reflected at a density nine-fourths critical. The red-shifted wing is directly backscattered. If only plasma waves with $\vec{k}$ close to the fastest growing mode are considered then the dominant contributions to our backscatter spectra will arise from the combination of the reflected pump wave and the plasma waves. The frequency shift of the $\frac{3}{2}\omega_0$ radiation arises from the Bohm-Gross correction to the plasma frequency and is always proportional to T_e, the electron temperature. For the modes of maximum growth rate the wavelength shifts of $\frac{3}{2}\omega_0$ are $\Delta\lambda_R = 19.0T_e$, $\Delta\lambda_B = -29.8T_e$, with T_e in kiloelectronvolts and $\Delta\lambda$ in angstroms. For $\frac{3}{2}\omega_0$ radiation close to the laser axis $\Delta\lambda_R = 23.3T_e$ and $\Delta\lambda_B = -44.3T_e$. We have also considered the effects of Brillouin-shifted reflection of the pump wave and of Doppler shifts due to the motion of the quarter-critical region. These are much less than the observed shift of the $\frac{3}{2}\omega_0$ radiation, being of order 10–20 Å. Moreover, the Brillouin shift is reduced to zero if the expansion of the plasma is at the sound speed.

The spectra presented here show a fairly symmetrical shift of the red and blue wings with a slightly larger shift to the red. We feel that the discrepancy between this and the simple theory may be due to rippling[11] of either the critical or quarter-critical density surfaces giving rise to an uncertainty in the angular relationship of the plasma waves and electromagnetic waves. Also the Barr theory has assumed that the nine-fourths-critical density layer is parallel to the quarter-critical surface and this may not be the case.

The differences between the spectra of Figs. 2(a) and 2(b) can be explained on the assumption that the splitting of red and blue wings is proportional to the electron temperature. The threshold for two-plasmon decay[2] is $(v_0/v_e)^2 k_0 L > 44$, where v_0 is the electron oscillatory velocity in the pump field, v_e is the electron thermal velocity, k_0 is the wave number of the pump, and L is the density scale length at quarter-critical density. For laser light of wavelength 1.06 μm this gives $\varphi = (2.3\times 10^{16}\ \mathrm{W\cdot cm^{-2}\cdot keV^{-1}\cdot \mu m})T_e/L$. In the case of small laser prepulse the density scale length during the rising half of the laser pulse is very small and the threshold for the two-plasmon decay is exceeded only after the peak of the laser pulse as the density scale length increases. The decreasing separation of the red and blue peaks is then a reflection of the decreasing electron temperature during the falling part of the laser pulse. With a significant prepulse the initial density scale lengths are longer and threshold is exceeded earlier. The spectral separation then follows the rise and fall of electron temperature with the laser irradiance.

It may be that the pulsed nature of the $\frac{3}{2}\omega_0$ emission is due to density-profile modifications caused by the ponderomotive force of the plasma

waves. Profile modification at the quarter-critical density surface has been observed by interferometry[12] and predicted in plasma simulations.[11] Bursts of $\frac{3}{2}\omega_0$ emission associated with recurrent saturation by profile steepening and by driven ion waves have been identified in plasma simulations.[4] The latter mechanism has too short a relaxation time, less than 1 ps, while the longer time scale associated with profile steepening is not given in Ref. 4 for realistic electron-ion mass ratios.

We believe that there is an alternative explanation of the bursts of $\frac{3}{2}\omega_0$ emission since identical temporal behavior has been observed in $2\omega_0$ time-resolved spectra.[13] There appears to be no reason why different parametric instabilities at different electron densities should be related except for the hydrodynamic expansion of the plasma. If the plasma flow across the steepened density profile[14] at the critical surface is unstable, then these density fluctuations will propagate outwards through the quarter-critical region. Both $2\omega_0$ emission (near critical density) and $\frac{3}{2}\omega_0$ emission will thus be affected. The time scale of such a hydrodynamic instability is expected to be about L/v_{ia} where L is the density scale length at critical density and v_{ia} is the ion sound speed. If we assume $L \sim 3$ μm and $v_{ia} \sim 3\times 10^7$ cm·s^{-1} then the time scale of the instability is ~ 10 ps which is in approximate agreement with the observations.

We gratefully acknowledge the assistance of the members of the Central Laser Facility at the Rutherford Laboratory in carrying out these observations.

[a]Present address: Department of Physics, Essex University, Wivenhoe Park, Colchester, Essex CO4 3SQ, England.

[1]D. Biskamp and H. Welter, Phys. Rev. Lett. 34, 312 (1975).

[2]C. S. Liu and M. B. Rosenbluth, Phys. Fluids 19, 967 (1976).

[3]H. C. Pant, K. Eidmann, P. Sachsenmaier, and R. Sigel, Opt. Commun. 16, 396 (1976).

[4]A. B. Langdon, B. F. Lasinski, and W. L. Kruer, Phys. Rev. Lett. 43, 2, 133 (1979).

[5]J. L. Bobin, M. Decroisette, B. Meyer, and Y. Vitel, Phys. Rev. Lett. 30, 594 (1973).

[6]T. A. Leonard and R. A. Cover, J. Appl. Phys. 50, 3241 (1979).

[7]S. Jackel, B. Perry, and M. Lubin, Phys. Rev. Lett. 37, 95 (1976).

[8]V. Yu. Bychenkov, Yu. A. Zukhorenhov, O. N. Krokhin, A. A. Rapsov, V. P. Silin, G. V. Sklizkov, A. N. Starodub, V. T. Tikhonchuk, A. S. Shikanov, Pis'ma Zh. Eksp. Teor. Fiz. 26, 500 (1977) [JETP Lett. 26, 364 (1977)].

[9]A. I. Avrov, V. Yu. Bychenkov, O. N. Krokhin, V. V. Purtavalov, S. S. Rupasov, V. P. Silin, G. V. Sklizkov, V. T. Tikhonchuk, and A. S. Shikanov, Zh. Eksp. Teor. Fiz. 72, 970 (1977) [Sov. Phys. JETP 45, 507 (1977)].

[10]H. C. Barr, Rutherford Laboratory Report No. RL-79-036, 1979 (unpublished), Section 8.3.8 08.12.

[11]A. B. Langdon and B. F. Lasinski, Lawrence Livermore Laboratory Report No. UCRL 50021-75, 1976 (unpublished), p. 309.

[12]H. A. Baldis, J. C. Sampson, and P. B. Corkum, Phys. Rev. Lett. 41, 1718 (1978).

[13]A. J. Cole, R. G. Evans, D. Gray, J. D. Murdoch, S. M. L. Sim, and W. T. Toner, Rutherford Laboratory Report No. RL-79-036, 1979 (to be published), Section 3.4 03.16.

[14]C. E. Max and C. F. McKee, Phys. Rev. Lett. 39, 1336 (1977).